2007

Experimental investigation of an electronically collimated radiation detector for location of gamma-ray sources

William H. Hill Jr.
Louisiana State University and Agricultural and Mechanical College

EXPERIMENTAL INVESTIGATION OF AN ELECTRONICALLY COLLIMATED RADIATION DETECTOR FOR LOCATION OF GAMMA-RAY SOURCES

A Thesis

Submitted to the Graduate Faculty of the
Louisiana State University and
Agricultural and Mechanical College
in partial fulfillment of the
requirements for the degree of
Master of Science

in

The Department of Physics and Astronomy

by

William H. Hill Jr.
B.S., Louisiana State University, 1995
B.A. Tulane University, 1989

December 2007

ACKNOWLEDGMENTS

I've been working on this degree for a long time and have an equally long list of people to thank. In the last ten years, I've had three major professors and seven employers. All of them had great enthusiasm for science and patience for myself and LSU's infamous bureaucracy. Each contributed invaluable skills to this work but they are only the start of the list of helpful people.

I owe the three major professors the most. Dr. Kurt Schulz got me started. Dr. Mark Williams did double duty as a major professor and employer. The transport education he gave me was invaluable to this work. I thank Dr. Kenneth Matthews for advising me through the graduate program in medical physics at LSU and for providing me with financial support. With his guidance I have become proficient in the burgeoning field of CZT detector technology, and for the education in medical imaging physics that he has provided me I am forever thankful.

My employers have been LSU professors and fellow students. Dr. Edward Lambremont first took my graduate work seriously and I'm grateful for his encouragement. Drs. Max Scott and John Courtney both gave me invaluable training in the classroom and on the job. Dr. Scott continues to offer useful advice and has helped with this thesis directly. Without Dr. Mehmet Tumay's patient encouragement at the Lousiana Transportation Research Center, I would not know C. Fellow student, Amir Shahkarami provided me invaluable industry experience at the River Bend Nuclear Generating Station. I must also thank Dr. Ken Hogstrom for both personal guidance and working to make the Medical Physics program excellent.

There were others at each of these places of employment who deserve mention. Yvvone Thomas, Dan VanGent, Vincent Mitts, Amar Rhagavendra, Fernando Villas, Hani Titi and Murad Abu-Farsakh, Steve Byrd, Tony Huit, Ken Schacter, Hortensia Valdez, were all wonderful people to work with.

Finally, we come to the people who have made ECRD and this thesis happen. My

committee members have all given me outstanding guidance. Drs. Wei-Hsung Wang and Erno Sajo have given me good Health Physics advice. Dr. Sajo also has been a great store of transport, and simulation knowledge as well as an excellent personal adviser.
Dr. Michael Cherry is a Compton imaging heavy hitter and was always a joy to consult with. Dr. Matthews, of course, put more into the work than anyone else. Fellow researchers Dr. Blair Smith, Adam Lackie and Laurie Kelly all contributed to this work. The without the help of the LSU Physics Prototype Development Shop the device would not have worked. Brad Ellison, Randy Gould, Marcus Nauman and Douglas Smith were all patient and professional.

For all the support and assistance outside of the academic setting that made it possible for me to complete this thesis, I thank my wife, Jeannette, and my children, Elizabeth and Marie.

TABLE OF CONTENTS

ACKNOWLEDGMENTS . . . . . **ii**

LIST OF TABLES . . . . . **vi**

LIST OF FIGURES . . . . . **vii**

ABSTRACT . . . . . **xiii**

CHAPTER

1 INTRODUCTION **1**
1.1 Overview 1

2 HYPOTHESIS AND AIMS **3**
2.1 List of Aims 4
2.2 Health Physics Motivations 4
2.3 Medical Imaging Motivations 4

3 BACKGROUND AND SIGNIFICANCE **5**
3.1 Current Practice 6
3.1.1 Health Physics 6
3.1.2 Medical Physics 8
3.2 Previous and Current Compton Imaging Devices 8
3.3 Compton Angle Calculations 9
3.4 Compton Backprojection 11
3.5 Characteristics of Pixellated CZT Detectors 11
3.5.1 Hecht Charge Trapping 14
3.5.2 Charge Sharing 16
3.5.3 Previous Semiconductor Simulations 16
3.6 Sources of Uncertainty and Other Limitations 17

4 EXPERIMENTAL METHODS AND MATERIALS **19**
4.1 Prototype Detector 19
4.1.1 Prototype Calibration 23
4.1.2 Saturation and Sensitivity 24
4.1.3 Source Positioning 25
4.1.4 Data Recorded 26
4.2 Prototype Data Sets Taken 26
4.2.1 Single Pixel 26
4.2.2 Angle of Incidence 26
4.2.3 Imaging 27
4.3 Simulation Model 27
4.3.1 Infinite Hecht Charge Trapping 30

4.3.2 Linear Charge Sharing . . . 31
4.3.3 Transport Code Interaction . . . 31
4.3.4 Simulation Calibration . . . 32
4.4 Data Analysis . . . 32
4.4.1 Prototype Data . . . 34
4.4.2 Simulation Data . . . 36
4.4.3 Backprojection and Image Analysis . . . 36
4.4.4 Comparison Methods . . . 37
4.5 Laboratory Materials and Software . . . 37
4.5.1 Sources . . . 37
4.5.2 Transport Codes . . . 39
4.5.3 Prototype Hardware . . . 39
4.5.4 Prototype Software . . . 41

5 RESULTS OF DATA ACQUISITION AND ANALYSIS . . . 42
5.1 Detector Calibration . . . 42
5.2 Detector Saturation and Sensitivity . . . 42
5.3 Single Pixel . . . 45
5.4 Angle of Incidence . . . 45
5.5 Imaging Results . . . 46
5.5.1 Gross Angular Resolution and Error . . . 46
5.5.2 Backprojection . . . 51
5.5.3 Response Rates . . . 57
5.6 Simulation Results . . . 58
5.6.1 Calibration . . . 58
5.6.2 Backprojection of Prototype Simulation Data . . . 58
5.6.3 Backprojection of Simulated Box Configuration . . . 61
5.7 Comparison of Prototype and Simulation . . . 62
5.7.1 Energy Resolution and Response . . . 62
5.7.2 Mean and Mode Angles . . . 62
5.7.3 Backprojection . . . 65

6 CONCLUSION . . . 67
6.1 System Improvements . . . 67
6.2 System Applications . . . 68

REFERENCES . . . 69

APPENDIX
A GRAPHS . . . 73

B BACKPROJECTIONS . . . 109

VITA . . . 120

LIST OF TABLES

4.1 Table of source positions and nominal scatter angles for core data set. Nominal scatter angle is given as the scatter angle from the center of the front detector to the center of the side detector and a range defined by center to rear and center to front. All values ±2° 28

4.2 Table of core data set positions with scatter angles that correspond to 100 keV to 200 keV front detector energy deposition. Nominal scatter angles are from Table 4.1. 29

4.3 Calibration sources and major photon yields [1]. Activity was known to 10%. 38

4.4 Imaging sources and major photon yields [1]. Activity was known to 10%. . . 38

5.1 Mode gross angular error and resolution for the positions of Table 4.2. 49

5.2 Angular error and resolution for the source positions of Table 5.1. Resolution is given in ±x and ±y degrees half width at half maximum (HWHM) around the apparent source position to highlight asymmetry. 52

5.3 Average response rates by isotope in cps/μCi at 50 cm. Assumed energies are given in parentheses. 57

5.4 Reduced chi squared difference between prototype and simulated mean and mode averages for the source positions of Table 5.1. 63

5.5 Image error and resolution for positions of Table 5.1. The resolution is the average of x and y resolution. Errors greater than 25 degrees are considered a miss. 66

LIST OF FIGURES

3.1 Illustration of search patterns (dashed paths) for locating a radioactive source, using (left) a conventional survey meter, e.g., Geiger counter, (middle) a collimated instrument, and (right) an electronically-collimated detector with inherent direction sensitivity. With high sensitivity and directional capability, an electronically-collimated detector allows more rapid localization of sources with less hit-or-miss searching. 7

3.2 Compton Kinematics 9

3.3 Pixellated backprojection diagram showing exaggerated potential errors for pixels of length l and thickness t separated by x and y. Axis errors, due to pixelization, and energy errors both shift the position of the apparent ring. . 12

3.4 Two perfect plane backprojection examples. The left image shows the relative brightness of intersections at the source location. The right image indicates the origin with a blue cross, which represents 10 cm on the backprojection plane, and the source is indicated with a red mark and a ring projected 15° around the mark. 13

3.5 Photo of a typical CZT crystal. 13

3.6 CZT linear attenuation. 14

4.1 The L shaped prototype detector. The photos show the mounted detector modules (top left), workstation (top right), external reference frame and light tight box (bottom left) and the assembly inside the light tight box. 20

4.2 Component diagram of the L-Shaped prototype system. 22

4.3 Setting a trigger delay, left, and a good result, right. The traces show one half of the differential energy signal, green, the trigger, yellow, and the delayed trigger in purple. 24

4.4 From left to right, local co-ordinate system, pointing device, source stand and cylindrical collimator with end pieces. 25

4.5 Compton scatter energy deposition in the front detector as a function of scatter angle. The prototype could resolve depositions from 50 keV to 250 keV. . 28

4.6 Typical charge collection profiles and charge sharing model. The charge collection diagram, left, shows contributions of each term in Equation 3.9 on the left axis and a poorly calibrated energy response on the right axis. The charge sharing diagram shows one quarter of a pixel, top right, and an energy response graph for the active and inactive areas, bottom right. 31

4.7 Simplified flow chart for data analysis. 33

4.8 Simplified flow chart for simulation analysis. 33

4.9 Histogram image construction for a Cs-137 data set. Vertical lines show detector response to specific scatter angles. Horizontal lines show what scatter angles are reported as any given angle the observer sees. 35

4.10 Simplified flow chart for Free Monte simulation. 39

5.1 Energy calibration plots. The left shows energy spectra used for calibration. The right shows typical pixel calibration curves. 43

5.2 Plots of calibration slopes, left, and intercepts, right, for all pixels in the front detector for the second calibration. 43

5.3 Effect of side shielding on the Co-57 spectra at 200 cm. 43

5.4 Sensitivity tests, plotting count rates as a function of source distance for the prototype, left, and two common meters, right. The conventional meters were a NaI(Tl) scintillation detector (NaI) and a Geiger-Müller counter (GM). . . 44

5.5 Co-57 saturation tests. From left to right, voltage histograms from Co-57 at 50, 100, 150 and 200 cm. Each pixel's voltage response is represented as a horizontal gray scale line in the images. The left side of each image corresponds to -5 V and the right side to 5 V. 44

5.6 Energy spectra for a single representative pixel and the entire module (left) and fitted peak locations (top right) and residual error (bottom right) for the single pixel. 45

5.7 Co-57 angle of incidence study. Measured data is shown as symbols, Free Monte (fm) simulation as lines. 46

5.8 Mode angular error and FWHM resolution, top left, by isotope and azimuth as a function of elevation. The other five plots show histograms of angular error as a function of source position at 50 cm for the indicated isotope and assumed energy. 47

5.9 Cs-137 angular error histograms. Top diagrams are complete responses. Top left graph shows histogram of scattering angles and differences between the energy calculated and pixel geometry calculated angles. Top right is a 2D histogram image as explained in the text. The bottom graphs show mean and mode averages of vertical (left) and horizontal (right) profiles through the histogram image. The error bars around the mean averages represent one standard deviation. 50

5.10 Backprojection for the example set of Figure 5.9 with an origin cross, source mark and 15° target outline. The cross corresponds to 10 cm on the projection plane. The right figure also has half maximum points marked. 53

5.11 A view from -z direction, left, and an orthogonal view right of the data in Figure 5.10. 54

5.12 Backprojection images of a Cs-137 source in the detector's plane of symmetry. Source was placed at 50 cm, local azimuth 0° and left to right, local elevation 0°, 15° and 30°. The cross marks the origin and the circle marks 15° from source location. 55

5.13 Perfect backprojection using source to pixel calculated angles instead of Compton energy angles for Cs-137 at 50 cm, $30z, 45\phi$. The cross marks 10 cm at the origin and the target marks 15° around the source location. 55

5.14 Bottom and orthogonal views of Cs-137 at 50 cm, $45\phi, 30z$. Compare to the same information in Figure 5.15. 56

5.15 Backprojection images for Cs-137 out of the plane of device symmetry. The source was placed at 50 cm, local azimuth 45° and, left to right, local elevation 0°, 15°, 30° and 45°. The cross marks a 10 cm distance on the plane at the origin, the target marks 15° around the source location. 57

5.16 Free Monte (FM) simulated energy histograms compared to measured energy histograms. 59

5.17 Cs-137 simulated at local azimuth 0° and, left to right, local elevation 0°, 15° and 30°. The cross marks 10 cm at the origin, and the target marks 15° around the source. 59

5.18 Cs-137 simulated at local azimuth 45° and, left to right, local elevation 0°, 15° and 30°. The cross marks 10 cm at the origin and the target marks 15° around the source. 60

5.19 Backprojections and histograms of prototype, left and upper right, and simulation, middle and lower right, results for Na-22 (1274 keV) at 50 cm, $0\phi, 30z$. 60

5.20 Cs-137 simulated for the box geometry at local azimuth 0° and, left to right, local elevation 0°, 15° and 30°. 61

5.21 Cs-137 simulated for the box geometry at local azimuth 45° and, left to right, local elevation 0°, 15°, 30° and 45°. 61

5.22 Observered and simulated mean, top row, and mode, bottom row, angles from Cs-137 at 50 cm normal to the detector. The left graphs are detector response, the right are detector reports as explained in Section 4.4.1. 64

A.1 Ba-133 50cm, 0ϕ, $0z$. 74

A.2 Ba-133 50cm, 0ϕ, $15z$. 75

A.3 Ba-133 50cm, 0ϕ, $30z$. 76

A.4 Ba-133 50cm, 45ϕ, $0z$. 77

A.5 Ba-133 50cm, 45ϕ, $15z$ 78

A.6 Ba-133 50cm, 45ϕ, $30z$ 79

A.7 Ba-133 50cm, 45ϕ, $45z$ 80

A.8 Co-60 50cm, 0ϕ, $0z$. 81

A.9 Co-60 50cm, 0ϕ, $15z$. 82

A.10 Co-60 50cm, 0ϕ, $30z$. 83

A.11 Co-60 50cm, 45ϕ, $0z$. 84

A.12 Co-60 50cm, 45ϕ, $15z$. 85

A.13 Co-60 50cm, 45ϕ, $30z$. 86

A.14 Co-60 50cm, 45ϕ, $45z$. 87

A.15 Cs-137 50cm, 0ϕ, $0z$. 88

A.16 Cs-137 50cm, 0ϕ, $15z$. 89

A.17 Cs-137 50cm, 0ϕ, $30z$. 90

A.18 Cs-137 50cm, 45ϕ, $0z$. 91

A.19 Cs-137 50cm, 45ϕ, $15z$. 92

A.20 Cs-137 50cm, 45ϕ, $30z$. 93

A.21 Cs-137 50cm, 45ϕ, 45z. 94
A.22 Na-22, 511 keV 50cm, 0ϕ, 0z. 95
A.23 Na-22, 511 keV 50cm, 0ϕ, 15z. 96
A.24 Na-22, 511 keV 50cm, 0ϕ, 30z. 97
A.25 Na-22, 511 keV 50cm, 45ϕ, 0z. 98
A.26 Na-22, 511 keV 50cm, 45ϕ, 15z. 99
A.27 Na-22, 511 keV 50cm, 45ϕ, 30z 100
A.28 Na-22, 511 keV 50cm, 45ϕ, 15z 101
A.29 Na-22, 1274 keV 50cm, 0ϕ, 0z. 102
A.30 Na-22, 1274 keV 50cm, 0ϕ, 15z. 103
A.31 Na-22, 1274 keV 50cm, 0ϕ, 30z. 104
A.32 Na-22, 1274 keV 50cm, 45ϕ, 0z. 105
A.33 Na-22, 1274 keV 50cm, 45ϕ, 15z. 106
A.34 Na-22, 1274 keV 50cm, 45ϕ, 30z. 107
A.35 Na-22, 1274 keV 50cm, 45ϕ, 45z. 108
B.1 Backprojection of Ba-133 in plane of symmetry. 110
B.2 Backprojection of Ba-133 out of plane of symmetry. 111
B.3 Backprojection of Co-60 in plane of symmetry. 112
B.4 Backprojection of Co-60 out of plane of symmetry. 113
B.5 Backprojection of Cs-137 in plane of symmetry. 114
B.6 Backprojection of Cs-137 out of plane of symmetry. 115
B.7 Backprojection of Na-22 (511 keV) in plane of symmetry. 116
B.8 Backprojection of Na-22 (511 keV) out of plane of symmetry. 117

B.9 Backprojection of Na-22 (1274 keV) in plane of symmetry. 118

B.10 Backprojection of Na-22 (1274 keV) out of plane of symmetry. 119

ABSTRACT

A electronically collimated prototype detector was built with commercially available cadmium zinc telluride (CZT) modules and assessed by experiment and simulation. Sensitivity was roughly equivalent to a common hand held 1"x1" NaI(Tl) detector. The maximum useful count rate was 300 counts per second (cps) per module. Overall angular error was less than 7°, which is generally less than source placement uncertainty, and angular resolution was between 20° and 40° for several common isotopes with photon energies between 511 keV and 1333 keV. Prototype data and backprojections were used to verify a simple three dimensional model of charge induction in pixellated CZT using an uncollided flux Monte Carlo code. The goal was to devise a hand held radiation detector that can be made with rugged and commercially available parts that can see a 0.1 mCi source with an energy range of 70 keV to 2 MeV at three meters distance with an angular resolution of less than 25° full width at half maximum (FWHM). The prototype lacked sensitivity to meet this stringent goal but proved the modules and prototype concept useful for a variety of health physics applications.

CHAPTER 1

INTRODUCTION

A direction finding, hand held radiation detection system can reduce the time, personnel exposure and cost of source location in health and medical physics applications. Conventional hand held meters require a skilled operator when used for source location. In health physics, operator exposure severely limits and complicates hot source recovery. Time and accuracy of detection are obviously important for typical medical physics applications, such as intraoperative localization of sentinel lymph nodes and metastases. A reliable direction finding detector should reduce the skill and time required to locate sources. The promise and ability of cadmium zinc telluride (CZT) in medical applications has long been recognized [2]. This thesis evaluated the performance of a prototype portable CZT detector system, verified a simple model for Monte Carlo (MC) simulations and performed basic imaging tests to conclude that portable imaging with the prototype is not fully practical but a useful direction finding device is possible.

1.1 Overview

The primary hypothesis of this work is that a portable CZT detector built from commercially available CZT detector modules is capable of resolving the direction, within 25°, to a 0.1 mCi source with an energy range of 70 keV to 2000 keV at three meters distance in 30 seconds. The reasoning behind this hypothesis and the aims that were investigated to address it are described in Chapter 2.

Chapter 3 presents relevant background information on CZT radiation detectors, including the charge transport model implemented in the MC simulations. This chapter also describes current practice for source location in health physics and medical physics applications. The principles of Compton scattering and its application to radiation detection and imaging are described. The chapter concludes with comments on the uncertainties and limitations that will likely effect the source location performance of a portable CZT detector system.

The prototype detector represented only part of a full portable detector design. Radioactive sources of various energies were used to calibrate and evaluate the detector. MC simulations of the prototype and the full portable design were performed and compared to the experimental evaluation. The methods, materials and key results are described in Chapter 4 and Chapter 5. Full sets of results are provided in the Appendices. Chapter 6 concludes the thesis with a brief discussion of directions to continue the development of a viable portable, hand-held detector system for radiation source location.

CHAPTER 2

HYPOTHESIS AND AIMS

We hypothesized that a portable CZT detector would be able to calculate the direction, within 25°, to a 0.1 mCi source with an energy range of 70 keV to 2000 keV at three meters distance in 30 seconds. Compton telescopes have been used in astrophysics for decades. A number of groups are developing Compton cameras, but no one has built a hand-held model yet. The promise of CZT detectors for portable detector systems has also been recognized. Preliminary measurements indicated that a portable unit could be built with an angular resolution of 25° full width at half maximum (FWHM) for photon energies between 356 keV and 1250 keV. Better detector geometry, angle and energy discrimination should improve on that accuracy. The goal was to show if a hand held device based on commercial CZT detectors can have practical resolving time for health and medical physics use.

This thesis reports a performance evaluation of a commercially available CZT module for use in a hand held, directional detector. Energy resolution and detector response from 53 keV to 1333 keV were evaluated. Detector response was also compared with common portable meters. Cone angles from pairs of modules were computed and evaluated for accuracy. The effects of energy and angle rejection were studied. The results were further checked for agreement with Monte Carlo simulation results within experimental error.

The evaluation was used to judge the practicality of a portable detector based on these modules. Quantifying detector response relative to common detectors will provide a reference frame for typical health physics use. Estimates of the number of modules required were made based on photon detection efficiency. Detector sensitivity and angular resolution will determine the detector's ability to locate sources in a time frame that is practical for a particular application. Imaging studies indicate that 40 coincident counts are required to identify the direction to a source [3]. A practical detector needs to obtain these counts in a few seconds. Monte Carlo model validation will facilitate future design work by rapid

evaluation of specific detector geometries. Angular resolution as a function of scatter cone angle is of particular interest for minimizing the number of modules required.

2.1 List of Aims

This thesis was executed in four aims. Chapter 4 describes the materials and methods for completing the aims. Results are presented in Chapter 5.

1. Develop a prototype detector from available modules which records the location and energy deposited by individual and coincident gamma rays.

2. Measure performance characteristics. These include sensitivity, efficiency, energy and angular resolution.

3. Compare measurements to Monte Carlo predictions.

4. Make performance predictions for a complete prototype and assess the practicality of the ECRD concept.

2.2 Health Physics Motivations

Surveys for contamination and misplaced sources are common but require a well trained operator. Current equipment may have good sensitivity or directionality but rarely both. A portable meter that provides both sensitivity and directionality will save time and help reduce employee exposure.

2.3 Medical Imaging Motivations

There is great interest and demand for intraoperative imaging and location of sentinel lymph nodes. Knowledge of cancer intrusion into lymph nodes is required for diagnosis, treatment and planning. Devices for this purpose must be small, rugged, fast and accurate all at once. These are challenging and contradictory requirements. Advances in materials and electronics are on the brink of meeting this challenge with imaging systems.

CHAPTER 3

BACKGROUND AND SIGNIFICANCE

This work is part of the feasibility study and design of a portable, electronically collimated, CZT based, radiation detector. Energies of interest included 1.06 MeV and 2.0 MeV gammas, likely to escape lead shielded special nuclear materials, and lower energies of more common sources. No one has built a hand held Compton detector yet and there are significant energy and angular resolution issues to overcome. Current hand held meters trade off sensitivity and directionality with varing degrees of mechanical collimation. An electronically collimated detector could provide both sensitivity and direction that would be useful in both health physics and medical physics roles. The prototype we built and studied used Compton's relation for scattered photon energy deposited in an array of CZT detectors. Concurrent projects by others in the our research group included Monte Carlo simulation and imaging algorithms. My work provided data to validate the simulation models and to judge the practicality of the detector for medical physics and health physics uses, such as interoperative sentinel lymph node detection and locating lost radiation sources.

Compton calculations are straight forward but angle and energy discrimination schemes may further improve detection time. A sub-goal of my research was to determine the optimal scattering angle for resolving a source. The optimum scatter angles will provide the greatest number of counts with the least computational ambiguity in a practical time frame. To determine the best angles, angular error and resolution for sources in a forward facing octant of a sphere were measured. The efficiency and accuracy of detection were measured and compared to Monte Carlo simulation models. The results will guide the geometry of a practical device.

A practical, direction finding detector for hot source location can speed source recovery operations and reduce operator exposure. For sentinel lymph node location, current intraoperative probes provide either high sensitivity but no directional information

when uncollimated, or directional information but poor detection efficiency when collimated. Improving direction finding and sensitivity together would be a significant advance in current practice.

CZT is an excellent candidate material for portable detectors. CZT is rugged, dense and has good intrinsic efficiency at room temperature for energies of interest. Its principal drawback is energy spectrum tailing created by electron trapping. In a thick material, signal strength is a function of the depth of gamma ray interaction. Poor energy resolution leads to poor cone angle resolution and imaging but this may not matter too much in a hand held unit where any timely direction finding is helpful. Rise time compensation in support electronics is significantly improving CZT energy resolution [4]. This thesis shows that a practical detector system is feasible even with the less than ideal commercial modules used for this evaluation.

3.1 Current Practice

Current hand held detectors sacrifice sensitivity for directionality with collimation. Collimated detectors have a narrow field of view and must be pointed directly at the source to sense anything. The volume of detector material typically must be small or the collimator will be too heavy. In the world of mechanical collimation, five centimeter thick lead block is considered portable. Such detectors can have angular resolution of 25° FWHM at 662 keV [5], which is comparable to the angular resolution of our device.

3.1.1 Health Physics

Conventional collimation has proved impractical for most applications and source recovery remains difficult and requires skilled operators. Figure 3.1 shows conventional and proposed search methods. In a typical health physics scenario, uncollimated detectors are carried by trained personnel in a systematic walk to find sources and contamination. The operator walks toward increasing count rates. This is difficult for low activity and multiple sources, which are often hidden by background radiation, and exposes the operator when the source is strong. Training can improve survey performance [6], but mastery is required with current equipment. Trained NATO operators were not always able to find sources due

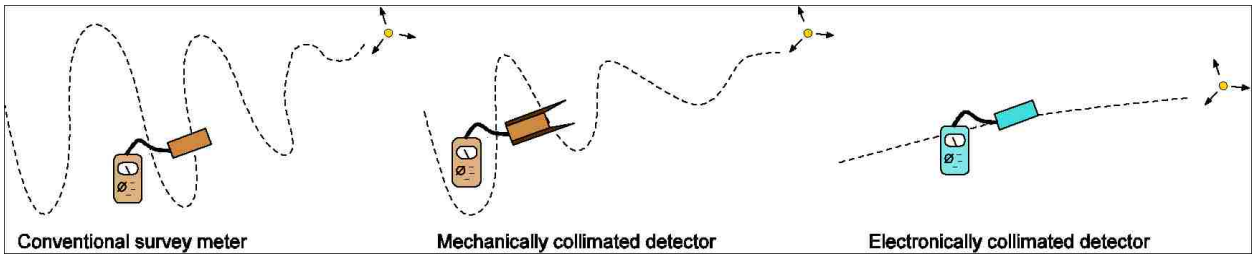

Figure 3.1. Illustration of search patterns (dashed paths) for locating a radioactive source, using (left) a conventional survey meter, e.g., Geiger counter, (middle) a collimated instrument, and (right) an electronically-collimated detector with inherent direction sensitivity. With high sensitivity and directional capability, an electronically-collimated detector allows more rapid localization of sources with less hit-or-miss searching.

to inexperience and equipment limits in large scale training exercises [7]. All current portable detection equipment has frustrating limitations [8]. One interesting, unconventional collimation technique is to place detectors on either side of the operator's head and provide stereo audio feedback [9]. Coded apertures are one means to provide fast imaging of sources [10]. While lighter than full collimators, they typically have a narrow field of view and are less efficient than desirable for high energy sources.

Operator exposure places great constraints on hot source recovery. Exposure must be planned and distributed over several operators to prevent excessive exposure to any single operator. Because the source location is not known, plans must be conservative. Planning time and time spent rotating operators both add to recovery operations. If the hot source recovery is critical path, the entire site remains down for the duration. Quick location of sources won't eliminate the need for planning, but it can simplify and speed the process.

Non mechanical direction finding can reduce operator exposure and save time in source recovery operations. An electronically collimated detector is as sensitive as any conventional solid detector of the same size but will also provide directional indication. In many circumstances, the operator can be replaced with a robot and this will eliminate operator exposure required to find the source. In other circumstances, timely directional information will reduce operating time and hence operator exposure. In all circumstances, planning is simplified and improved by better knowledge of the source location.

3.1.2 Medical Physics

Compton imaging for medical purposes was proposed as early as 1974 [11]. Singh and others pioneered the design of Compton cameras for radioisotope imaging and showed that order of magnitude increases in efficiency were possible with electronic collimation [12]. Use of a three scatter model for Compton imaging shows great resolution and sensitivity improvements [13]. Others have proposed large cylindrical detectors for SPECT [14]. Increasing sensitivity in imaging always reduces dose to patients and medical staff.

For work with small organs like the thyroid and sentinel lymph nodes there are two established techniques. Anger cameras with 3 mm resolution [15] and small probes [16, Chapter 1], [17] have been fielded. Tiny probes for sentinel lymph nodes have the same kind of trade offs as larger detectors for searches. Collimation provides directionality at the cost of reduced sensitivity. Both of these approaches require highly efficient and compact materials. The smaller the probe, the less invasive and more useful it can be. Imaging is the more difficult application and places more stringent requirements on energy and spatial resolution.

Hospitals have health physics needs too. They routinely handle and must account for hundreds of tiny sources. Prostate seed implants, for example, are very common. Each operation uses approximately one hundred tiny seeds. Careful checks of the operating room must be made to be sure none was left behind in bedding or fluids. Currently, that means an exhaustive sweep of the theater with a hand held meter. This is tedious and error prone.

3.2 Previous and Current Compton Imaging Devices

While Compton telescopes have been around for decades, no one has produced a hand held model. Astronomers have been using Compton telescopes for higher energy x-rays since 1984. They have moved on to sophisticated techniques which include dual Compton scatter and recoil electron tracking [18, Chapter 19]. The COMPTEL (Compton Telescope), MEGA (Medium Energy Gamma-ray Telescope) and ATHENA (Advanced Telescope for High-Energy Nuclear Astrophysics) projects are examples [19], [20], [21]. These devices, however, weigh thousands of pounds.

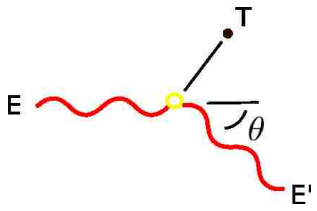

Figure 3.2. Compton kinematics.

Portable and compact devices have been made, but they are still very large and heavy. The Michigan group's C-SPRINT [22] obtained results comparable to Anger cameras with a silicon front scattering detector and 1 m diameter ring of scintillating secondary detectors. They are also working on another 3D imaging device, C-SPECT [23]. Vetter and others at the Lawrence Livermore National Laboratory have made the SPEctroscopic Imager for g-Rays (SPEIR), a Si and Ge detector that achieved a 3° angular resolution at 344 keV, which is close to the theoretical limit [24]. Wulf, Kurfess and others at the Naval Research Lab have applied a three scatter Compton formula to strip detectors with reasonable results [25]. All of these devices are too large to be hand carried and many require cryogenic cooling. The Michigan group's 3D positioning CZT detector is small and can be made portable or handheld with excellent positional and energy resolution [4], [26].

3.3 Compton Angle Calculations

Dr. Arthur Holly Compton derived the relationship between photon scatter energy and angle, θ, by balancing momentum and energy for photon-electron interactions seen in Figure 3.2. If we ignore the binding energy of an electron at rest, the scattered photon energy, E', and recoil electron energy, T, are given by

$$E' = \frac{E}{1 + (E/mc^2)\,(1 - cos\theta)} \tag{3.1}$$

and

$$T = E - E' = \frac{(E^2/mc^2)\,(1 - cos\theta)}{1 + (E/mc^2)\,(1 - cos\theta)}. \tag{3.2}$$

where E is the intial photon energy and m is the electron rest mass.

These relations can be used directly by solving for scatter angle in terms of energies. The accuracy of angle calculations as a function of energy given the assumptions is well documented and understood. Uncertainty created by finite pixel size, energy resolution and Doppler broadening have been described by Ordonez and others who predict the best cone angle resolution of 5° for scatter angles between 20° and 110°, given 1% FWHM energy resolution [27], [28], [29], [30].

We looked at two methods of direct use. The first method uses the measured energy depositions for the two interactions so that

$$\theta = cos^{-1}\left(1 - mc^2\left(\frac{1}{E_2} - \frac{1}{E_1 + E_2}\right)\right) \tag{3.3}$$

where E_1 is the energy deposited in the first detector and E_2 is the energy deposited in the second detector. This may not be well suited to portable detectors because it assumes the scattered photon is photo-electrically absorbed in the second detector. A high intrinsic efficiency secondary detector is required for this to work well and it will always suffer from energy measurement inaccuracies of both detectors. A better estimate of E_2 can be obtained by using an external calorimeter.

The second method uses an assumed source energy.

$$\theta = cos^{-1}\left(1 - mc^2\left(\frac{1}{E_\gamma - E_1} - \frac{1}{E_\gamma}\right)\right) \tag{3.4}$$

If the isotope is known, the scatter angle calculation can be performed using the first energy deposition. The second interaction is then used for cone axis direction finding alone as discussed in Section 3.4. A drawback to this method is that multiple photon energies and previously scattered photons will have incorrectly calculated cone angles. Improvements on this method would be to use the second energy deposition and a calorimeter to estimate which photon energy of the expected energies any given photon was. When the energy difference between primary photons is large, the second detector does not require good energy resolution or perfect stopping power. An external calorimeter could also be used for spectroscopy and isotope identification when the isotopes present are not known.

Two further improvements, the three Compton scatter method and recoil electron tracking, are not possible with our geometry. Kurfess and others at the Naval Research Lab have proposed a three Compton method, which uses the angles from two sequential scatters. This eliminates the need for total absorption and is good for higher energy photons [31], [32]. It also enables the use of thinner CZT detectors, which inherently have better energy resolution, for secondary scatter detectors. An alternate detector geometry is required to make this work well. Recoil electron tracking can be used, when backprojecting, to further limit the backprojected arc [33]. CZT detectors are not yet capable of electron tracking [34].

3.4 Compton Backprojection

Figure 3.3 shows the basics of Compton image reconstruction and potential errors from a pixellated detector. It is helpful to think of shining a flashlight against a wall. A cone axis is drawn to the projection surface through the estimated interaction points. The cone, with an opening angle equal to the Compton scatter angle, is drawn with its vertex at the first interaction point. The intersection of this cone with the projection surface forms the image as shown in Figure 3.4. If there are no errors, every projection will pass though the source point. Recoil electron tracking can reduce the amount of cone that must be projected while still containing the source point. Research by Lackie et al. indicates that useful direction information can be obtained from as few as 50 cones, depending on the specific backprojection algorithm used [35] [3]. Others have used filtered backprojection of spherically projected cones for CZT and shown that it is less computationally intensive than maximum likelihood and other methods [26].

3.5 Characteristics of Pixellated CZT Detectors

CZT is an excellent candidate material for portable detectors. It is rugged, dense and sensitive at room temperature for energies of interest. The principle drawback is energy spectrum tailing created by charge trapping. In a thick detector, signal strength is a function of the depth of gamma ray interaction. The University of Michigan has pioneered

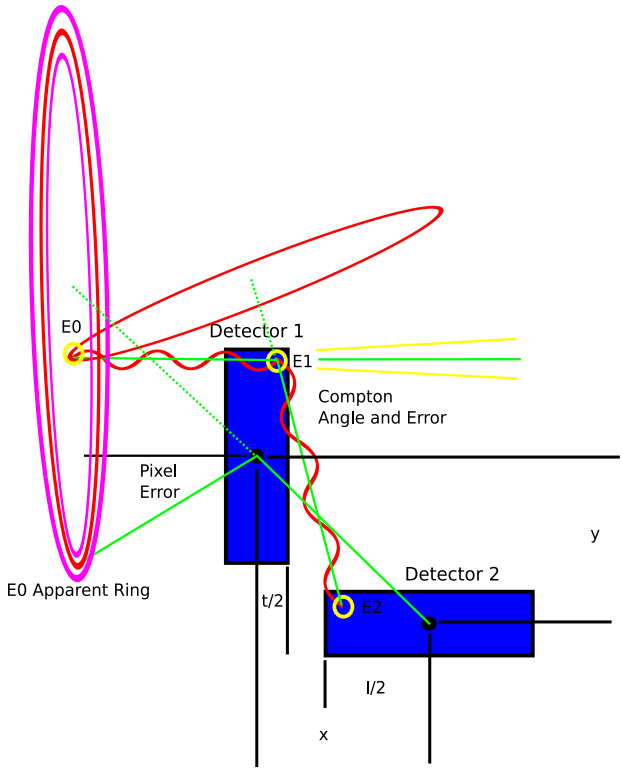

Figure 3.3. Pixellated backprojection diagram showing exaggerated potential errors for pixels of length l and thickness t separated by x and y. Axis errors, due to pixelization, and energy errors both shift the position of the apparent ring.

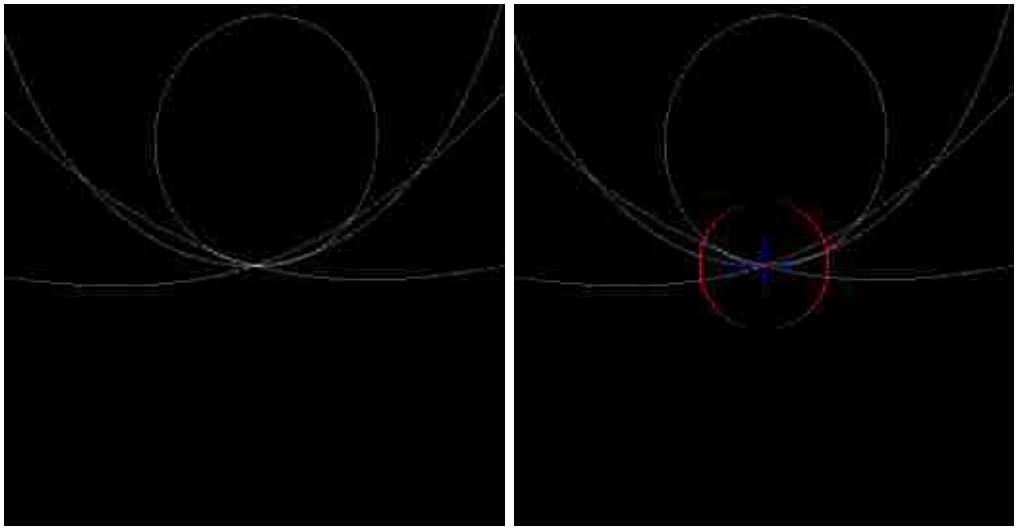

Figure 3.4. Two perfect plane backprojection examples. The left image shows the relative brightness of intersections at the source location. The right image indicates the origin with a blue cross, which represents 10 cm on the backprojection plane, and the source is indicated with a red mark and a ring projected 15° around the mark.

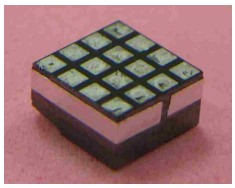

Figure 3.5. Photo of a typical CZT crystal.

improved spatial and energy resolution with single polarity charge sensing [36] and rise time compensation [37] and have achieved excellent spatial and energy resolution [38]. Use of these techniques in future portable CZT Compton detectors would likely be advantageous.

Figure 3.5 is a typical $Cd_{1-x}Zn_xTe$ (CZT) crystal. It is a dense, shiny and metallic material. The commercial crystal shown here is about a centimeter square and is 5 mm thick. The top surface has sixteen vapor deposited contact pads and the bottom surface is covered in a single large contact pad. The side has a grounding plane wrapped around it.

CZT's high density gives a detector excellent stopping power. Figure 3.6 shows the linear attenuation coefficient of CZT and its major components for the energy range of interest. Only silicon detectors have better stopping power for part of this range.

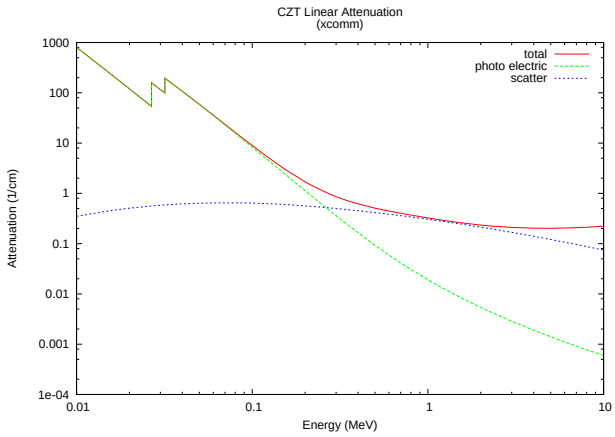

Figure 3.6. CZT linear attenuation.

While CZT detectors can be larger than CdTe detectors, several factors limit size [16]. The vertical Bridgman growth process requires pressures on the order of 100 atm, and this limits boule size. The pressure is required to limit cadmium evaporation. Boules are not typically single crystals so crystals are cut out by hand. There are material variations between and within single crystals that degrade energy resolution and parts of boules are not usable [16].

3.5.1 Hecht Charge Trapping

Hecht's relation describes charges induced on surface electrodes as a function of depth in a planar detector. The charge, Q^*, induced in the detector's electrode is a function of the distance traveled, described by the Shockley-Ramo theorem [39, equation 13.4]

$$dQ^* = -\frac{eN_0}{t}\left(dx_e + dx_h\right) \tag{3.5}$$

where N_0 is the number of initial charges, e is the electric charge, t is the thickness of the detector, and dx_e and dx_h are the distances traveled by the electrons and holes. The actual paths the charges take depend on the shape of the applied field and the actual charge induced is the integral of charge motion on those paths [39, Appendix D].

When charges are lost due to trapping the induced signal is reduced and response amplitude becomes a function of interaction depth. Charge loss is mostly a function of

applied potential and material properties. In an infinite planar detector, the relation between charge mobility and charge collection efficiency can be expressed by the Hecht relation [39, Equation 13.5]

$$Q^* = eN_0 \left(\frac{\nu_h \tau_h}{t} \left[1 - exp\left(-\frac{x_i}{\nu_h \tau_h} \right) \right] - \frac{\nu_e \tau_e}{t} \left[1 - exp\left(-\frac{x_i - t}{\nu_e \tau_e} \right) \right] \right) \tag{3.6}$$

where τ is the charge carrier lifetime. x_i is the depth of interaction measured from the cathode. The electron and hole velocities and lifetimes are given by ν_e,τ_e and ν_h,τ_h respectively. The velocity, ν, is a function of electric field, ε, and mobility, μ, and is relatively constant for most detectors. Electric field is constant for a flat detector with a fixed voltage. For strong electric fields, charges are accelerated quickly to their saturation speed,

$$\nu = \mu\varepsilon. \tag{3.7}$$

Electrons have greater mobility than holes in CZT, typically by an order of magnitude. Typical values are 1350 cm^2/V-s for electrons and 120 cm^2/V-s for holes. Values of average electron life time have been reported between 100 ns and several μs. Hole life times vary between 50 ns and 300 ns [16], [39].

The product of charge velocity and life time represents an average trapping length, λ. The trapping length divided by the actual detector thickness is the carrier extraction factor, a good indicator of induced charge production.

Because energy reported is proportional to the charge induced,

$$E = kQ^*, \tag{3.8}$$

the Hecht relation can be simplified to

$$E = E_0 \left(\frac{\lambda_h}{t} \left[1 - \exp\left(-\frac{x}{\lambda_h} \right) \right] - \frac{\lambda_e}{t} \left[1 - \exp\left(\frac{x - t}{\lambda_e} \right) \right] \right). \tag{3.9}$$

Typical response for our detector can be found in Section 4.3.2.

A consequence of Hecht's relation is that angle of incidence can change energy response and resolution. Photons with shallow angles of incidence have shallow energy depositions which produce better signals. This effect has been documented for CZT [40].

3.5.2 Charge Sharing

Monolithic CZT is usually pixelated by applying a grid of conductors to the crystal's anode side. The material directly under the anode is considered "active." Charges deposited under the active area may induce charges on neighboring pixel anondes, depending on pixel size and applied voltage. Ionization in the inactive area between the anodes may induce charges in more than one anode, regardless of pixel size, which results in charge sharing between pixels [39, Appendix D].

3.5.3 Previous Semiconductor Simulations

Radiation transport and electrical simulations model different phenomena and are typically separate, specialized packages that must interact. Monte Carlo methods are used in codes such as GEANT [41] and MCNP to model energy deposition in materials by Boltzmann diffusion. Statistically significant numbers of "random walks" of particles guided by statistical models of physical interaction of those particles with other matter are tracked and the energy deposited is recorded. The average behavior of particles in the physical system is then inferred, using the central limit theorem, from the average behavior of the simulated particles [42]. Energy deposited in real materials liberates charges which transport routines ignore once they have dropped below a certain energy level. More sophisticated codes may take into account Doppler broadening and these have been used for models of medical devices like C-SPRINT [43] and our prototype detector [44],[45]. Other simulations have optical transport [46]. In general, methods other than Monte Carlo are used to model the electrical conduction of the liberated charges and induction in nearby conductors, and these methods must be integrated with the MC transport code.

An electrical model is typically built for ionization response simulations and several studies have been done with CZT. The electrical model solves the Laplace equation for charge flow and induction for the particular geometry [39], [47]. Flow and induction are recorded by starting position and output for each pixel. Mathy presents a finite element method solution where rise time as a function of pulse amplitude is simulated [48]. Others have worked to simplify the method for CZT [49]. To be effective, material properties must

be estimated and the exact geometry must be known.

3.6 Sources of Uncertainty and Other Limitations

There are geometric, electronic, calibration and radiological sources of uncertainty. Geometric uncertainty comes from pixelization and relative placement of the detectors. Electronic uncertainty comes from amplifier, power supply and electromagnetic noise as well as CZT leakage current. Radiological uncertainty comes from background and scattered radiation. All of these degrade data quality potentially effecting angular resolution, image contrast and localization error. CZT has performance limitations that must also be understood for a particular detector, such as temperature limits which degrade energy resolution and reverse charge build up due to trapping which puts an upper limit on count rate.

Geometric and pixelization errors result in incorrect cone axis location and direction but are relatively easy to quantify. Pixel size and accuracy of placement are known, so the geometric component of angular errors can be computed directly.

Electronic and calibration errors are important but energy resolution is dominated by charge trapping. Electronic noise can be measured directly at the analog energy signal in the absence of gamma-ray interactions. Calibration errors can be determined by linear regression for each pixel. The uncertainty introduced by charge trapping, however, is much greater. Charge trapping uncertainty is non Gaussian and the best report is FWHM energy resolution at a particular energy. The net result of energy uncertainty is an incorrect cone angle.

Background radiation and radiological pollution can degrade image quality. Laboratory contamination, poorly shielded sources, and terrestrial, cosmic and scattered photons all contribute to detector response. This reduces contrast and contributes to blurring.

All of the sources of uncertainty produce image blurring which can also be measured directly using a point source. Ultimately, a given source at a given location will produce an image with the cumulative results of all the uncertainty built into the detector. The

maximum intensity point should match the actual source location and the location error can be quantified by the angular difference. The spread around that point is angular resolution measured as the FWHM of the intensity profile. Measures of these types are used in this thesis to quantify the Compton detector's performance.

CHAPTER 4

EXPERIMENTAL METHODS AND MATERIALS

An L shaped prototype detector and two simulation models were developed to judge the imaging ability and the performance of the ECRD detector concept. Tests were devised to quantify the sources of uncertainty discussed in Section 3.6. The prototype detector was calibrated by flood exposure to five low energy sources and then used to image four higher energy sources. Sensitivity, energy resolution and angular resolution were determined and compared to common hand held meters. A simulation model of the L shaped prototype was verified against calibration and imaging data for energy spectrum agreement, and mean and mode average angle agreement. A separate box shaped simulation model was used to estimate the performance of a more complete geometry detector. Backprojections of experimental data and simulation results were made and compared by angular error and resolution, then used to estimate full detector performance. This chapter provides a functional description of the prototype detector, data acquisition, the simulation model, comparison tests, and an explanation of how the results were projected to the full detector concept. Finally, a detailed list is provided of research materials used.

4.1 Prototype Detector

The ECRD prototype detector is shown in Figure 4.1. It was made from detector modules, support electronics, a light tight box and positioning systems. Figure 4.2 shows the signal paths and relationship between the components. The prototype provided energy and position data for 512 front and 512 side pixels.

We modified components from two existing CZT gamma cameras [50] to make the prototype system. The front and side subsystems each had two detector modules, each with 256 pixels and an electronics package. The detector modules were carefully mounted in a frame so that the relative pixel positions would be known to an accuracy of half a millimeter. The electronics were modified to provide energy and position information for coincident gamma ray interactions. The device frame, detector modules and electronics

Figure 4.1. The L shaped prototype detector. The photos show the mounted detector modules (top left), workstation (top right), external reference frame and light tight box (bottom left) and the assembly inside the light tight box.

were placed in a light tight box and only opened with red light illumination.

The CZT detector modules were 5 mm thick by 38 mm by 38 mm monolithic crystal assemblies. Each module has a 16 by 16 array of 2.4 mm pitch pixels and two ASICs for preamplification, trigger generation and multiple pixel hit detection. The ASICs provided an output signal from only one pixel per module per gamma ray interaction. Hits to multiple pixels were reported as a sum of energies at the hit locations and a multihit signal was driven high so the data could be rejected. Additional amplification and signal processing were performed by supplemental electronics boards, provided by the CZT module's manufacturer.

The performance characteristics of the gamma camera electronics and individual detector modules were previously examined [50]. Count rates were reported to be linear up to 3,300 counts per second for the system and 60,000 counts per second for the module itself. Average pixel energy resolution for 1 mm collimated, active area hits was reported at 6.5% FWHM for the 140.5 keV peak of Tc-99m. Flood energy resolution was about 35% FWHM for Ba-133 (81 keV) and 18% FWHM for Co-57 (122 keV, 136 keV). There was also an apparently linear fall off of counts as the 1 mm collimated source was stepped between active pixel centers.

Signals were routed from the subsystem electronics to two separate but synchronized data acquisition systems (DAQ), as shown in Figure 4.2. The front and side subsystem of the prototype each provided separate energy, location, trigger and multihit signals. Trigger signals were routed to a coincidence detector, pulse counter and a delay. The coincidence detector was used to identify events based on either of the subsection triggers or their coincidence. The pulse counter was used for all rate measurements. The delay was used to avoid the system's analog sample and hold signal bounce. Analog differential energy signals were routed to the analog I/O DAQ system. Binary position and multihit signals were buffered and routed to a digital I/O DAQ system. Both DAQs were synchronized by the delayed trigger. When triggered, the acquisition system recorded both sets of pixel, energy and multihit signals. The DAQ output was two files, one with pixel, module and multihit

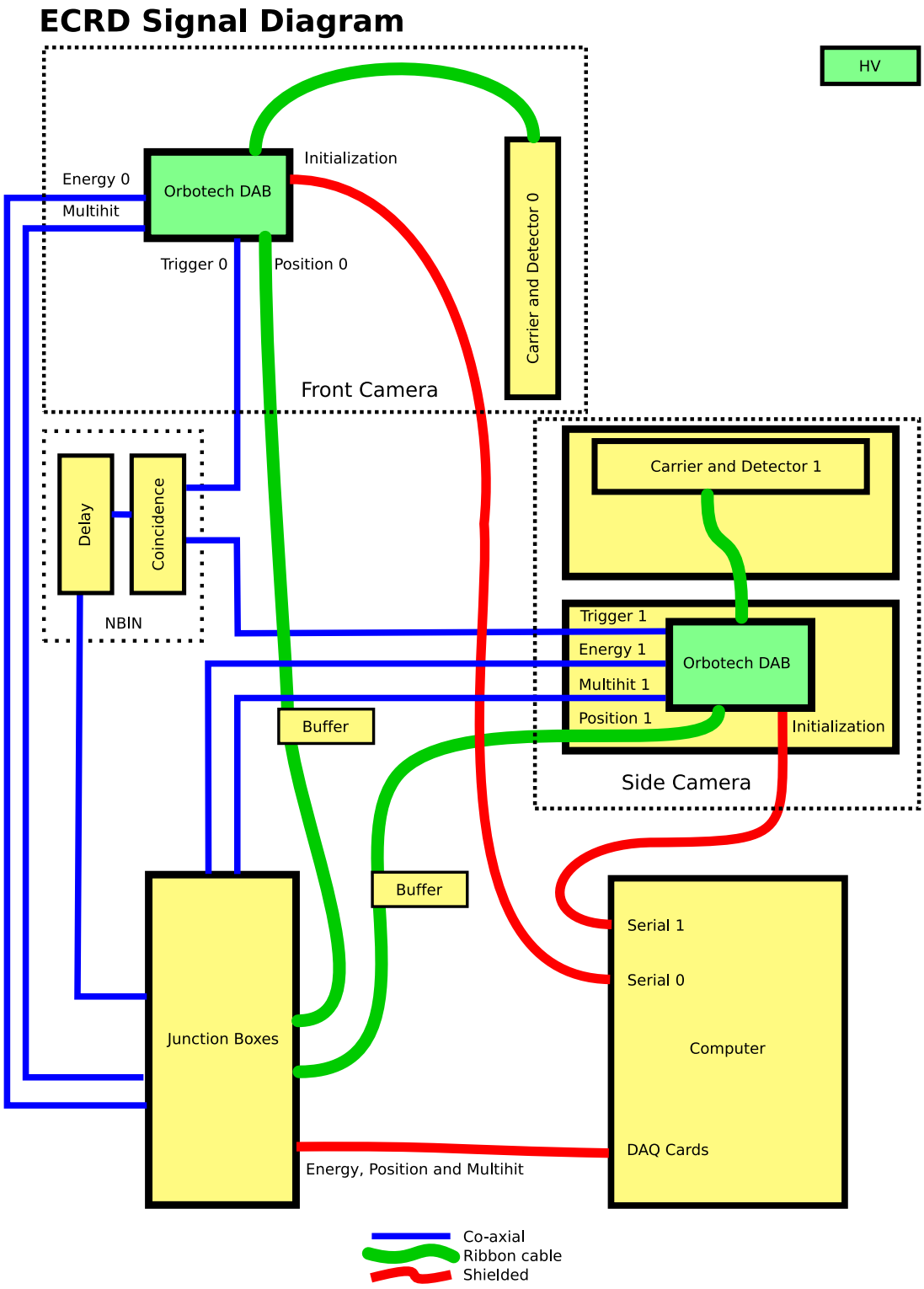

Figure 4.2. Component diagram of the L-Shaped prototype system.

data and one with differential energy data.

Each subsystem was calibrated separately on a per pixel basis with the isotopes of Table 4.3. Compton scatter data were acquired with higher energy sources listed in Table 4.4 in the positions listed by Table 4.1 using the entire system in coincidence mode. System sensitivity and saturation were also measured with the high energy sources. Sensitivity was measured in the same way with conventional detectors and compared.

Coincidence data were analyzed for sensitivity, energy deposition and scatter angle. Because the prototype geometry and source location were known, angles computed from energy were easily compared to the assumed true angles from source locations and pixel positions. Coincidence between subsystems could also be determined by the analysis software; data could be taken by coincident or subsystem triggers. Coincident hits were then backprojected and analyzed for angular error and angular resolution.

4.1.1 Prototype Calibration

Two energy calibrations were made for the prototype, once before Compton scatter data acquisition and once after most of the data had been taken. The first calibration used Ba-133, Cd-109 and Co-57. The second calibration used Co-57, I-123 and Tc-99m. Rate information was taken for each subsystem using a pulse counter for each source and for background so that background could be subtracted. All of the data presented here were analyzed using the second calibration.

Before the device could be calibrated, the trigger delay had to be set. As seen in Figure 4.3, the differential energy signals had considerable bounce. An additional RC circuit smoothed this out, but it was still advantageous to delay digitization until the latter part of the signal. The trigger delay was determined by collecting Co-57 spectra and selecting the trigger delay that provided the best histogram. The trigger delay was fixed before the first calibration and not changed again.

For calibration, data were taken from each subsystem during normal flood illumination by each of the low energy sources. To minimize background and noise, the sources were as close as possible without saturating the detector. Collimated and

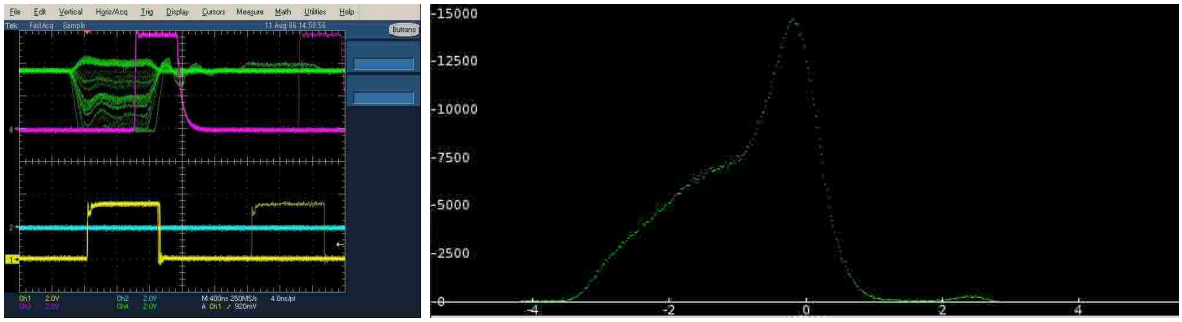

Figure 4.3. Setting a trigger delay, left, and a good result, right. The traces show one half of the differential energy signal, green, the trigger, yellow, and the delayed trigger in purple.

uncollimated source spectra were acquired for each pixel. Slope and intercept were determined with at least three sources by a least squares regression. σ_{yx} was used as a mechanical cut off to eliminate pixels with obvious errors and the rest were checked by hand. The maximum voltage each pixel could generate was also recorded, so that saturated event signals could be rejected during analysis.

Sample backgrounds were also recorded and removed from the Ba-133, Cd-109 and Co-57 source spectra of the first calibration data. Subtraction was done by count rate and total counts, so that the correct amount of background would be removed from any given spectrum. This made little difference in peak location, slope and intercept so background subtraction was not used for the second calibration with Co-57, I-123 and Tc-99m.

4.1.2 Saturation and Sensitivity

A usable count rate was determined from detector saturation. The highest activity source, Co-57, was measured at decreasing distances until the detector was no longer able to respond linearly. Voltage histograms were monitored for each pixel and visually inspected for changes in shape. While any pixel was saturated the detector was considered saturated. A count rate that produced no visible change in voltage histograms was considered safe.

Sensitivity was measured and compared to common Geiger-Müller ionization and 1”x1” NaI scintillation survey meters. The detectors were placed in similar geometry to the prototype and count rates were measured for all the sources except I-123 and Tc-99m at several distances to produce inverse square response graphs. The response rate at 100 cm

Figure 4.4. From left to right, local co-ordinate system, pointing device, source stand and cylindrical collimator with end pieces.

per decay corrected μCi was compared to the same for the prototype detector.

4.1.3 Source Positioning

Sources were placed both inside and outside of the light tight enclosure with two devices that provided $\pm 2.5°$ of angular accuracy. Inside the enclosure, pointing rigs were used. A fixed reference frame was constructed and leveled for sources outside of the light tight enclosure. The pointing rig used for the core data sets is shown in Figure 4.4. This had a fixed radius of 50 cm. The external reference frame is shown suspended above the light tight box in the bottom left image of Figure 4.1.

Two local co-ordinate systems were defined. One used the radius, elevation and azimuth to identify the source location relative to the detector system, as illustrated in Figure 4.4. The radius was defined as the distance to the source from the center of the front detector. The elevation, z, was the angle between the X3-X1 plane and the line to the source. The azimuth, ϕ, was defined as the rotation angle from the X3-X2 plane to the projection onto the X3-X1 plane of the line to the source, with the positive direction counterclockwise from the X3 axis. Co-ordinates were also translated to local Cartesian co-ordinates, with the axes oriented as shown in Figure 4.4. For source positions external to the light tight box, the X1,X2 and X3 coordinates were measured directly to within ± 1 mm and then translated to local angular co-ordinates.

4.1.4 Data Recorded

For each interaction, the prototype subsystems each reported a trigger, energy, module number, pixel address and multiple-hit flag. The trigger was a five volt TTL signal. The energy was represented as differential analog voltage signals produced by the module. These were amplified to a range of -5 to 5V and digitized. The pixel address, module number and multiple-hit flag was encoded as a 16 bit integer. The data were saved in two files, one for energy and one for pixel information.

4.2 Prototype Data Sets Taken

The data sets taken were designed to test the equipment itself, the simulation model and the imaging algorithm. Calibration, sensitivity and saturation tests discussed above provided module performance information. The electronic noise level present on the analog lines was observed with an oscilloscope. Single pixel irradiation and angle of incidence studies provided additional detector performance information. The side subsystem trigger was delayed to test for accidental coincidence rates, and count rates of collimated and non collimated sources were compared to estimate scatter count rate. Finally, Compton scatter data were acquired to determine gross angular error and angular resolution directly and with the imaging algorithm.

4.2.1 Single Pixel

The active area of a single pixel was illuminated with Co-57 to determine energy resolution with minimal charge sharing. The source was collimated to 1 mm width using the collimator shown in Figure 4.4 with two of the collimating caps. Energy histograms were constructed for the pixel itself and the sum of all pixels. Angular resolution was determined for both histograms. The results of this test were also used to set the parameters of the simulation model.

4.2.2 Angle of Incidence

A consequence of Hecht's relation, Equation 3.6, is that photons impinging at steep incidence angles interact at shallower depths and have less tailing. The front detector was

illuminated with the collimated Co-57 source from 260 cm at 0°, 30°, 45° and 60° elevation to determine the effect on the energy resolution. The collimated beam was just wide enough at this distance to uniformly illuminate the front detector. Energies, positions and count rate were recorded as a function of angle of incidence. Energy resolution was determined from the sum energy histogram.

4.2.3 Imaging

Count rates, energy and interaction positions were recorded for Ba-133, Co-60, Cs-137 and Na-22 over a range of source positions covering an eighth of a sphere at 50 cm and other distances. The core data set was collected from uncollimated sources at 50 cm, at two local azimuths and four local elevations. This provided a wide variety of scatter angles and source positions. The sets from each source contained at least one position where the scatter angles fell within the detector's energy measurement limits. They also contain a good set of near and off axis conditions to test backprojection algorithms. The nominal scattering angles and source positions are listed in Table 4.1.

Table 4.2 lists positions where the best results are expected for each isotope based on the range of possible scattering angles for the source energy of interest which matches the measurable energy range of the front detector. Several other positions were close to this range and could also yield satisfactory results. Figure 4.5 shows ideal energy depositions for the range of interest within the limits of our equipment. The best scatter angles should be between 20° and 60°. The energy range of interest has a forward peaked scatter probability.

Additional data was taken at other locations to investigate the effects of collimation and distance, and to fill in angles missed by the core data set. Collimated and uncollimated energy spectra were recorded for Co-57 at 200 cm, $0z$, 0ϕ. Several Cs-137 and Na-22 sets were taken at 100 cm and other distances which are reported when appropriate.

4.3 Simulation Model

A simulation model was made for the physical processes unique to CZT that can be used with any transport code. The Hecht relation for an infinite plane detector was used to

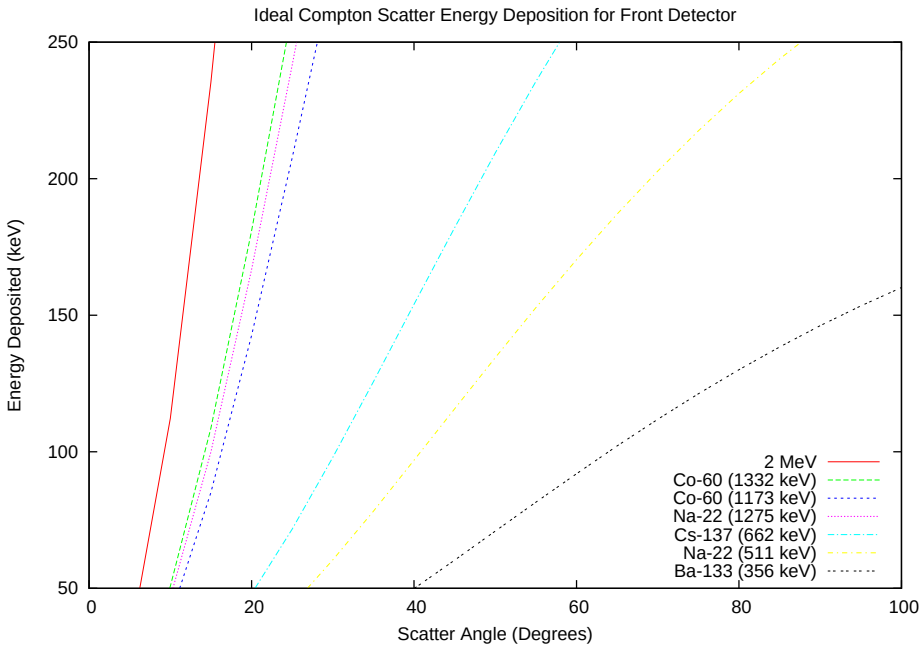

Figure 4.5. Compton scatter energy deposition in the front detector as a function of scatter angle. The prototype could resolve depositions from 50 keV to 250 keV.

Table 4.1. Table of source positions and nominal scatter angles for core data set. Nominal scatter angle is given as the scatter angle from the center of the front detector to the center of the side detector and a range defined by center to rear and center to front. All values $\pm 2°$.

Azimuth, ϕ	Elevation, z	Normal, θ_n	Nominal Scatter, θ Center to Center(Rear,Front)
0	0	0	43 (30,67)
	15	15	28 (15,52)
	30	30	13 (0,37)
45	0	45	59 (52,74)
	15	47	47 (44,60)
	30	52	38 (39,46)
	45	60	32 (38,32)

Table 4.2. Table of core data set positions with scatter angles that correspond most to 100 keV to 200 keV front detector energy deposition. Nominal scatter angles are from Table 4.1.

Isotope	Photon Energy (keV)	Scatter Range (degrees)	Position (ϕ,z degrees)	Nominal Scatter (θ, degrees)
Ba-133	356	60-120	45, 0	59 (52,74)
Co-60	1225	15-25	0, 30	13 (0,33)
Cs-137	662	30-50	0, 0	43 (30,67)
			0, 15	28 (15,52)
			45, 30	38 (39,46)
			45, 45	32 (38,32)
Na-22	511	40-70	0, 0	43 (30,67)
			0, 15	28 (15,52)
			45, 0	59 (52,74)
			45, 15	47 (44,60)
			45, 30	38 (39,46)
Na-22	1274	15-25	0, 30	13 (0,37)

account for charge trapping at depth. A linear model was used to approximate charge sharing between pixels in the x and y direction. Random Gaussian signals of fixed maximum amplitude were added to model electronic noise. This simple model for charge trapping and sharing provided a full 3D model of CZT response and was implemented with a few lines of C code. It was used with Free Monte, a basic Monte Carlo simulation system developed in house, but can be used with GEANT4, MCNP or any other code that allows per interaction calculations.

Thick detector CZT simulations must take into account charge trapping, sharing and noise which reduce signals and broaden recorded energy distributions. Charge trapping in the material reduces the charge that will be induced on collecting electrodes. Ordinary charge induction is mostly a function of depth of interaction. The further charges travel, the larger the signal induced. Charge trapping creates an upper limit on the charge that can be induced by charges moving through a given thickness. The further charges have to move, the more likely they will be trapped. Charges produced between pixels can induce charges on more than one electrode. This kind of charge sharing is a function of depth and planar location. Noise comes from statistical effects of ionization as well as heat in the detector and electronics.

A more detailed model could be built from an electrical simulation but this was beyond the scope and ability of the current work [39], [47]. An electrical simulation would solve charge induction using the Laplace equation to obtain weighting factors for the particular geometry. Flow and induction would be recorded as a table of weighting factors by starting position and output for each pixel. To be effective, however, material properties would have to be estimated and the exact geometry would have to be known. The simple model used here allowed for quick material property estimation as described in the calibration section below.

4.3.1 Infinite Hecht Charge Trapping

Equation 3.9 was used to model charge trapping at depth. Starting values for mean path lengths were taken from the literature. A typical expected depth response is shown in

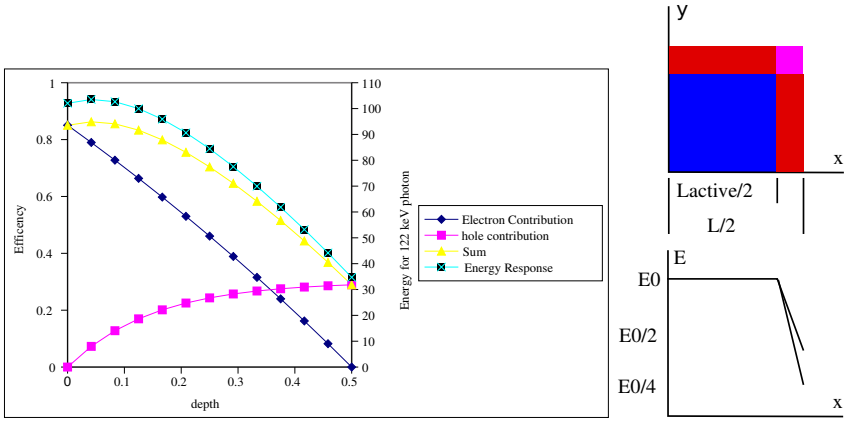

Figure 4.6. Typical charge collection profiles and charge sharing model. The charge collection diagram, left, shows contributions of each term in Equation 3.9 on the left axis and a poorly calibrated energy response on the right axis. The charge sharing diagram shows one quarter of a pixel, top right, and an energy response graph for the active and inactive areas, bottom right.

the left graph of Figure 4.6. Charge trapping was the only variation with depth modeled.

4.3.2 Linear Charge Sharing

A linear model was used to approximate charge sharing between pixels at all depths. Charge was assumed shared equally for ionizations that happened at half the pixel pitch. No charges were shared for ionizations that occurred within the active pixel, defined by the pixel electrode area. Charge sharing for ionizations in the inter-pixel regions was approximated as a linear function of distance between the active area and the mid-pixel point. Ionizations at the mid pixel point were reduced by half. For corners, between four pixels, the product of x and y linear approximations was used as shown in the bottom right graph of Figure 4.6. The minimum value returned is 0.25 of the potential induction at any depth.

4.3.3 Transport Code Interaction

Radiation transport codes call the model whenever an interaction occurs in the CZT volume. Sophisticated transport codes can check for multiple hits in the same group of

modules by the same or coincident particles. Information reported by the simulation can include real energy deposited, energy reported, real interaction position and pixel center location for each interaction. The entire simulation must be calibrated to match the actual detector response.

4.3.4 Simulation Calibration

The fixed noise contribution of electonic noise was estimated from actual detector response. Analog line noise voltage was measured with an oscilloscope and multiplied by an average pixel calibration slope to determine the noise level in keV present in the prototype.

Selection of material properties to best match detector response was performed in an iterative fashion. Reasonable starting values were chosen for hole and electron mobility and used for low-energy source simulations. Due to charge trapping and sharing, the model places the most probable energy response at an energy less than the actual photon energy. A linear calibration curve was made from the simulated spectra of three or more low energy sources. The calibrated spectra were then compared to measured prototype spectra and material constants were adjusted. Increasing electron mobility sharpened the peak and changed the shape of the tail. Changing the hole mobility changed the shape of the tail. The process was repeated until the spectral shape agreed to the user's satisfaction.

4.4 Data Analysis

Data from both the detector and simulations was histogrammed by energy and angle, backprojected and then compared. Gross angular error and resolution was computed for the data. Mean and mode average angular response were also computed and compared. Backprojected images were analyzed for angular error and resolution. Flow charts of the process are provided in Figure 4.7 and Figure 4.8 and explained below.

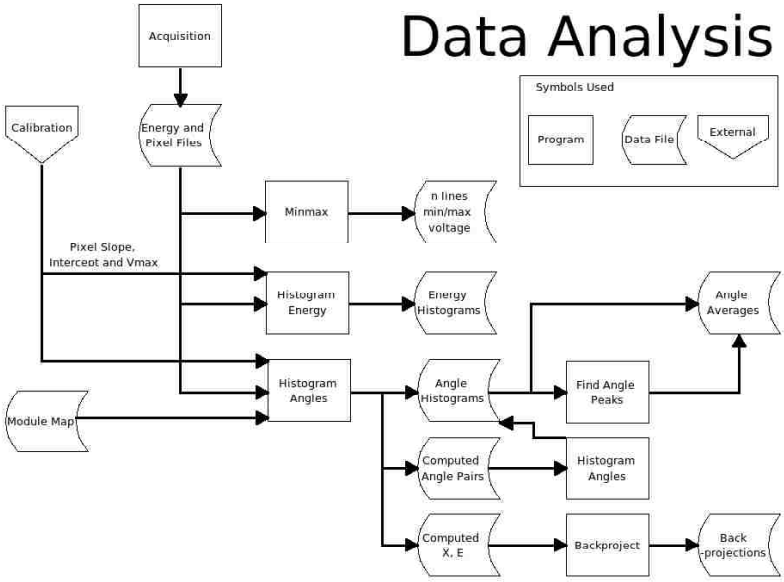

Figure 4.7. Simplified flow chart for data analysis.

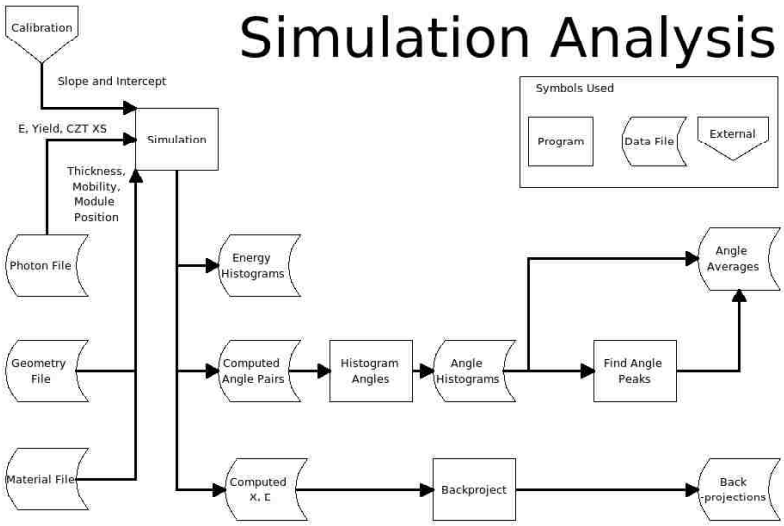

Figure 4.8. Simplified flow chart for simulation analysis.

4.4.1 Prototype Data

Position and energy information were determined from the recorded files. The multi-hit bit was checked and all multihit counts were rejected. Data that lacked a valid module number were also rejected. Pixel position was determined by table look up for pixel and module number. The differential energy signals were converted from voltage to energy in keV using the corresponding calibration curve for the particular pixel. Events with energy signals within the recorded noise level of the highest possible voltage for a given pixel were rejected to eliminate detector saturation.

Calculated Compton scatter angle estimates were compared to the actual geometric scatter angle. The geometric angle of coincident hits was estimated from pixel centers and the known source location. Two Compton angle estimates were computed from coincident hit energies and the known source energy as described in section 3.3. Gross resolution and gross error, scatter plots, histograms and averages were computed for all of these quantities.

An important tool for analysis was a two dimensional histogram, made from the calculated geometric angle and the energy estimate of scatter angle. All of the angles were binned one degree intervals by pixel position estimate and then according to energy estimate. An ideal histogram of this type would only have a 45° diagonal line where the angle estimates agree. A 30° scatter, for example, should yield a 30° pixel angle and a 30° Compton angle. Construction of a sample histogram is shown in Figure 4.9. The image demonstrates how the detector responds to scattered photons and what it reports to the observer. Vertical lines show how the detector responds to photons scattered at a given angle and horizontal lines graph what true scatter angles produce a reported scatter angle. In this particular case, the detector's response and report to 35° is graphed. The response graph plots the distribution of angular responses for a given true scatter angle. The report graph plots the distribution of true scatter angles reported as the same energy response angle. Mode and median averages and variance for detector responses and reports are visually apparent from these graphs.

Mean averages and variances of angle binned data were computed as one might

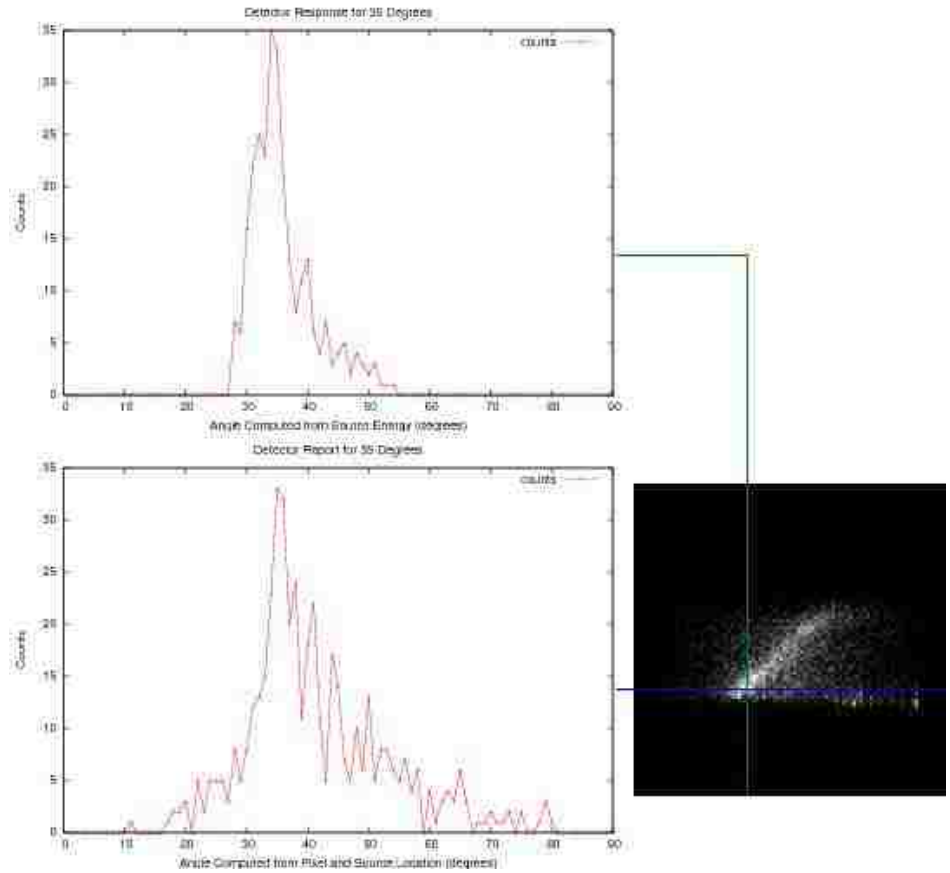

Figure 4.9. Histogram image construction for a Cs-137 data set. Vertical lines show detector response to specific scatter angles. Horizontal lines show what scatter angles are reported as any given angle the observer sees.

expect. The average and variance for each detector response bin and each detector report bin were computed by Equations 4.1 and 4.2.

$$\overline{x} = \frac{1}{n}\sum_{i=1}^{n} x_i \tag{4.1}$$

$$s^2 = \frac{1}{n-1}\sum_{i=1}^{n} (y_i - \overline{y})^2 = \frac{1}{n-1}\sum_{i=1}^{n} {y_i}^2 - \frac{n}{n-1}\overline{y}^2 \tag{4.2}$$

Mode averages and angular resolution of each response and report bin were determined from the histograms by the program Fityk [51]. The guess routine was used, which simply chooses the maximum value and determines the width at half that value.

Data was backprojected to a flat plane at the known source distance. An axis line was computed from the pixel locations and projected back to the plane. The appropriate ellipse or hyperbola branch for the cone angle was drawn around that point.

Backprojected images were analyzed for angular error and angular resolution visually and analytically. The point of maximum intensity was determined and the angular error between it and the actual source location was computed. The angular resolution was determined in both distance and degrees from the max point in the positive and negative X and Y directions. Marker overlays of origin, actual source location, a fifteen degree projection range and half intensity were applied to images for visual inspection. Finally, false color and topographical maps were prepared for select images.

4.4.2 Simulation Data

Position, energy and angle information were generated by the simulation for the detector geometry and source location. The rest of the analysis was the same as it was for the prototype data.

4.4.3 Backprojection and Image Analysis

A planar backprojection was used with a known plane distance. The plane was scaled at 4 mm per pixel and sized as a projection of 80° around each edge of the front detector

face. Ellipses and hyperbolas were drawn on the plane based on the angle of intersection of the cone axis with the plane and the cone angle. For both ellipses and hyperbolas major and minor axis lengths were solved from the cone angle and cone axis intersect points and front pixel normal intersect points. The first quadrant of the ellipse or hyperbola was constructed and then rotated to its correct position. Each pixel was checked before drawing to construct a smooth and continuous curve. Optionally, a 10 cm cross, source marker and 15 degree range marker were drawn on the image.

These images were analyzed by determining the maximum intensity point and half maximum intensity points, and comparing them to the known source location. The error between the maximum intensity point and the known source location was computed in millimeters and degrees. The half maximum intensity points were optionally marked and the distance to the maximum point was computed in both millimeters and degrees.

4.4.4 Comparison Methods

The prototype data was compared qualitatively and quantitatively. A reduced chi squared was computed for each kind of average value.

$$\chi^2 = \frac{1}{n-1}\sum_{i=1}^{n}\frac{\left(\overline{y}_{i,data} - \overline{y}_{i,simulation}\right)^2}{{\sigma^2}_{i,data} + {\sigma^2}_{i,simulation}} \tag{4.3}$$

In practice, the uncertainty of the averages due to calibration drift was much larger than the uncertainty due to measurement variance and this was used instead. Differences reflected by large chi squared values were investigated by comparing angle histogram images and looking for noise problems with the prototype data. Finally, image quality was subjectively assessed from the differences in data and simulation backprojection images.

4.5 Laboratory Materials and Software

The most important hardware and software components are listed in this section. Vendor and model information is given where possible.

4.5.1 Sources

The sources used for calibration and evaluation are given in Table 4.3 and Table 4.4.

Table 4.3. Calibration sources and major photon yields. Activity was known to 10%.

Isotope	Assay		Energy	Absolute
	Date	Activity (μCi)	(keV)	Yield (%)
Ba-133	4/1/2006	50	356	62.1
			81.0	34.1
			303	18.3
			384	8.9
			276	7.1
			53.1	2.2
			80	2.0
Cd-109	4/1/2006	100	88	3.6
Co-57	4/1/2006	1000	122	85
			136.5	10.7
I-123	3/15/2007	98.9	159	83.3
Tc-99m	3/28/2007	65	140.5	89.1

Table 4.4. Imaging sources and major photon yields. Activity was known to 10%.

Isotope	Assay		Energy	Absolute
	Date	Activity (μCi)	(keV)	Yield (%)
Co-60	4/1/2006	10	1173	100
			1333	100
Cs-137	4/1/2006	25	662	85.1
Na-22	4/1/2006	100	1275	100
			511	178

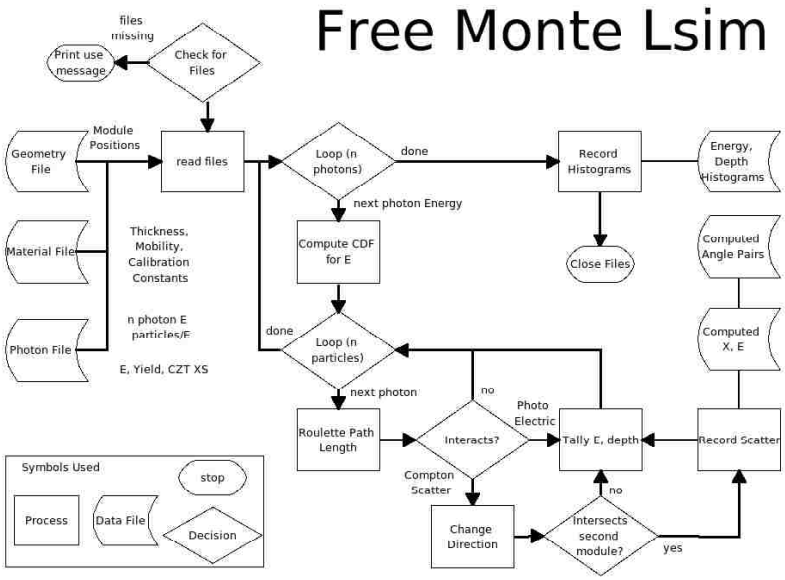

Figure 4.10. Simplified flow chart for Free Monte simulation.

4.5.2 Transport Codes

Free Monte is a simple uncollided flux transport code used for quick material evaluation and data verification. Only the first collision and direction change were tracked, so it only required the material cross sections for a single energy. The scattered photon was assumed to escape the front detector and interact in the second detector if the path crossed it. Uniform illumination of the front detector was assumed and a front pixel center rather than an actual location was sampled. The outputs were a position and energy file, an angle pairs file and histograms of energy and depth of interaction. A flow chart of the program is depicted in Figure 4.10. Interaction with the CZT model was described in Section 4.3.3.

4.5.3 Prototype Hardware

The front and side detectors shared power supplies:

- High voltage power supply, Spellman MP 1.5N24

- Low voltage power supplies from the LabRat system [50].

The front detector was made from these components from Orbotech Imaging Systems:

- Detector Link Board, DLB V1.101,
- Detector Access Board, DAB V1.00,
- CZT modules (2) with XaIm 3.3 ASICs
- LSU's Physics Electronics Development Group provided two carrier boards (LSU Physics EDB 5/1/2006) and a custom digital buffer board.

The side detector was made from these components from Orbotech Imaging Systems:

- Carrier board, DCB 5x5 V105
- Detector Link Board, DLB V1.101,
- Detector Access Board, DAB V1.10,
- CZT modules (2) with XaIm 3.2 ASICs,
- and a custom digital buffer board from LSU's Electronics Lab.

Trigger signals selected for detector hit, conditioned and counted by:

- Coincidence Detector, Ortec 418a,
- Tail Pulse Generator, Berkely Nucleonics Corp. (BNC BH-1)
- Counter, Ortec 871.

Analog Energy signals were acquired through:

- Analog BNC connection board, NI BNC-2110
- Analog DAQ, NI 6143

Digital module, pixel and multihit signals were acquired with:

- Screw terminal box, NI SCB68
- Digital IO Card, NI 6533

4.5.4 Prototype Software

A previous software set up for data acquisition was used with little modification [50]. Data acquisition was performed with the following software:

- Windows 2000, version 5.0(build 2195: Service Pack 4)
- LabVIEW 7 Express, Version 7.0 was used for DAQ control, module shift register programming, via RS232 serial port, and data acquisition.

Data analysis was performed with the custom software mentioned in section 4.4 and the following software, all provided by Debian GNU/Linux:

- Debian Etch, 2.6.18-4-686
- GCC gcc-4.1-base - The GNU Compiler Collection, gcc (GCC) 4.1.2 20061115 (prerelease)
- libgd2-xpm-dev - GD Graphics Library version 2.0.33-5.2
- libgsl0-dev - GNU Scientific Library (GSL) – development package, version 1.8-2 (Debian 4.1.1-21)
- OpenDX (IBM Visualization Data Explorer), 4.4.0-2
- GQview - A simple image viewer 2.0.1
- Gnumeric - GNOME spreadsheet application, 1.6.3
- Gnuplot - A command-line driven interactive plotting program, 4.0 patchlevel 0
- Fityk - general-purpose nonlinear curve fitting and data analysis, 0.7.6

CHAPTER 5

RESULTS OF DATA ACQUISITION AND ANALYSIS

5.1 Detector Calibration

The module performance degraded over the course of the project, but the prototype maintained linearity. Response amplitude declined and the low energy threshold increased. Figure 5.1 shows typical energy spectra for the final calibration set for the front detector. A Co-57 spectrum from preliminary measurements is included as an indication of the stability of peak structure over time. The spectra also show the module performance degradation, illustrated by the loss of response in the 50-100 keV range. The amplitude loss caused a 6 keV shift between the two calibrations. Figure 5.2 shows the slope and intercept for each pixel from the calibration. The average response was 22 keV/V with a zero intercept of 130 keV. Energy resolution was about 20% for I-123. Electronic noise on the analog output was about 0.2V peak to peak, which corresponds to 4.5 keV. The front background count rate was 21.9 $\pm$0.1 cps at the time of calibration, but this varied with detector module degradation. Calibration results for the side detector were similar but were not used in subsequent analysis and are not presented here.

Figure 5.3 shows the effect of side shielding on Co-57 energy spectra. Even though the CZT scatter cross section is relatively low at the primary photon energies of 122 keV and 136 keV, the count rate decreased about seven percent, from 643 $\pm$1 to 602 $\pm$1 cps. The different shapes of the spectra show the contribution of scattered photons which have a range of 90 keV to 136 keV.

5.2 Detector Saturation and Sensitivity

Figure 5.4 shows the results of the sensitivity tests. The two front modules have about the same sensitivity as a 1"x1" NaI crystal. Rough equivalency is shown between the prototype and the scintillation detector.

Figure 5.5 shows the results of the saturation test as pixel voltage histogram images. The maximum rate of detection with good energy resolution is about a count per pixel per

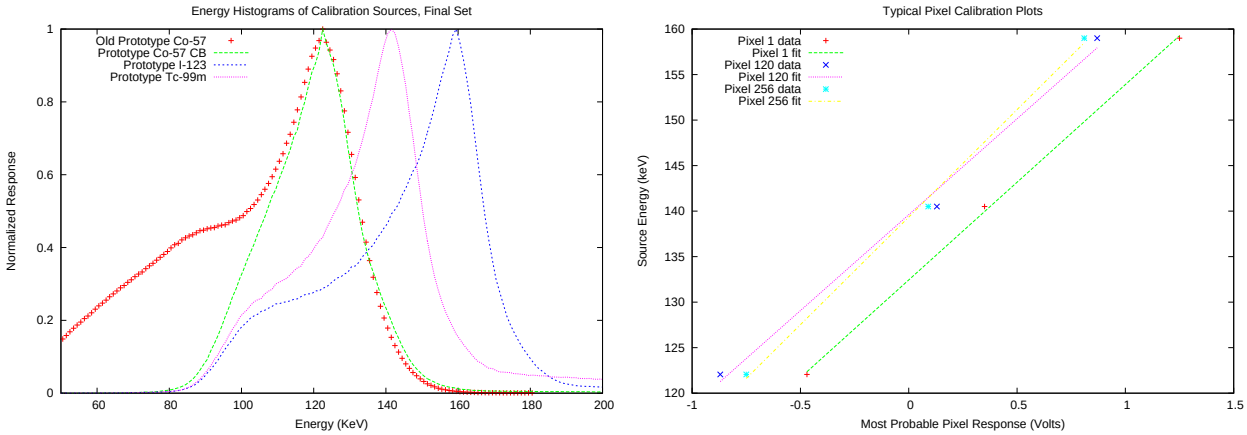

Figure 5.1. Energy calibration plots. The left shows energy spectra used for calibration. The right shows typical pixel calibration curves.

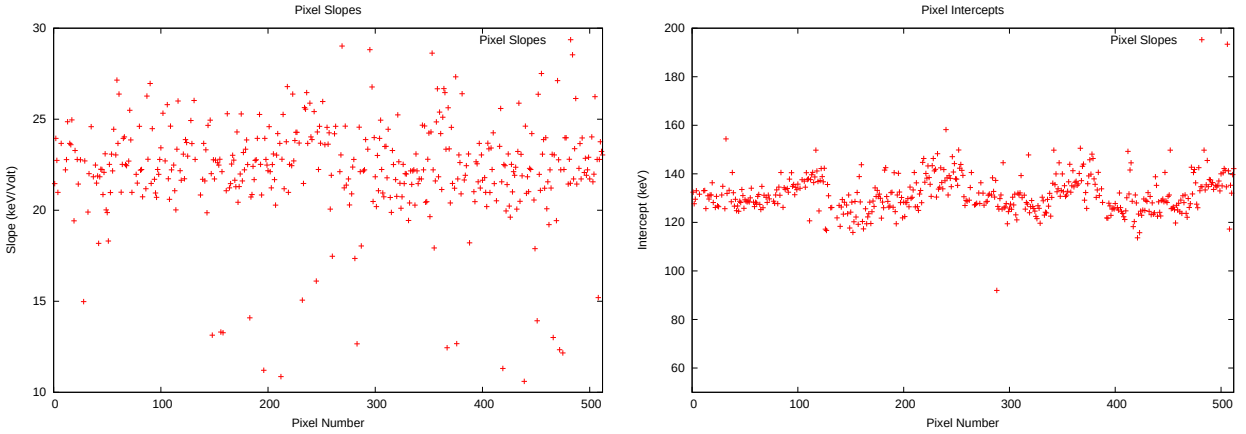

Figure 5.2. Plots of calibration slopes, left, and intercepts, right, for all pixels in the front detector for the second calibration.

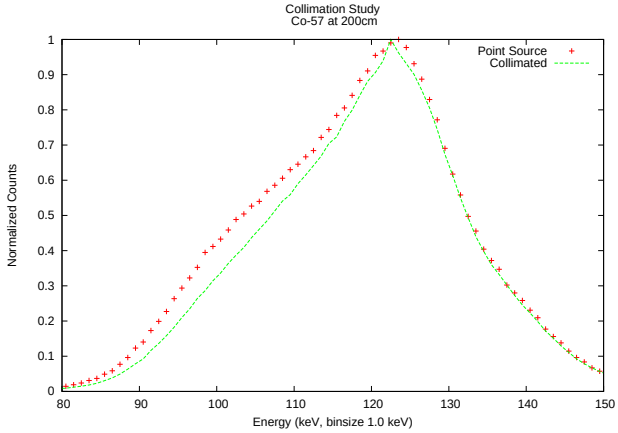

Figure 5.3. Effect of side shielding on the Co-57 spectra at 200 cm.

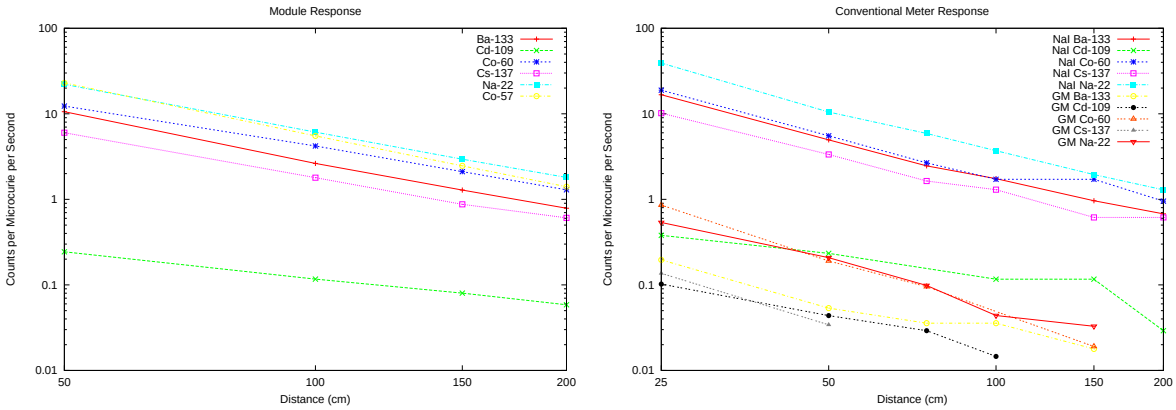

Figure 5.4. Sensitivity tests, plotting count rates as a function of source distance for the prototype, left, and two common meters, right. The conventional meters were a NaI(Tl) scintillation detector (NaI) and a Geiger-Müller counter (GM).

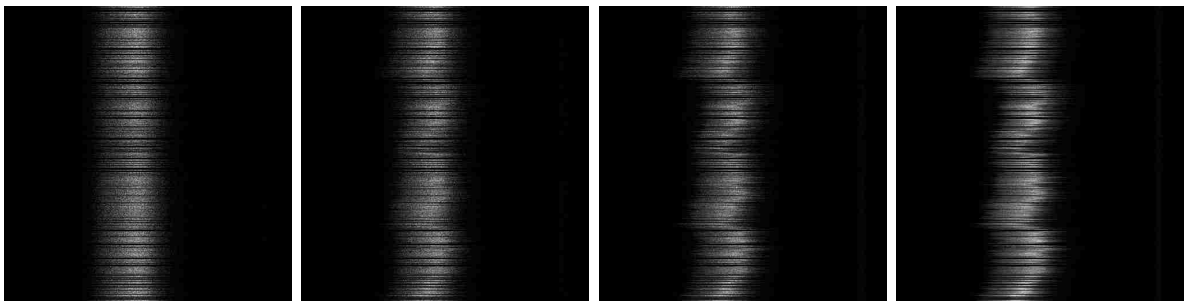

Figure 5.5. Co-57 saturation tests. From left to right, voltage histograms from Co-57 at 50, 100, 150 and 200 cm. Each pixel's voltage response is represented as a horizontal gray scale line in the images. The left side of each image corresponds to -5 V and the right side to 5 V.

second. For higher count rates, the modules respond as expected by the inverse square law, but energy discrimination is degraded. At 50 cm, every pixel responds with the same broad peaked spectrum. At 200 cm, the peaks are clean and will calibrate linearly with peaks from other sources. The count rate at 200 cm was roughly 600 cps, or a count per second per pixel, so this should be considered an upper bound. All subsequent data was taken at a total rate of less than 300 cps.

The count rates in this test were less than expected from solid angle calculations. This is because part of the photopeak and tail was lost by the time these tests were performed. Preliminary count rates agreed within uncertainty.

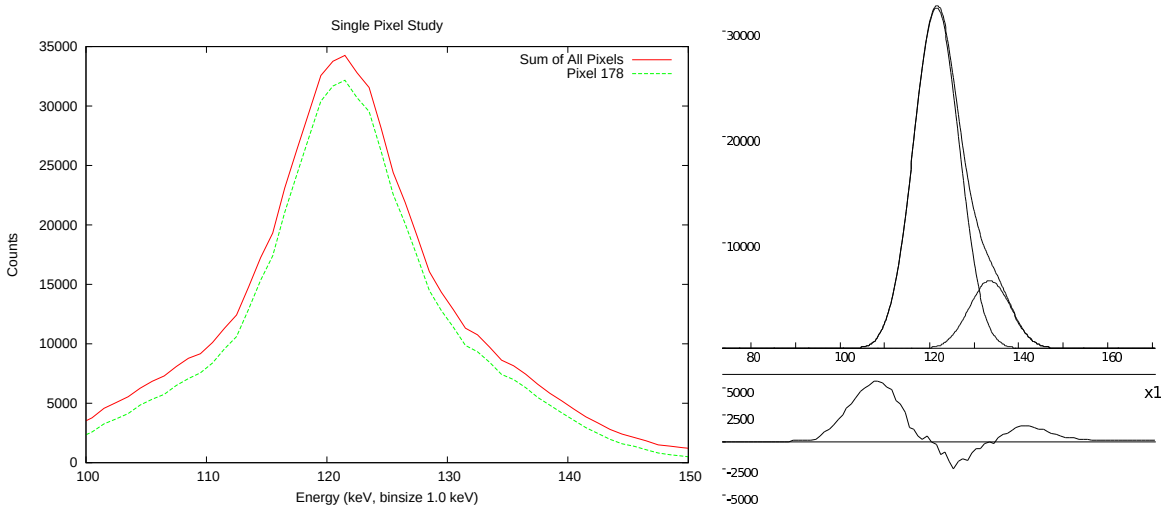

Figure 5.6. Energy spectra for a single representative pixel and the entire module (left) and fitted peak locations (top right) and residual error (bottom right) for the single pixel.

5.3 Single Pixel

Figure 5.6 shows energy spectra and fitted peaks for a 1 mm collimated Co-57 source beam aimed at a single pixel. The histogram plot shows the sum of all pixels and pixel 178, where the beam was aimed. Pixels around pixel 178 also responded, but the vast majority of response was from the target pixel. The fit places the peaks at 121.2 keV and 133.5 keV with FWHM values of 13 keV and 11 keV or 10% and 8%, respectively. The sum peak was fitted with peaks at 121.5 keV and 135.5 keV and have similar resolution.

5.4 Angle of Incidence

The observed energy resolution for a 2 mm collimated Co-57 source at all angles of incidence was about 16% FWHM and the results are graphed in Figure 5.7. The peak value of 124 keV instead of 122 keV is a result of the drift during the time between calibration and observation. Energy resolution was an increasing function of angle of incidence but not as much as expected from literature or simulations.

Both low energy cut off and floor scatter can account for the lack of energy resolution improvement with angle of incidence. Energy cut off, seen as an inflection point in the tail

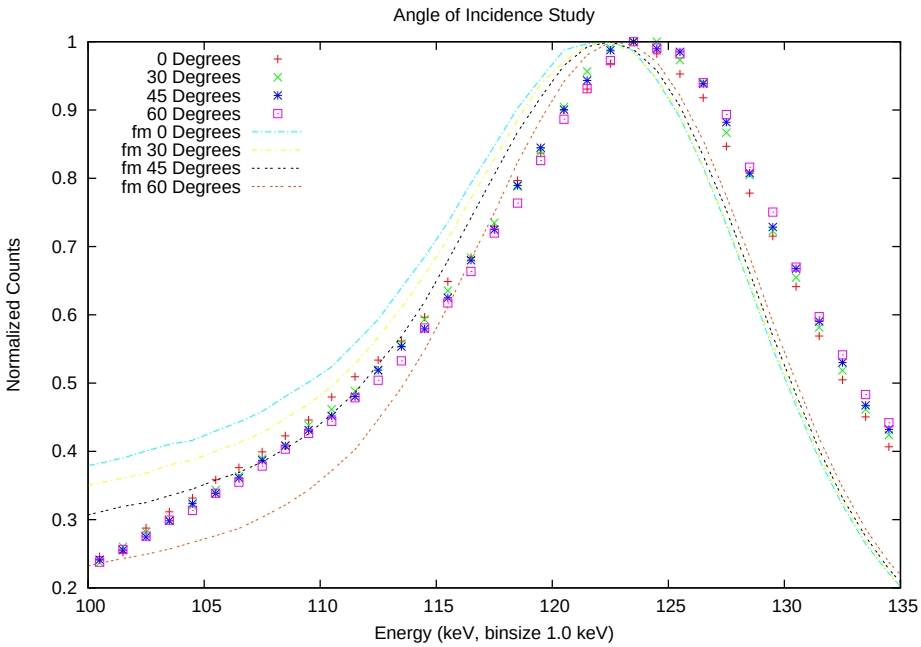

Figure 5.7. Co-57 angle of incidence study. Measured data is shown as symbols, Free Monte (fm) simulation as lines.

slope at 107 keV, masks some of the differentiation. It is likely that floor scatter increased with angle of incidence which increased counts in the tail as was demonstrated in Figure 5.3. A better test would minimize changes to irradiation geometry by rotating the detector instead of moving the source.

5.5 Imaging Results

Gross angular resolution was within twenty five degrees FWHM with an error less than the placement uncertainty where Compton and nominal scattering angles matched. The observer always sees a mode response that is within five degrees of the true angle. Data sets where Compton scatter angles did not match nominal scattering angles generally produced low quality data with large errors.

5.5.1 Gross Angular Resolution and Error

Figure 5.8 shows the histogram of the differences between angles based on position and Compton angles computed with an assumed energy for all isotopes at 50 cm. Where

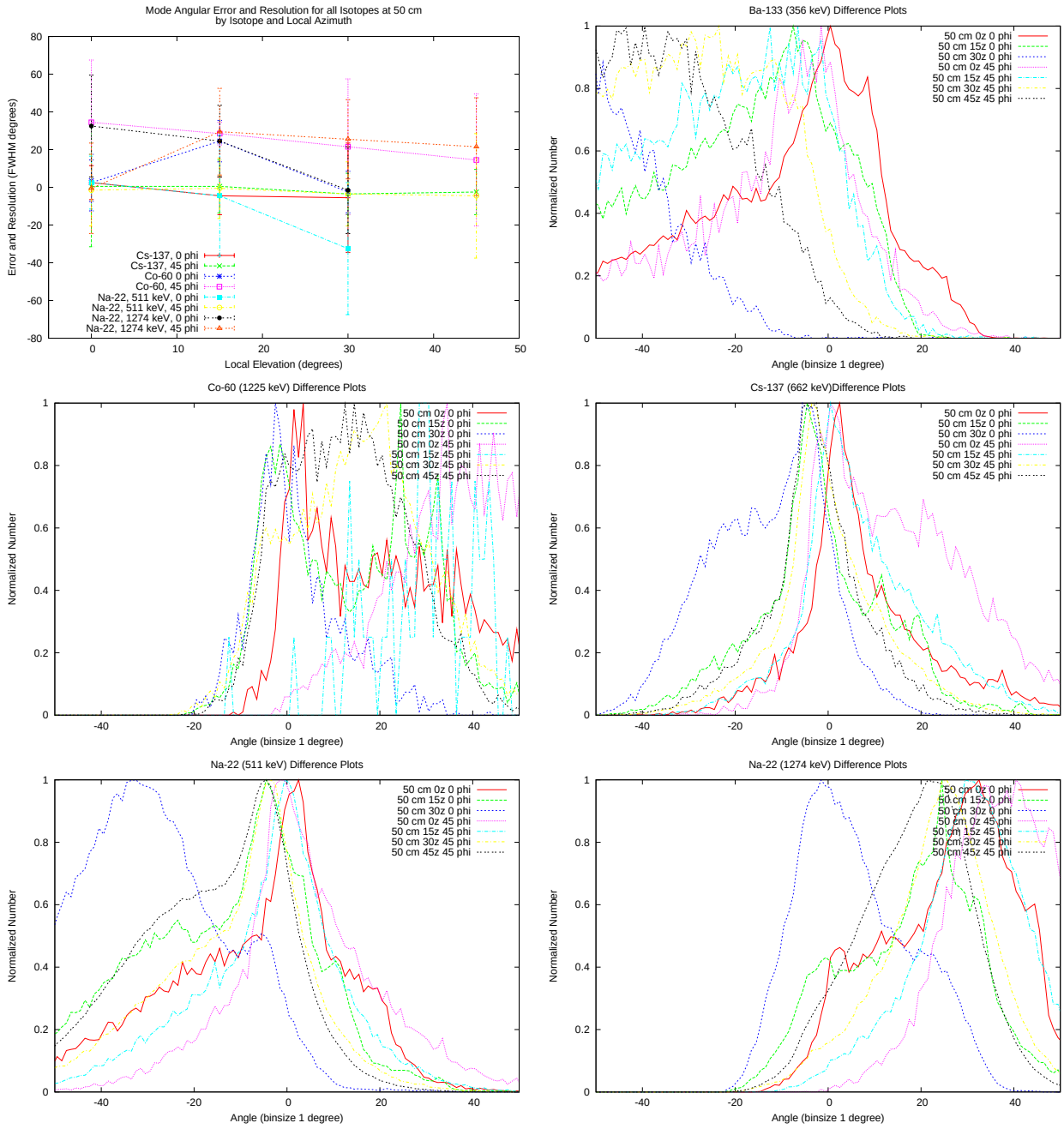

Figure 5.8. Mode angular error and FWHM resolution, top left, by isotope and azimuth as a function of elevation. The other five plots show histograms of angular error as a function of source position at 50 cm for the indicated isotope and assumed energy.

scattering geometry was aligned to deposit energy within the front detector's range, the mode error is less than the source placement uncertainty of 5° and angular resolution is less than 25° FWHM. For other cases, it's hit and miss. Table 5.1 lists results for the better positions. In all but one of these cases the error is less than 5° and angular resolution is less than 25° FWHM. Cs-137 and Na-22 both had positions with FWHM less than 15° centered close to zero angular error. Co-60 had two positions that were almost as good. Na-22 at $0phi, 15z$ and 511 keV, is the exception with an angular resolution of 32° FWHM because both 511 and 1274 keV photons have valid scatter angles at that position. For this position, the 1274 keV photon creates a large tail as seen in the bottom left gross error histogram of Figure 5.8. There are several intriguing borderline cases with poor alignment that do the same thing. Na-22 placed at $0\phi, 30z$ and $45\phi, 45z$, with an assumed energy of 511 keV, have distinguishable low error peaks but poor overall resolution due to the 1274 keV photon contribution. Cs-137 in the same positions performs better because Cs-137 only has one prominent photon energy. Ba-133 has more photons and consequently worse resolution. It has one reasonably aligned position at $45\phi, 0z$, and one borderline case at $0\phi, 0z$, both of which have less than 5° errors and 25° resolution.

Figure 5.9 shows histograms and averages for a Cs-137 data set. The first histogram shows differences between the Compton computed angle and the angle computed by source and pixel locations. The top right image is the detector response histogram as described in Section 4.4.1 and Figure 4.9. In it, one can see the response from several noisy pixels, which form vertical streaks along the lowest horizontal band of reported angles. The case shown has a 2° gross error and 9° FWHM gross resolution. For this data set, what the observer sees is mostly correct. Almost all of the scattering events occur in the detector's measurable range for the isotope, 30° to 60°, and the mode response of each observed angle bin is within 5° of the true angle within this range. Graphs like Figure 5.9 for the core data set of results can be found in Appendix A.

Table 5.1. Mode gross angular error and resolution for the positions of Table 4.2.

Isotope	Assumed Photon Energy (keV)	Source Position (ϕ,z in degrees)	Error (degrees)	Resolution (degrees FWHM)
Ba-133	356	45, 0	-1.5	24
Co-60	1225	0, 30	-2.5	11
Cs-137	662	0, 0	2.5	9
		0, 15	-4.5	10
		45, 30	-3.5	11
		45, 45	-2.5	12
Na-22	511	0, 0	2.5	14
		0, 15	-4.5	32
		45, 0	-1.5	19
		45, 15	-0.5	16
		45, 30	-3.5	17
Na-22	1274	0, 30	-1.5	23

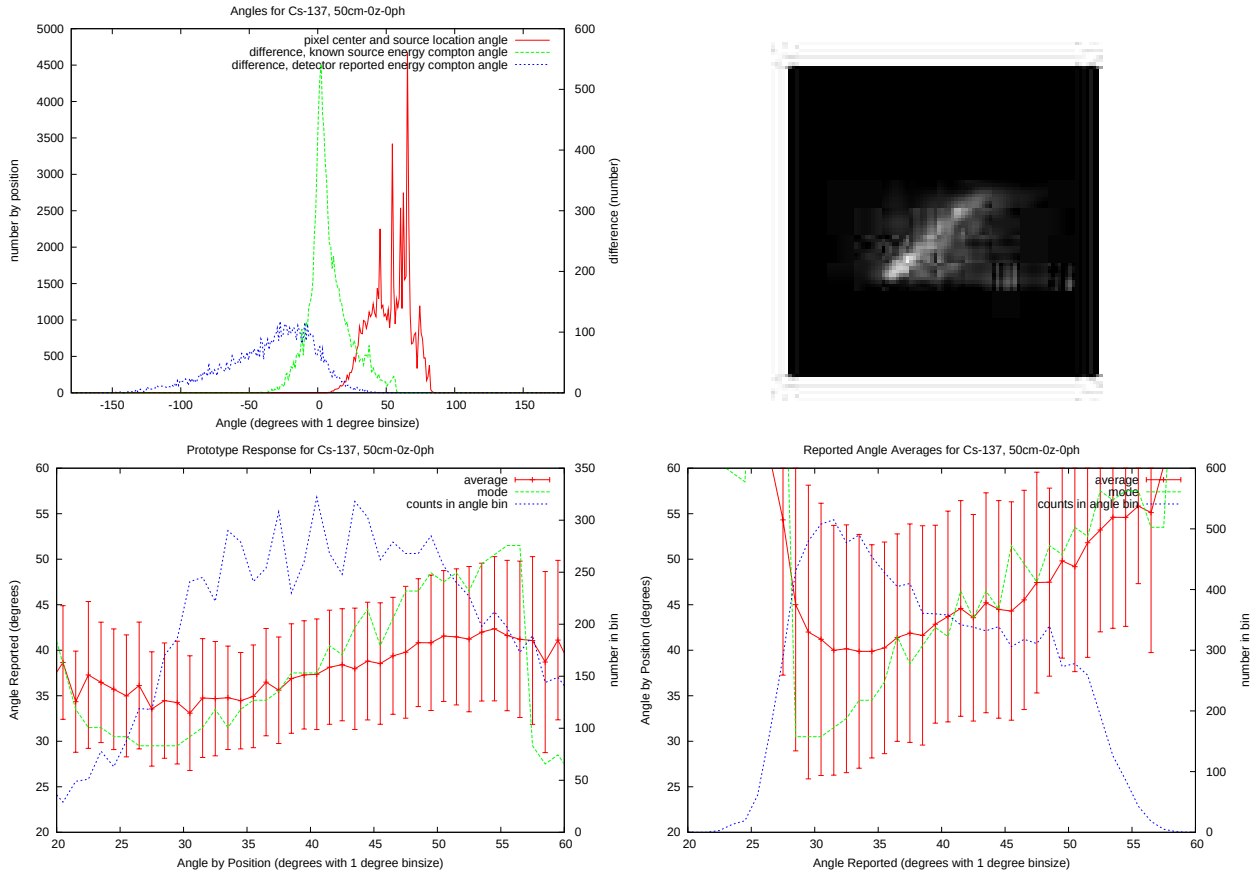

Figure 5.9. Cs-137 angular error histograms. Top diagrams are complete responses. Top left graph shows histogram of scattering angles and differences between the energy calculated and pixel geometry calculated angles. Top right is a 2D histogram image as explained in the text. The bottom graphs show mean and mode averages of vertical (left) and horizontal (right) profiles through the histogram image. The error bars around the mean averages represent one standard deviation.

5.5.2 Backprojection

Backprojected prototype data were not as good as desired, but the images are still informative and might be interpreted by a trained operator. Errors and resolution were larger for backprojections than the gross error and resolution of the previous section. Imaging was worse for sources further from axial positions than those on the axis and plane of symmetry, but the general shape always points to the source.

Backprojected image errors and resolution were worse than gross angular errors and resolution due to pixellation, axis errors and false intersections. All of the images had some degree of background intensity due to floor scatter and energy errors that were present in the gross angular results. Pixellation increased the angular resolution through axis errors. Energy errors from multiple photons created false intersections at incorrect locations. For sources located on the detector's plane of symmetry, the error was symmetrically distributed around the source point and the results follow the gross errors. For sources located away from of the detector's plane of symmetry, false intersection errors were distributed in a quarter ellipse pattern pointing back to the center of the projection plane. This caused several large angular position errors where the false intersections were more intense than the true source location even though acceptable gross results had been obtained. Backprojections of all core data can be found in Appendix.

Table 5.2, results for the the best aligned source positions, can be compared directly to the gross errors in Table 5.1. Ba-133 and all but one source position out of the prototype plane of symmetry become misses, with angular errors greater than 25°. Positions on the prototype plane of symmetry maintain errors of less than 8°. For them, resolution FWHM in the x direction is symmetric around the source and roughly two to three times larger than the gross angular resolution FWHM. Angular resolution is asymmetric in the y direction and comparable to gross resolution, which indicates a full detector configuration could match gross resolution in all directions. Interestingly, Co-60 had the smallest angular resolution.

Backprojection of centrally located sources yielded a point with 1/r fall off.

Table 5.2. Angular error and resolution for the source positions of Table 5.1. Resolution is given in ±x and ±y degrees half width at half maximum (HWHM) around the apparent source position to highlight asymmetry.

Isotope	Position (ϕ,z in degrees)	Angular Error (degrees)	Resolution (degrees HWHM)	
			$+x, -x$	$+y, -y$
Ba-133	45, 0	67	41, 29	10, 11
Co-60	0, 30	6	4, 3	3, 4
Cs-137	0, 0	1	13, 14	4, 5
	0, 15	8	18, 11	3, 7
	45, 30	7	4, 10	11, 15
	45, 45	70	53, 17	17, 23
Na-22 (511 keV)	0, 0	2	28, 30	8, 4
	0, 15	8	30, 33	23, 7
	45, 0	40	39, 42	15, 15
	45, 15	28	18, 69	19, 17
	45, 30	58	18, 69	19, 17
Na-22 (1274 keV)	0, 30	7	12, 18	6, 21

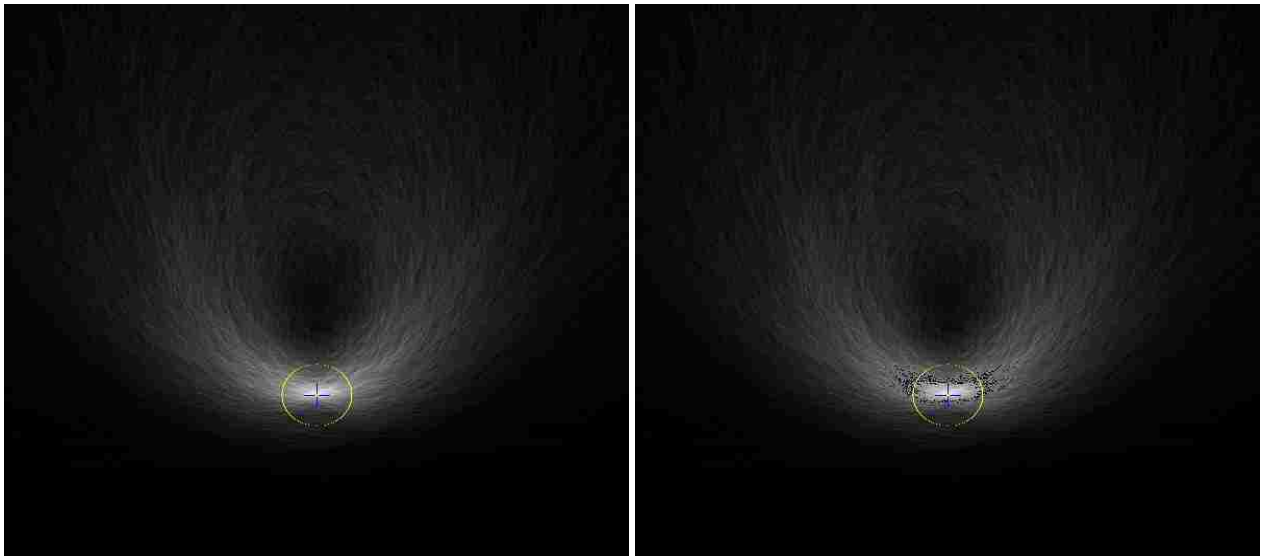

Figure 5.10. Backprojection for the example set of Figure 5.9 with an origin cross, source mark and 15° target outline. The cross corresponds to 10 cm on the projection plane. The right figure also has half maximum points marked.

Figure 5.10 shows a backprojection for the Cs-137 source, 50 cm in front of the detector center, and Figure 5.11 shows three dimensional views of the same information. The fall off pattern is clear when looking at the profile and orthogonal views. This symmetry was repeated for sources on the prototype's plane of symmetry and can be seen in all the images of Figure 5.12.

Visually, the images in Figure 5.12 also show the effects of source positioning and detector noise. As was seen in the gross results, Figure 5.8, the 0° and 15° elevation positions had significant scatter within the measurable energy range and little else. Backprojection of data from these positions yields bright spots within the 15° target that marks the true source position. Figure 5.10 right, shows that the half maximum points are mostly encompassed by the 15° target for the $0z$ position. The $15z$ position shows rings from a noisy pixel and this may be why this data's error is larger than the source placement uncertainty. These rings come from a noisy pixel in the side detector that creates false coincidences and many data points with the same set of incorrect axes. They may also be responsible for the spikes seen in the gross results for this position at 10° and

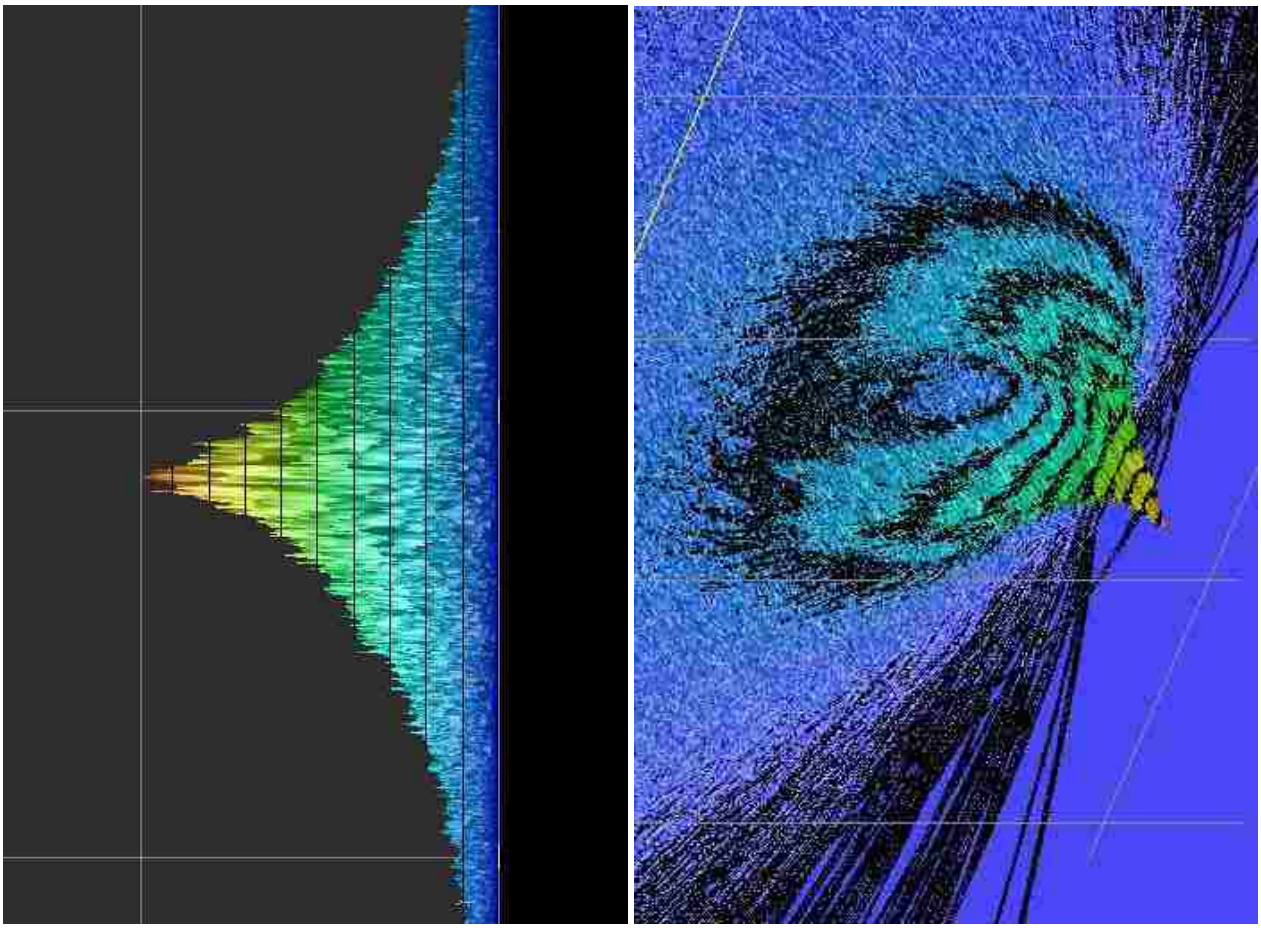

Figure 5.11. A view from -z direction, left, and an orthogonal view right of the data in Figure 5.10.

20° of error. The 30° elevation has much less scatter in the proper energy range and is not included in any of the tables because good results were not expected. The interesting peak from the gross results is lost in the fog created by a large tail. A source location is visible in the $30z$ location, but most of the image is blurred from scatter, accidental coincidence, and background radiation.

Backprojections from sources not on the prototype's plane of symmetry were more challenging. As shown in Figure 3.4, projected ellipses may have more than one point of intersection with projected hyperbolas and other ellipses. Even with perfect data, as shown in Figure 5.13, there is some streaking because the entire ellipse or hyperbola must be drawn and all of the axes point in the same direction. With poor energy resolution, the

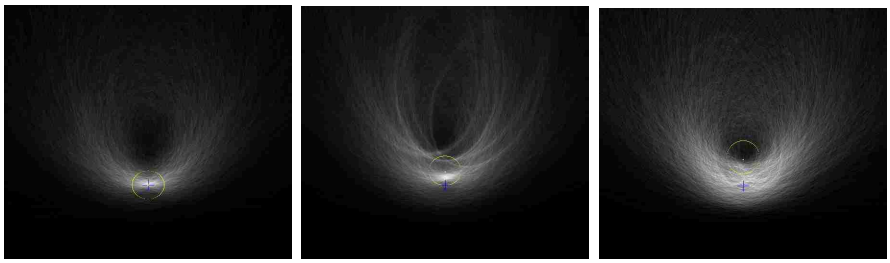

Figure 5.12. Backprojection images of a Cs-137 source in the detector's plane of symmetry. Source was placed at 50 cm, local azimuth 0° and left to right, local elevation 0°, 15° and 30°. The cross marks the origin and the circle marks 15° from source location.

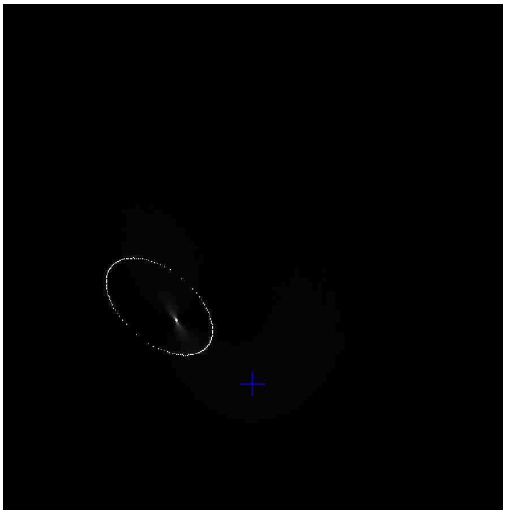

Figure 5.13. Perfect backprojection using source to pixel calculated angles instead of Compton energy angles for Cs-137 at 50 cm, $30z, 45\phi$. The cross marks 10 cm at the origin and the target marks 15° around the source location.

secondary intersections can be as prominent as the source location. This is demonstrated in Figure 5.14, a three dimensional view of Cs-137 at $45\phi, 30z$, a position which was expected to have a good backprojection and had good gross results of $-3.5°$ error and 11° gross FWHM. The concentration of false intersections in an elliptical pattern is apparent.

Figure 5.15 shows Cs-137 in the 45ϕ local azimuth positions. Of the four positions shown, the 30° and 45° local elevations had the most scatter in the front detector's energy range. Visually, the image for 30° local elevation was the most clear. The $45z$ position produced foggy imaging results that missed the real source. Both the $30z$ and the $45z$ positions had good errors and resolutions that were better than those of $0\phi, 0z$ and $0\phi, 15z$.

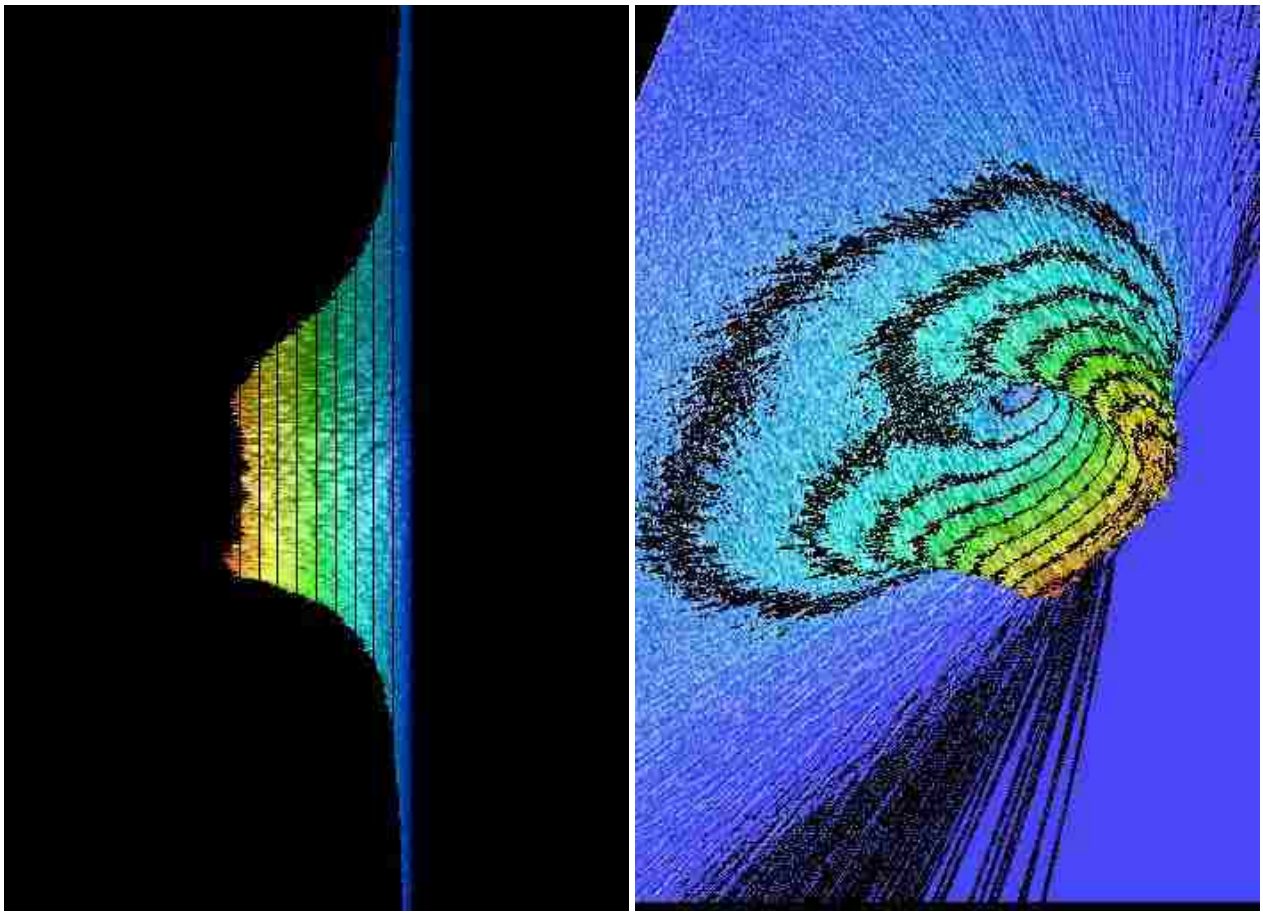

Figure 5.14. Bottom and orthogonal views of Cs-137 at 50 cm, $45\phi, 30z$. Compare to the same information in Figure 5.15.

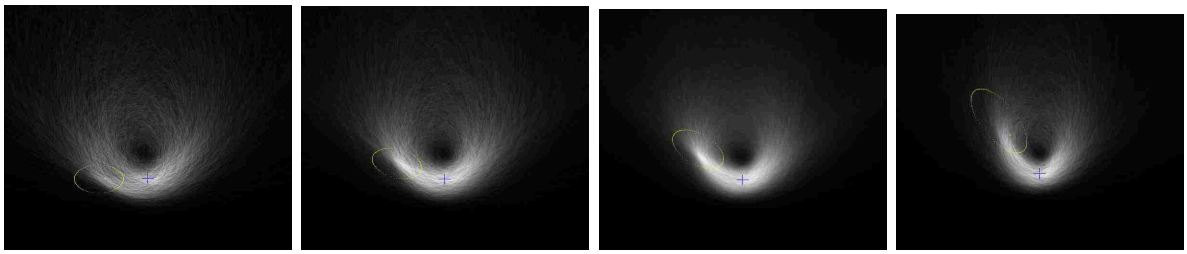

Figure 5.15. Backprojection images for Cs-137 out of the plane of device symmetry. The source was placed at 50 cm, local azimuth 45° and, left to right, local elevation 0°, 15°, 30° and 45°. The cross marks a 10 cm distance on the plane at the origin, the target marks 15° around the source location.

Table 5.3. Average response rates by isotope in cps/μCi at 50 cm. Assumed energies are given in parentheses.

Isotope	Rate
Ba-133 (365 keV)	0.012
Co-60 (1275 keV)	0.018
Cs-137 (662 keV)	0.018
Na-22 (511 keV)	0.051
Na-22 (1274 keV)	0.034

The 15° local elevation, which had poorer gross error and resolution, had visibly better imaging results than the 45° local elevation because false intersections are more important where cones are not projected symmetrically to distribute the error.

5.5.3 Response Rates

The rate of useful response, as defined in section 4.4.1, was between 0.5 and 7.0 angle-producing coincident cps at 50 cm. Table 5.3 summarizes the average rate of response by isotope for positions where scattering was within the detector's measurement range.

5.6 Simulation Results

The simulation provided an interesting approximation of the prototype data. Its energy response was similar to the prototype's and its calibration was also linear. L shaped simulations showed half the angular error and resolution as the prototype data. The box shaped simulation had errors and resolutions roughly equivalent to the prototype simulation, but produced visually better backprojections. A full set of images can be found in Appendix B.

5.6.1 Calibration

A reasonable fit for the calibration data was found using an electron trapping length of 2.9 cm and a 0.15 cm hole trapping length and 5 keV of fixed source noise. Simulation results are shown with prototype calibration data in Figure 5.16. The trapping length values are consistent with those reported in the literature and discussed in Section 3.5. The fixed noise was consistent with the 4.5 keV of line noise observed during calibration and a small margin to account for thermal noise, leakage and other effects. Like the prototype detector data, the simulation data produced a linear calibration.

5.6.2 Backprojection of Prototype Simulation Data

Backprojections of simulated data were similar to backprojections of prototype data. They lacked much of the noise and were relatively tighter but had the same structure and overall shape. Figure 5.17 and Figure 5.18 can be compared directly with Figure 5.12 and Figure 5.15. All of the data can be compared this way in Appendix B.

The angular error and angular resolution of the simulated data was about half that of the prototype data. This is visually apparent and is tabulated in Table 5.5 of Section 5.7.3. Differences between simulated and prototype data are due to scatter, false coincidence and background radiation in the prototype data and model simplifications. One interesting exception where the data is better than the simulation was Na-22 at $0\phi, 30z$ evaluated as 1274 keV, shown in Figure 5.19. This is a position where significant correct energy scatter

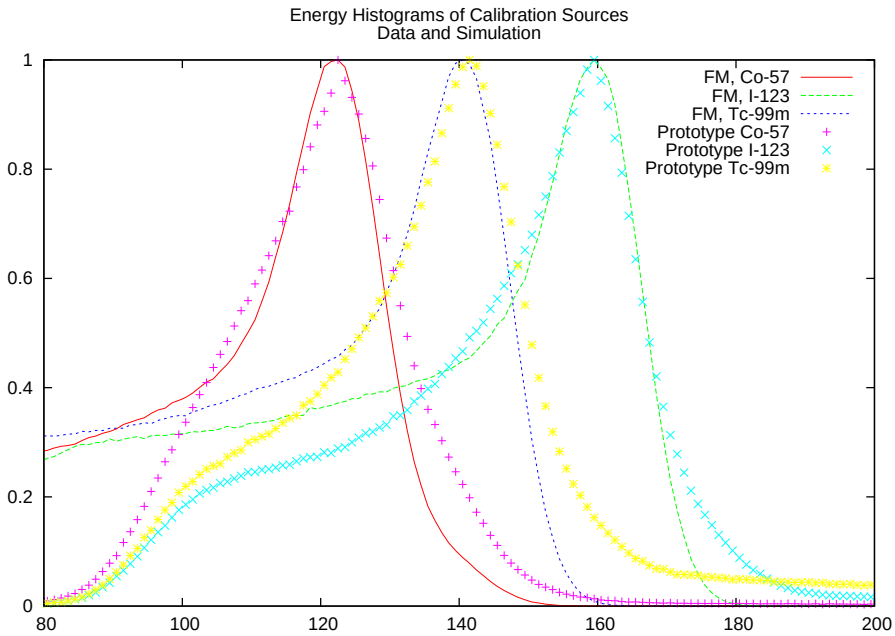

Figure 5.16. Free Monte (FM) simulated energy histograms compared to measured energy histograms.

was expected but the result should be masked by the 511 keV photon which also has significant scatter in the detector's energy range for the position, as discussed in Section 5.5.1. This may be because the prototype detector was able to detect higher energies than were modeled in the simulation limits, which is reflected in the vertical width of the histogram images. It's more likely a coincidence because the detector often over responds.

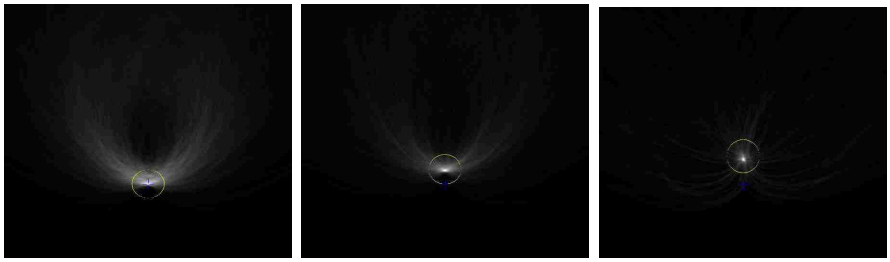

Figure 5.17. Cs-137 simulated at local azimuth 0° and, left to right, local elevation 0°, 15° and 30°. The cross marks 10 cm at the origin, and the target marks 15° around the source.

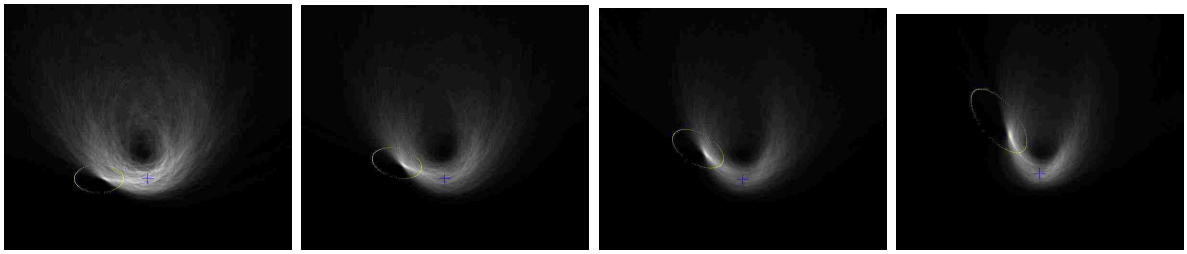

Figure 5.18. Cs-137 simulated at local azimuth 45° and, left to right, local elevation 0°, 15° and 30°. The cross marks 10 cm at the origin and the target marks 15° around the source.

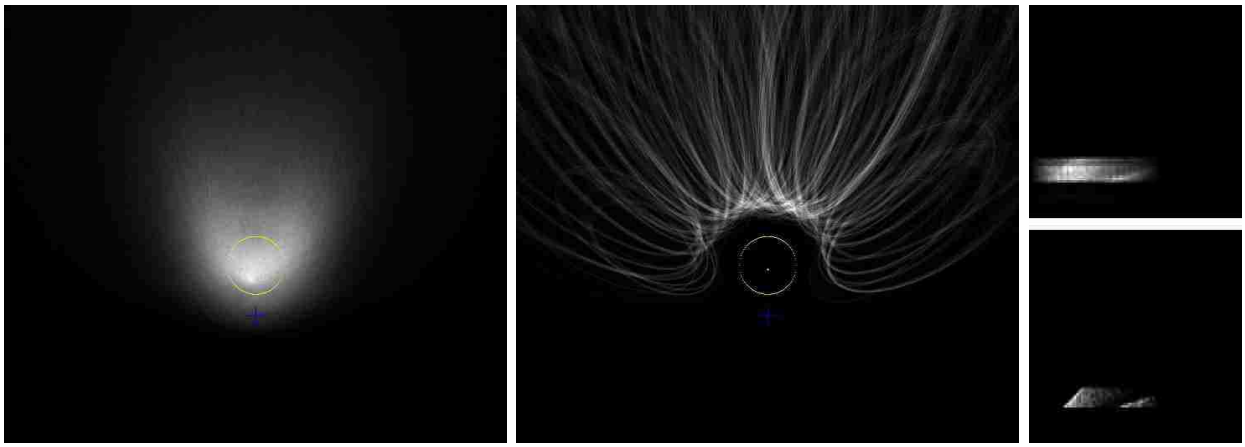

Figure 5.19. Backprojections and histograms of prototype, left and upper right, and simulation, middle and lower right, results for Na-22 (1274 keV) at 50 cm, $0\phi, 30z$.

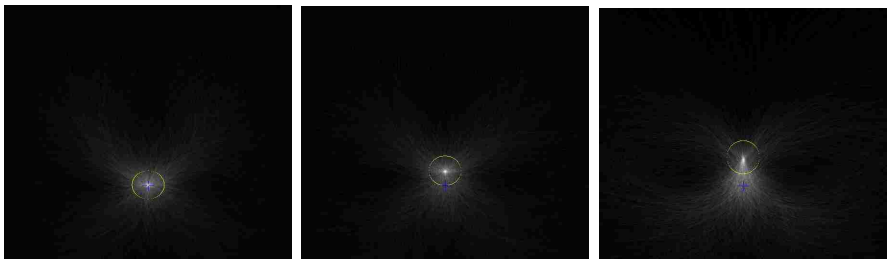

Figure 5.20. Cs-137 simulated for the box geometry at local azimuth 0° and, left to right, local elevation 0°, 15° and 30°.

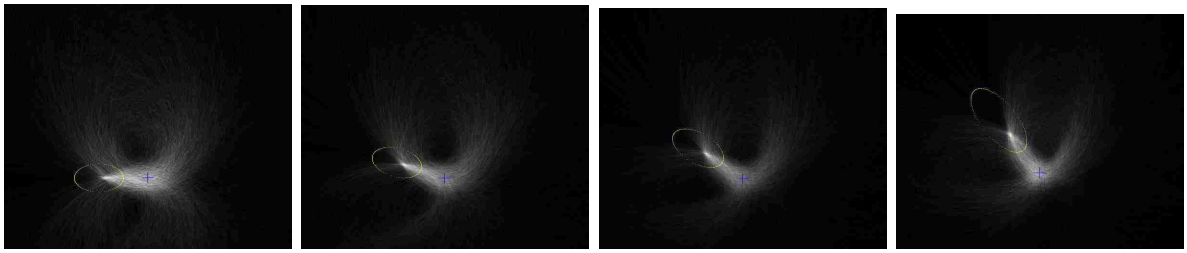

Figure 5.21. Cs-137 simulated for the box geometry at local azimuth 45° and, left to right, local elevation 0°, 15°, 30° and 45°.

5.6.3 Backprojection of Simulated Box Configuration

There are both visual and quantitative improvements for backprojected data from the box detector simulation. Figures 5.20 and 5.21 show box simulation results for Cs-137. Table 5.5 of Section 5.7.3 lists angular error and resolution for the core data set. Resolution improvement is mostly in the x direction and now both x and y FWHM are equivalent and symmetrical. The full box configuration distributes false intersections so they only reinforce each other along a line between the source and the center of the plane. Where the L shaped detector produced a cup shape, the box detector produces a spike. A notable exception to the general trend is Ba-133, which has so many low energy photons that imaging actually gets worse with a full detector shape. Na-22 works well with an assumed energy of 511 keV but misses at 1274 keV because the 511 keV photons dominate the images. Cs-137 and Co-60 both show marked improvements. A full set of images can be seen in Appendix B.

5.7 Comparison of Prototype and Simulation

5.7.1 Energy Resolution and Response

As can be seen in Figure 5.16, the simulated calibration data matches actual calibration data for collimated sources. Tailing in the simulation results is greater than that found in the measured data. This is partly because of the detector's energy cutoff and partly because of the simple model used for the simulation.

5.7.2 Mean and Mode Angles

Mean and mode angle comparisons are favorable within the expected energy and angle ranges for each isotope. For the data sets with good source detector scatter alignment, the averages follow the same trends but are separated by an offset due to energy drift. The reduced chi squared of the mean average response is less than 1.5 but the energy drift forced a large angle uncertainty, so this test is less conclusive than it could have been. Table 5.4 lists the results for the positions where good agreement should be expected. Positions with reduced chi squared differences greater than 1.5 for any other average usually had noisy pixel problems or larger offsets. Ba-133 at $0\phi, 0z$ and Cs-137 at $0\phi, 15z$ are examples of data sets with noisy side detector pixels. Cs-137 at $45\phi, 45z$ is an exception, where the reduced chi squared was large without a noisy pixel. Some near miss positions, such as Cs-137 at $0\phi, 30z$ and Na-22 (511 keV) at $45\phi, 45z$, are not listed but were reasonably good matches between simulation and experiment. Positions with better and worse scatter overlap had better and worse agreement due to random coincidences, background radiation and scatter not present in the simulation. Some positions show unusually good reduced chi squared because of the large uncertainty used.

Figure 5.22 shows the mean and mode angles for Cs-137 at 50 cm, $0\phi, 0z$. As described in Section 4.4.1, the left set of graphs shows mean and mode responses for each true angle bin and the right set of graphs shows mean and mode angles for each bin the detector reports to the observer. The simulated mean and mode follow the correct results better than the prototype detector, but the detector mode is never more than five degrees away from the true angle. A complete set of graphs can be found in Appendix A.

Table 5.4. Reduced chi squared difference between prototype and simulated mean and mode averages for the source positions of Table 5.1.

Isotope	Position (ϕ,z in degrees)	Mean		Mode	
		Response	Report	Response	Report
Ba-133	45, 0	1.3	3.0	1.7	NA
Co-60	0, 30	0.8	0.9	1.9	1.7
Cs-137	0, 0	0.3	0.7	0.7	NA
	0, 15	0.6	3.5	7.4	8.0
	45, 30	1.0	1.3	0.4	0.3
	45, 45	1.0	2.1	0.4	0.4
Na-22 (511 keV)	0, 0	0.2	1.0	0.4	1.5
	0, 15	0.3	0.7	1.6	2.8
	45, 0	0.9	0.3	0.6	0.6
	45, 15	0.9	0.2	0.2	0.1
	45, 30	1.2	0.2	0.3	0.2
Na-22 (1274 keV)	0, 30	1.0	2.9	0.6	0.6

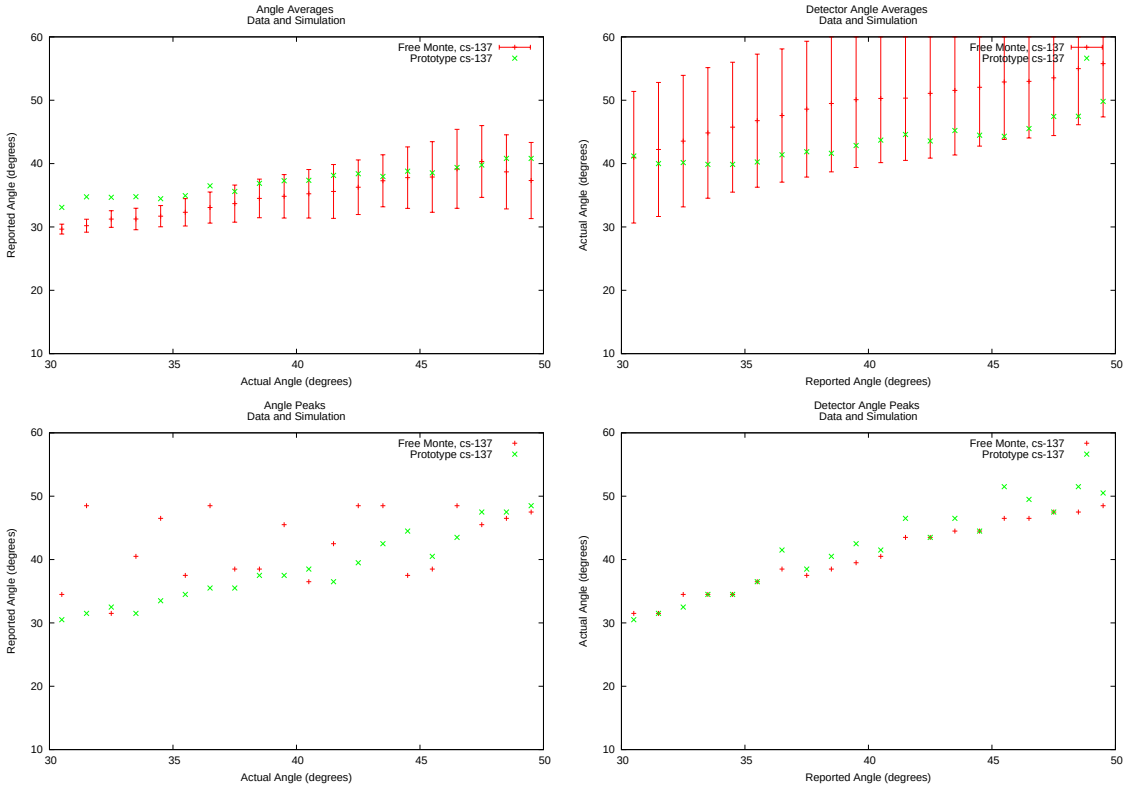

Figure 5.22. Observered and simulated mean, top row, and mode, bottom row, angles from Cs-137 at 50 cm normal to the detector. The left graphs are detector response, the right are detector reports as explained in Section 4.4.1.

5.7.3 Backprojection

Backprojections of simulated data were remarkably similar to the backprojections of actual data. As mentioned in Section 5.6.2, the simulated data had similar structure and shape with about half the angular error as the actual data for the set expected to have the best results. The similarity of shape and structure of backprojection was seen in all of the data even where the expected result would be noise and there is no apparent source location. The shapes made are indicative of the direction to the source and a trained operator should be able to interpret them and gain useful direction information. A full set of backprojections can be found in Appendix B. Table 5.5 lists the imaging error and resolution of the prototype data, L-shaped prototype simulation data and the box simulation data.

Table 5.5. Image error and resolution for positions of Table 5.1. The resolution is the average of x and y resolution. Errors greater than 25 degrees are considered a miss.

Isotope	Position (ϕ,z in degrees)	Error (degrees), Resolution (degrees FWHM) Prototype	L Simulation	Box Simulation
Ba-133	45, 0	miss	miss	miss
Co-60	0, 30	6,7	1,7	2,8
Cs-137	0, 0	1,18	1,10	1,8
	0, 15	2,20	1,6	1,6
	45, 30	7,20	1,7	0,5
	45, 45	miss	1,9	0,6
Na-22 (511 keV)	0, 0	2,34	1,12	1,8
	0, 15	8,46	1,11	1,10
	45, 0	miss	2,21	1,36
	45, 15	miss	1,7	1,9
	45, 30	miss	1,7	1,7
Na-22 (1274 keV)	0, 30	7,29	25,5	miss

CHAPTER 6

CONCLUSION

An electronically collimated prototype detector was built with inexpensive, commercially available CZT modules. Sensitivity was roughly equivalent to a common hand held 1“ x1” NaI(Tl) meter. Its overall angular error was less than 7°, and generally less than source placement uncertainty. Its angular resolution was between 20° and 40° for several common isotopes with energies between 511 keV and 1333 keV. Prototype data and backprojections were used to verify a simple three dimensional model of charge induction in pixellated CZT using an uncollided flux transport code. Further detector geometry studies can be carried out with this model using more sophisticated transport codes.

The hypothesis, “A portable CZT detector should be able to calculate the direction, within twenty-five degrees, to a 0.1 mCi source with an energy range of 70 keV to 2 MeV at three meters distance in thirty seconds,” was false using the prototype system. Hundreds of modules would be required to meet these stringent requirements even if generous imaging assumptions are made. However, this failure does not make the prototype impractical and much can be done to improve the system.

6.1 System Improvements

The most important improvement is sensitivity and this can be done by increasing solid angle and improving energy response. Because the energy range of interest mostly corresponds to forward scattering, the best improvement in sensitivity comes from decreasing the lower limit of detection. Raising the upper limit would also be helpful, especially for higher energy photons. Decreasing detector thickness will improve energy resolution and response. A more functional side detector would also improve efficiency because it or an external calorimeter could be used to estimate better the energy of the primary photon. Every photon could be utilized from multiple energy sources without the errors and blurring that was apparent in the Ba-133 and Na-22 results.

Specific to our detector system, an improvement would be better support electronics.

Electronic noise, particularly noisy pixels, should be eliminated. Better amplification closer to the modules would help. ASIC logic that allows multiple hits to be read out at the same time would improve efficiency and spatial and energy resolution. Shared charges could be summed and hit locations with sub pixel accuracy would be possible if the ASICS could report multiple hits at once.

For the applications envisioned, improvements to geometric accuracy and energy resolution are secondary to sensitivity because these were essentially good enough for direction finding and source location.

6.2 System Applications

The system is practical for hot source location and could be useful as a room or warehouse monitor. Curie activity sources can be detected at five meters in five seconds with three modules to each side of the box, little more than we used in the prototype. This would be very useful on a remote access robot in situations where optical visibility might be impeded. A larger panel type detector with 100 modules per side could detect a typical 330 μCi brachytherapy seed at five meters in less than five minutes. At 10 cm, the system can find 330 μCi seeds within five seconds, so the prototype could make a good, short range direction finding detector without modification. A twenty-five module per side prototype could detect the same source at 50 cm in ten seconds. Although large numbers of modules would be less than portable, a substantial increase in sensitivity is probably necessary for long distance stand off detection. Thus, using this system as a portable detector should be restricted to short range applications.

REFERENCES

[1] R. G. Helmer. *Gamma-Ray Spectrum Catalogue, fourth edition.* Idaho National Engineering & Environmental Laboratory, PO Box 1625, Idaho Falls, Idaho 83415-2114, 1998.

[2] C. Scheiber and G. Giakos. Medical applications of CdTe and CdZnTe detectors. *Nuclear Instruments and Methods in Physics Research*, A458:12–25, 2001.

[3] A.L. Lackie. A directional algorithm for the electronically collimated radiation detector. Master's thesis, Louisiana State University and Agricultural & Mechanical College, Baton Rouge, LA, 2007.

[4] Y. F. Du, Z. He, G. F. Knoll, D. K. Wehe, and W. Li. Evaluation of a Compton scattering camera using 3-D position sensitive CdZnTe detectors. *Nuclear Instruments and Methods in Physics Research*, A457:203–211, 2001.

[5] S.V. Guru, Z. He, and D.K. Wehe. Portable high energy gamma ray imager. *Nuclear Instruments and Methods in Physics Research*, A378:612–619, 1996.

[6] W. Wang, J. McGlothlin, D. Smith, and K.L. Matthews. Evaluation of a radiation survey training video developed from a real-tme video radiation detection system. *Health Physics*, 90(2):S33–S39, 2006.

[7] D. Haslip and J. R. Mercier. A NATO exercise on radiological sampling. *Health Physics*, 87(5), 2004.

[8] K. Fujimoto. A simple gamma ray direction finder. *Health Physics*, 91(1):29–35, 2006.

[9] E. Sajo. Personal communication, 2006.

[10] M. Woodring, D. Beddingfield, D. Souza, G. Entine, M. Squillante, J. Christian, and A. Kogan. Advanced multi-dimensional imaging of gamma-ray radiation. In *Proceedings of the Tenth Symposium on Radiation Measurements and Applications*, volume 505 of *Nuclear Instruments and Methods in Physics Research Section A: Accelerators, Spectrometers, Detectors and Associated Equipment*, pages 415–419, 2003.

[11] R. Todd, J. Nightingale, and D. Everett. A proposed γ camera. *Nature*, 251(5471):132–134, 1974.

[12] M. Singh and R. Brechner. Experimental test-object study of electronically collimated SPECT. *Journal of Nuclear Medicine*, 31(2):178–186, 1990.

[13] J. Durkee Jr, P. Antich, E. Tsyganov, A. Constantinescu, J. Fernando, P. Kulkarni, B. Smith, G. Arbique, and M. Lewis. SPECT electronic collimation resolution enhancement using chi-square minimization. *Physics in Medicine and Biology*, 43:2949–2970, 1998.

[14] A. Bolozdynya, C. Ordonez, and W. Chang. A concept of cylindrical Compton camera for SPECT. In *Conference Record of 1997 IEEE Nuclear Science Symposium and Medical Imaging Conference*, volume 2, pages 1047–1051, 1997.

[15] E. Porras, B. Escat, J.M. Benlloch, D. Kadi-Hani, S. López, N. Pavón, J.A. Ruiz, F. Sáncheza, and A. Sebasti. Portable mini gamma camera for medical applications. *Nuclear Instruments and Methods in Physics Research*, A486:186–190, 2002.

[16] T. Schlesinger and R. James. *Semiconductors for Room Temperature Nuclear Detector Applications*, volume 43 of *Semiconductors and Semimetals*. Academic Press, San Diego, 1995.

[17] T. S. Hickernell, H. H. Barrett, H. B. Barber, J. M. Woolfenden, and J. N. Hall. Probability modelling of a surgical probe for tumour detection. *Physics in Medicine and Biology*, 35(4):539–559, 1990.

[18] M. Wernick and J. Aarsvold. *Emission Tomograpy, The Fundamentals of PET and SPECT*, pages 383–419. Elsevier Academic Press, San Diego, 2004.

[19] J. D. Kurfess. Compton scatter imaging in astrophysics. *IEEE Transactions on Nuclear Science*, 45(3):936–942, 1998.

[20] J. Ryan, R. Andritschke, P. F. Bloser, J. P. Cravens, M. Cherry, G. Di Cocco, T. G. Guzik, D. H. Hartmann, S. Hunter, G. Kanbach, R. M. Kippen, J. Kurfess, J. R. Macri, M. L. McConnell, R. S. Miller, W. S. Paciesas, B. Phlips, V. Reglero, J. G. Stacy, M. Strickman, W. T. Vestrand, J. P. Wefel, E. Wulf, A. Zoglauer, and A. Zych. MEGA: the next generation medium energy gamma-ray telescope. In *Proceedings of the SPIE, UV and Gamma-Ray Space Telescope Systems.*, volume 5488, pages 977–987, 2004.

[21] B. L. Graham, B. F. Phlips, J. D. Kurfess, and R. A. Kroeger. Background and sensitivity simulation of a space based germanium Compton telescope. In *Conference Record of the 1997 IEEE Nuclear Science Symposium and Medical Imaging Conference*, volume 2, pages 325–329, Albuquerque, NM, 1997.

[22] J. LeBlanc and D. Wehe. A Compton camera for low energy gamma ray imaging in nuclear medicine applications. Master's thesis, Univ. of Michigan, 1999.

[23] A. Hero, A. Suave, and T. Kragh. Image reconstruction for a novel Compton scatter tomograph. In *Proceedings of the IEEE Asilomar Conference on Signals, Systems, and Communications*, pages 328–332, 2000.

[24] K. Vetter, M. Burks, C. Cork, M. Cunningham, D. Chivers, E. Hull, T. Krings, H. Manini, L. Mihailscu, K. Nelson, D. Protic, J. Valentine, and D. Wright. High-sensitivity Compton imaging with position-sensitive Si and Ge detectors. *Nuclear Instruments and Methods in Physics Research*, A579:363–366, 2007.

[25] E. A. Wulf, N. I Johnson, R. A. Kroeger, J. D. Kurfess, and B. F. Phlips. Germanium strip detector Compton telescope using three dimensional readout. *IEEE Transactions on Nuclear Science*, 50(4):57–61, 2003.

[26] D. Xu and Z. He. Filtered back projection in 4π Compton imaging with a single 3D position sensitive CdZnTe detector. *IEEE Transactions on Nuclear Science*, 53(5):2787–2795, 2006.

[27] C.E. Ordonez, A. Bolozdynya, and W. Chang. Dependence of angular uncertainties on the energy resolution of Compton cameras. In *Conference Rececord of the 1997 IEEE Nuclear Science Symposium and Medical Imaging Conference*, volume 2, pages 1122–1125, Albuquerque, NM, 9-15 November 1997.

[28] C.E. Ordonez, A. Bolozdynya, and W. Chang. Doppler broadening of energy spectra in Compton cameras. In *Conference Record of the 1997 IEEE Nuclear Science Symposium and Medical Imaging Conference*, volume 2, pages 1361–1365, Albuquerque, NM, 9-15 November 1997.

[29] C.E. Ordonez, W. Chang, and A. Bolozdynya. Angular uncertainties due to geometry and spatial resolution in Compton cameras. *IEEE Transactions on Nuclear Science*, 46:1142–1147, 1999.

[30] A. Zoglauer and G. Kanbach. Resolution of next generation Compton telescopes. In J. Truemper and H. Tananbaum, editors, *Proceedings of SPIE 4851 (2003) X-Ray and Gamma-Ray Telescopes and Instruments for Astronomy*, pages 1302–1309. SPIE, 2002.

[31] J. Kurfess, W. Johnson, R. Kroeger, and B. Phlips. Considerations for the next compton telescope mission. *AIP Conference Proceedings*, 510:710, 2000.

[32] A. Akyüz, D. Bhattacharya, T.J. ONeill, J. Samimi, and A. Zych. Enhanced performance of an electron tracking Compton gamma-ray telescope. *New Astronomy*, 9:127–135, 2003.

[33] G. Kanbach, R. Andritschke, and A. Zoglauer. Development and calibration of the tracking Compton/pair telescope MEGA. *Nuclear Instruments and Methods in Physics Research*, A541:310–322, 2005.

[34] F. Zhang, Z. He, G. Knoll, D. Wehe, and J. Berry. 3-D position sensitive CdZnTe spectrometer performance using third generation VAS/TAT readout electronics. *IEEE Transactions on Nuclear Science*, 52(5):2009–2016, 2005.

[35] A.L. Lackie, K.L. Matthews, B.M. Smith, W.H. Hill, W.-H. Wang, and M.L. Cherry. A directional algorithm for an electronically-collimated gamma-ray detector for intraoperative localization of radiation sources. *Medical Physics*, 33(6):1983, 2006.

[36] Z. He, G.F. Knoll, D.K. Wehe, and J. Miyamoto. Position-sensitive single carrier CdZnTe detectors. *Nuclear Instruments and Methods in Physics Research*, A388:180–185, 1997.

[37] Z. He, W. Li, G. F. Knoll, D. K. Wehe, J. Berry, and C. M. Stahle. 3-D position sensitive CdZnTe gamma-ray spectrometers. *Nuclear Instruments and Methods in Physics Research*, A422:173–178, 1999.

[38] F. Zhang, Z. He, D. Xu, G. Knoll, D. Wehe, and J. Berry. Improved resolution for 3-D position sensitive CdZnTe spectrometers. *IEEE Transactions on Nuclear Science*, 51(5):2427–2431, 2005.

[39] G. F. Knoll. *Radiation Detection and Measurement, 3rd ed.* John Wiley & Sons Inc, New York, NY, 1999.

[40] P. Shikhaliev. Tilted angle CZT detector for photon counting/energy weighting x-ray and CT imaging. *Physics in Medicine and Biology*, 51:4267–4287, August 2006.

[41] S. Agostinelli et al. GEANT4: A simulation toolkit. *Nuclear Instruments and Methods in Physics Research*, A506:250–303, 2003.

[42] X-5 Monte Carlo Team. *MCNP A General Monte Carlo N-Particle Transport Code, Version 5*, volume 1 Overview and Theory. Los Alamos National Laboratory, October 2005.

[43] S. Chelikani, J. Gore, and G. Zubal. Optimizing Compton camera geometries. *Physics in Medicine and Biology*, 49:1387–1408, 2004.

[44] B.M. Smith, K.L. Matthews, A.W. Lackie, W.H. Hill, W.-H. Wang, and M.L. Cherry. An electronically-collimated portable gamma-ray detector for locating environmental radiation sources. In *Proceedings of SPIE*, volume 6319 of *X-Ray and Gamma-Ray Detector Physics and Penetrating Radiation Systems VIII; article 63190H; doi: 10.1117/12.683568*, 2006.

[45] B.M. Smith, K.L. Matthews, W.H. Hill, A.W. Lackie, W.H. Wang, and M.L. Cherry. An electronically-collimated gamma-ray detector for intraoperative localization of radiation sources. *Medical Physics*, 33(6):2277, 2006.

[46] D. Lowe, A. Truman, H. Kwok, and A. Bergman. Results of optical Monte Carlo simulations of a compact γ camera for the detection of sentinel lymph nodes. *Nuclear Instruments and Methods in Physics Research*, A466:551–568, 2001.

[47] A. Zumbiehl and M. Hage-Alia. Modelling and 3D optimisation of CdTe pixels detector arraygeometry – extension to small pixels. *Nuclear Instruments and Methods in Physics Research*, A469:227–339, 2001.

[48] F. Mathy, A. Gliere, E. d'Aillon, P. Masse, M. Picone, J. Tabary, and L. Verger. A three-dimensional model of CdZnTe gamma-ray detector and its experimental validation. *IEEE Transactions on Nuclear Science*, 51(5):2419–2426, 2004.

[49] P. Guerra, G. Kontaxakis, D. Visvikis, D. Darambara, and A. Santos. Detailed modelling of pixellated CdZnTe detectors for an accurate performance characterization of a multi-modality imaging system. In *Conference Record of the 2006 IEEE Nuclear Science Symposium and Medical Imaging Conference*, volume 3, pages 1924–1928, San Diego, CA, 2006.

[50] L. Kelly. Performance evaluation of two CZT gamma ray imaging systems. Master's thesis, Louisiana State University and Agricultural & Mechanical College, Baton Rouge, LA, 2005.

[51] M. Wojdyr, S. Gierlotka, J. Folmer, and Michael Richardson. *Fityk 0.8.2 - User's Manual*. Unipress, Institute of High Pressure Physics, ul. Sokolowska 29/37 01-142, Warsaw, POLAND, August 2007.

APPENDIX A

GRAPHS

This appendix shows histograms and averages of all of the core data sets. The first histogram is of differences between the Compton computed angle and the angle computed by source and pixel location. The second histogram is an image of detector response. For each given true angle, the Compton angle was binned. An image was made of the zero to ninety degree corner of the histogram. The mean and mode angles were computed from the detector and the observer viewpoints and are graphed in the two graphs shown. The error bars around the mean averages represent one standard deviation. Graphs are printed with consistent ranges to facilitate comparison of correct information and some appear blank. Data sets where results were expected have been underlined.

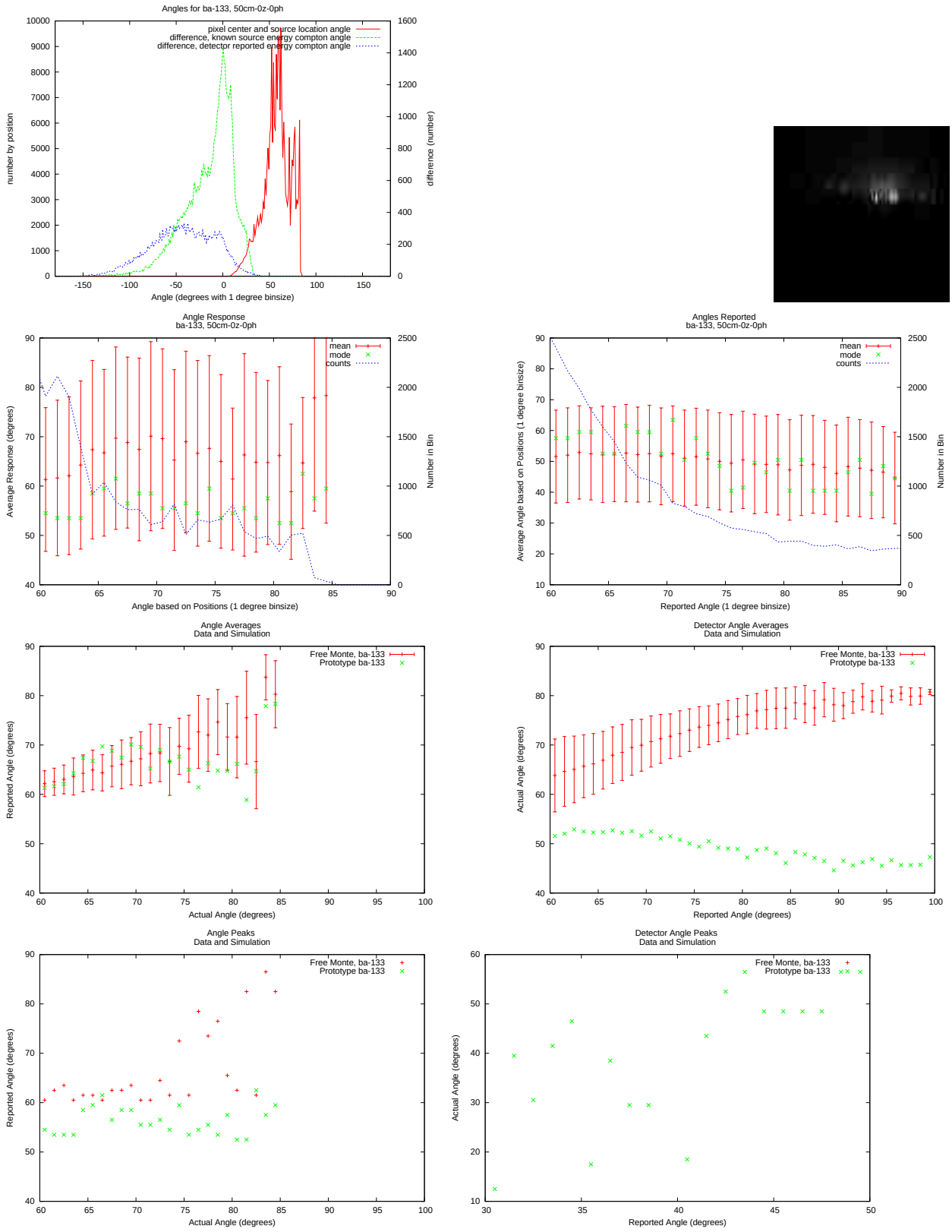

Figure A.1. Ba-133 50cm, 0ϕ, $0z$.

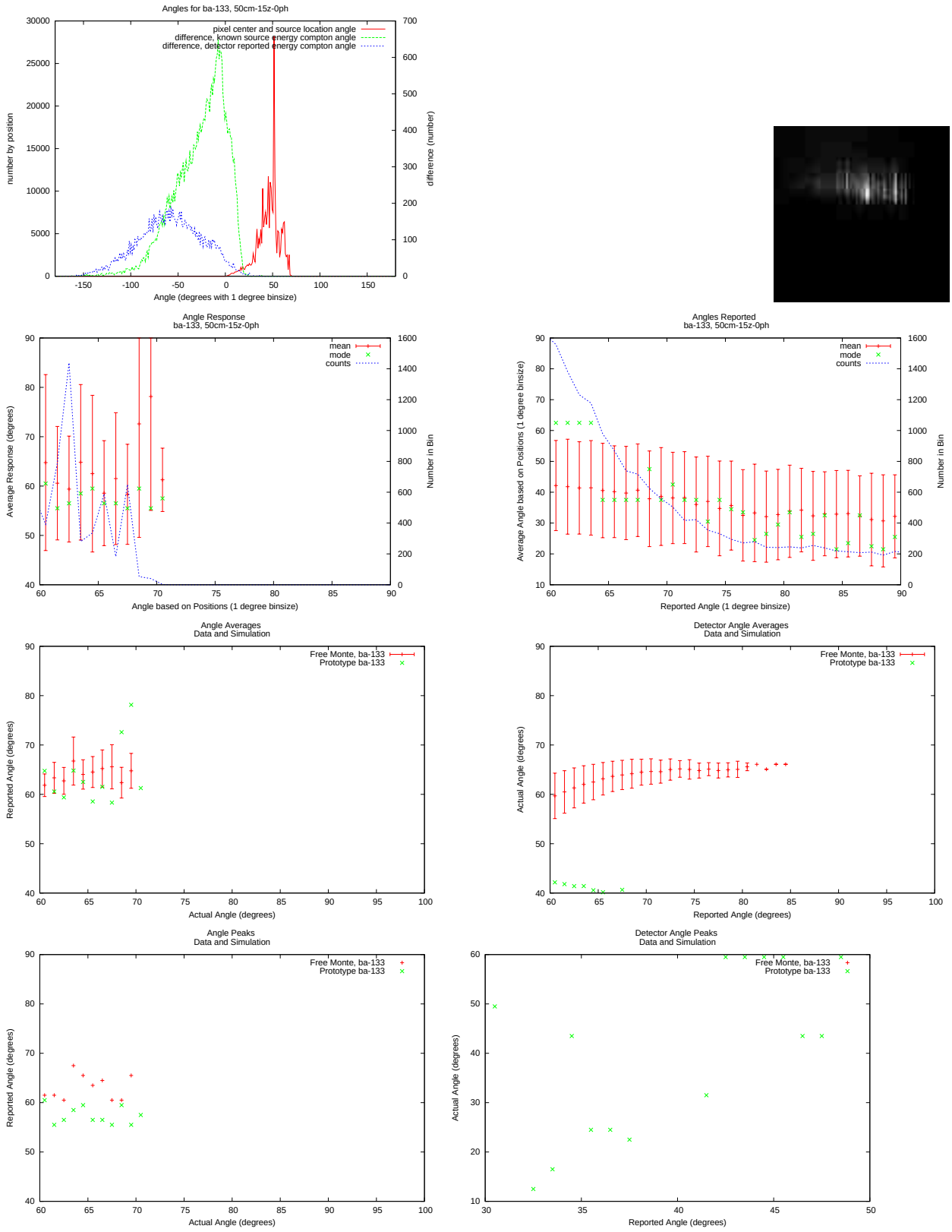

Figure A.2. Ba-133 50cm, 0ϕ, 15z.

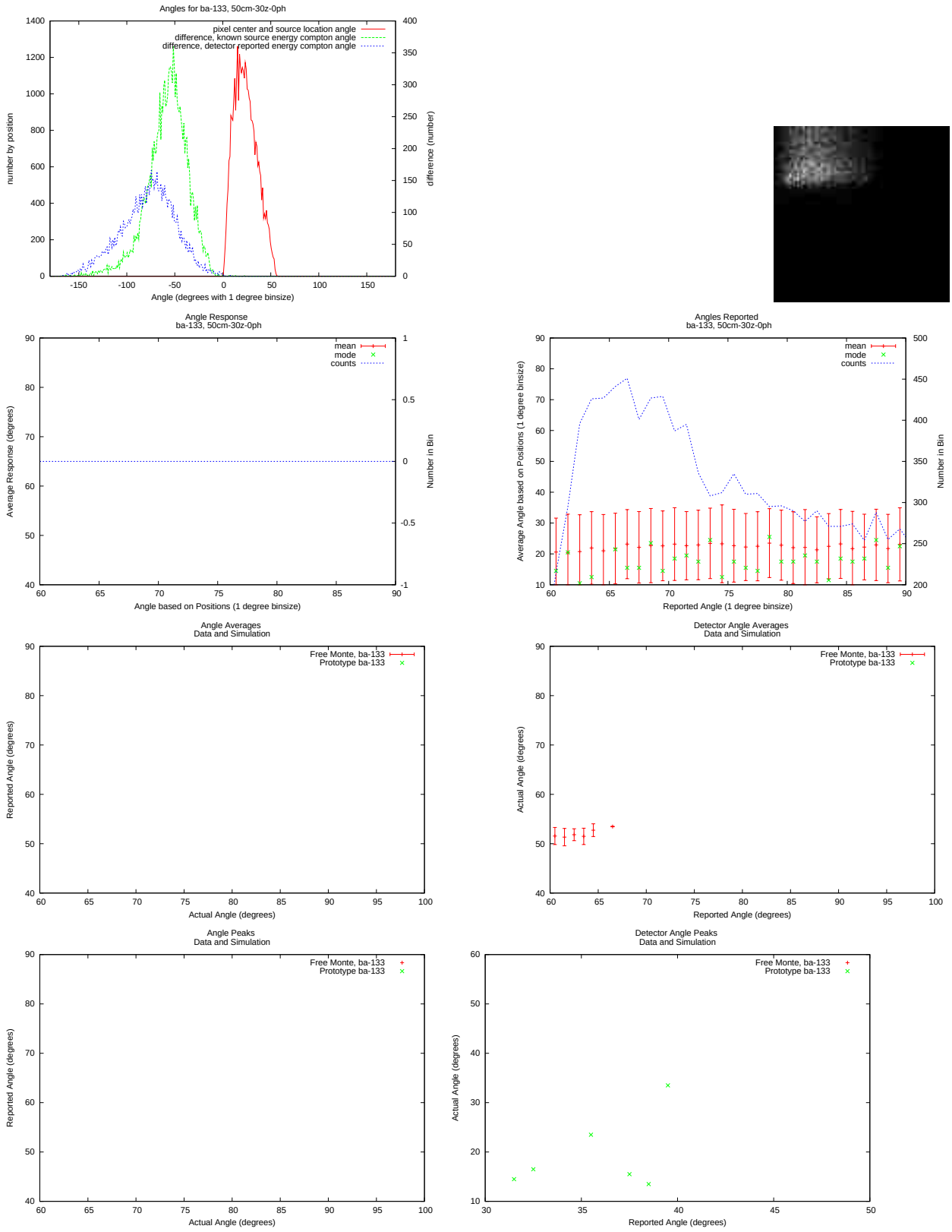

Figure A.3. Ba-133 50cm, 0ϕ, $30z$.

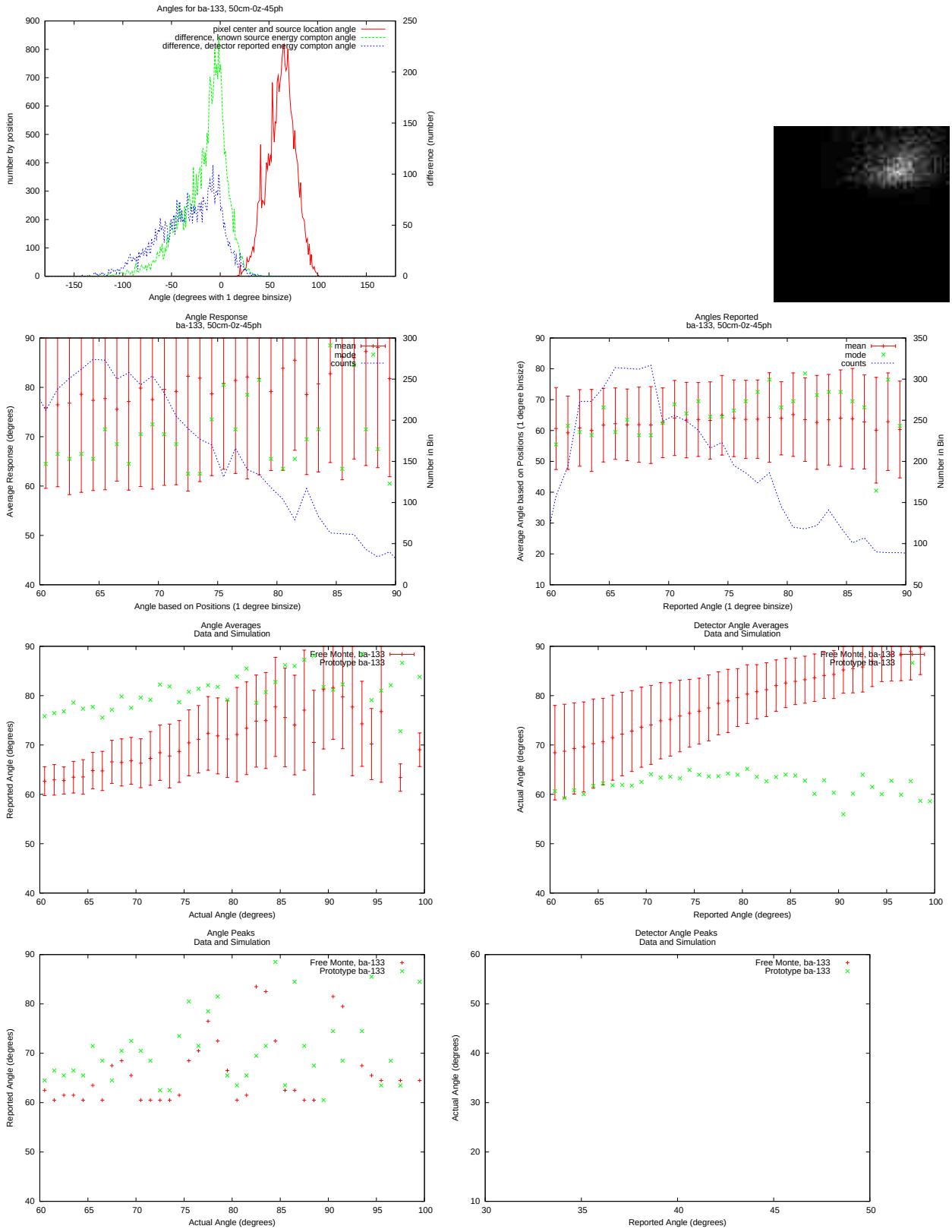

Figure A.4. Ba-133 50cm, 45ϕ, $0z$.

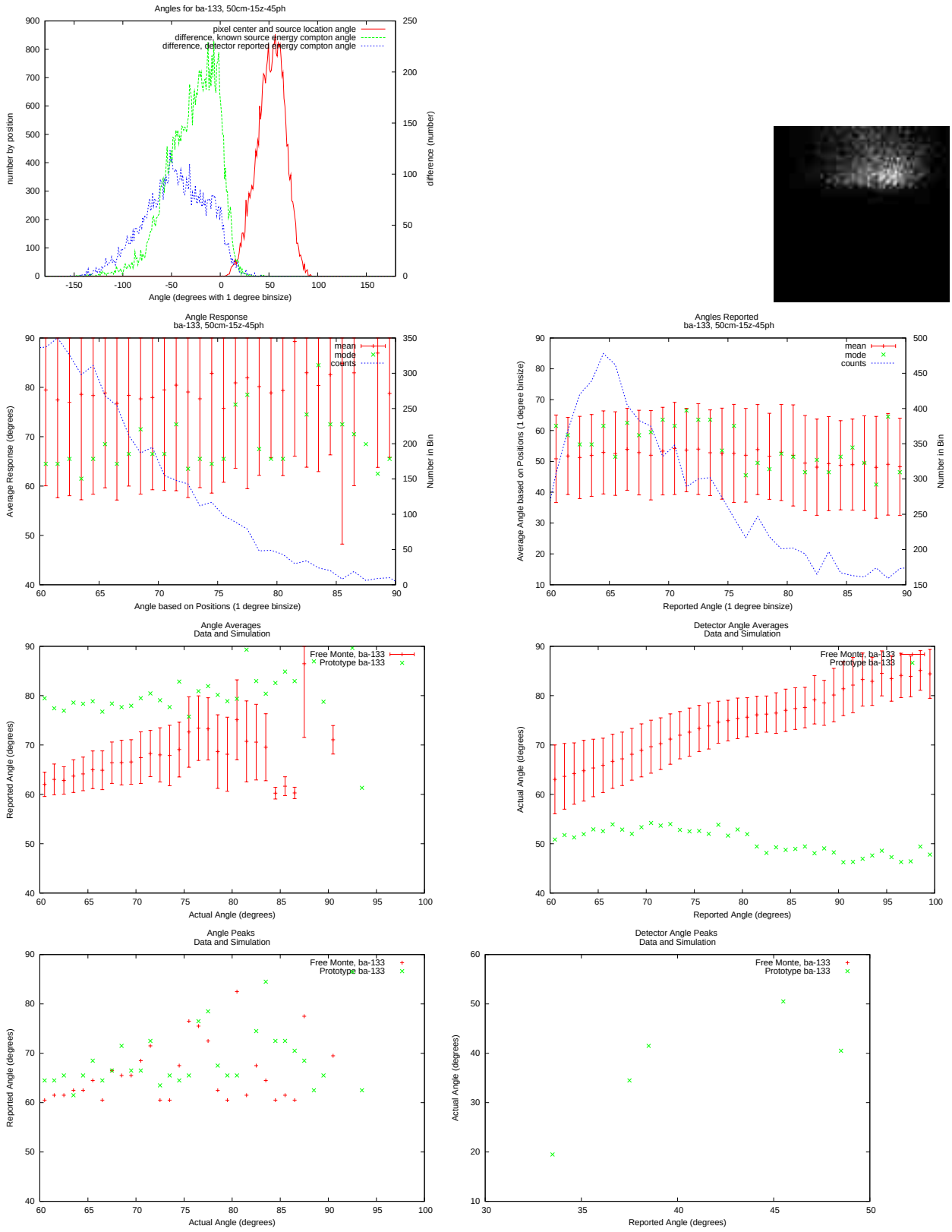

Figure A.5. Ba-133 50cm, 45ϕ, 15z.

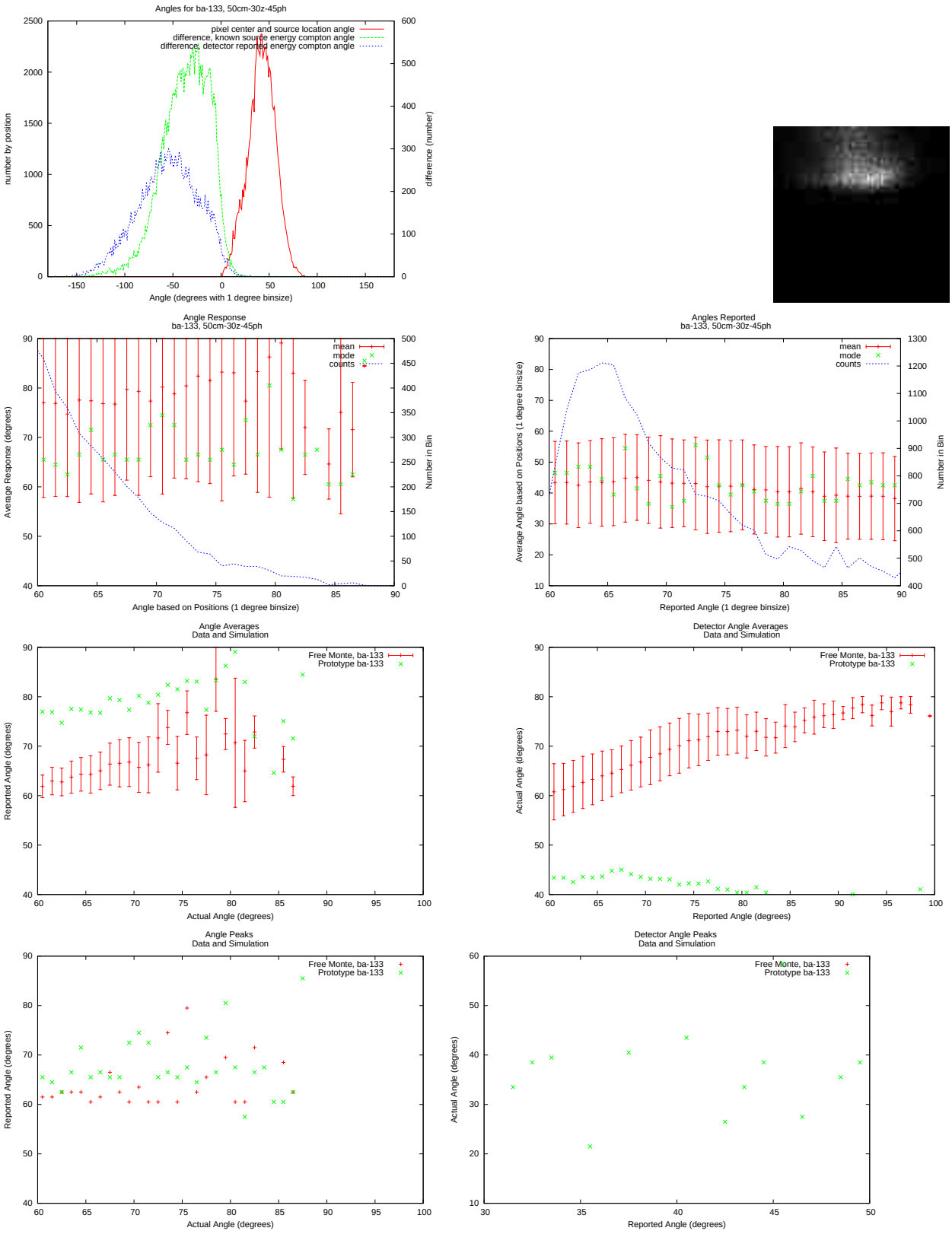

Figure A.6. Ba-133 50cm, 45ϕ, 30z.

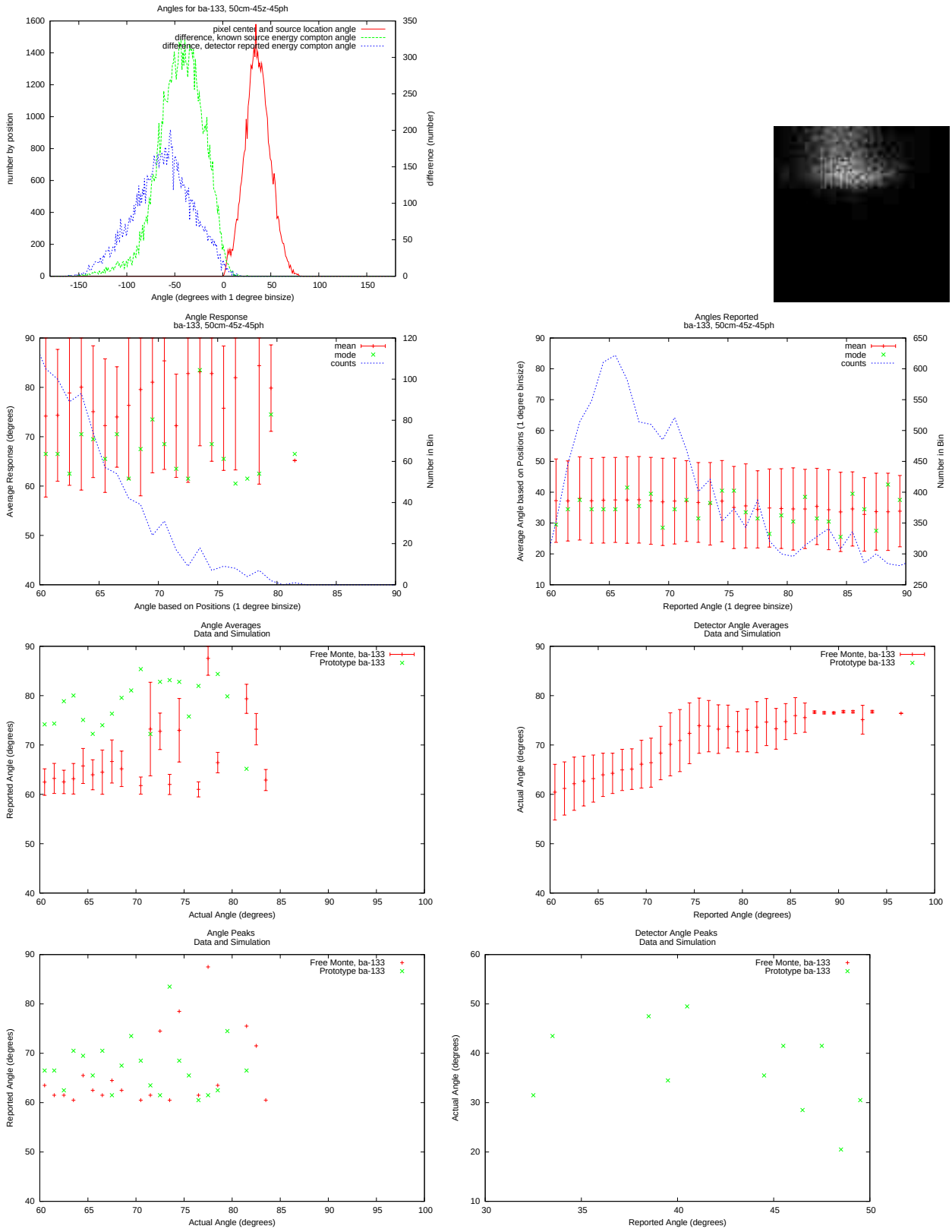

Figure A.7. Ba-133 50cm, 45ϕ, 45z.

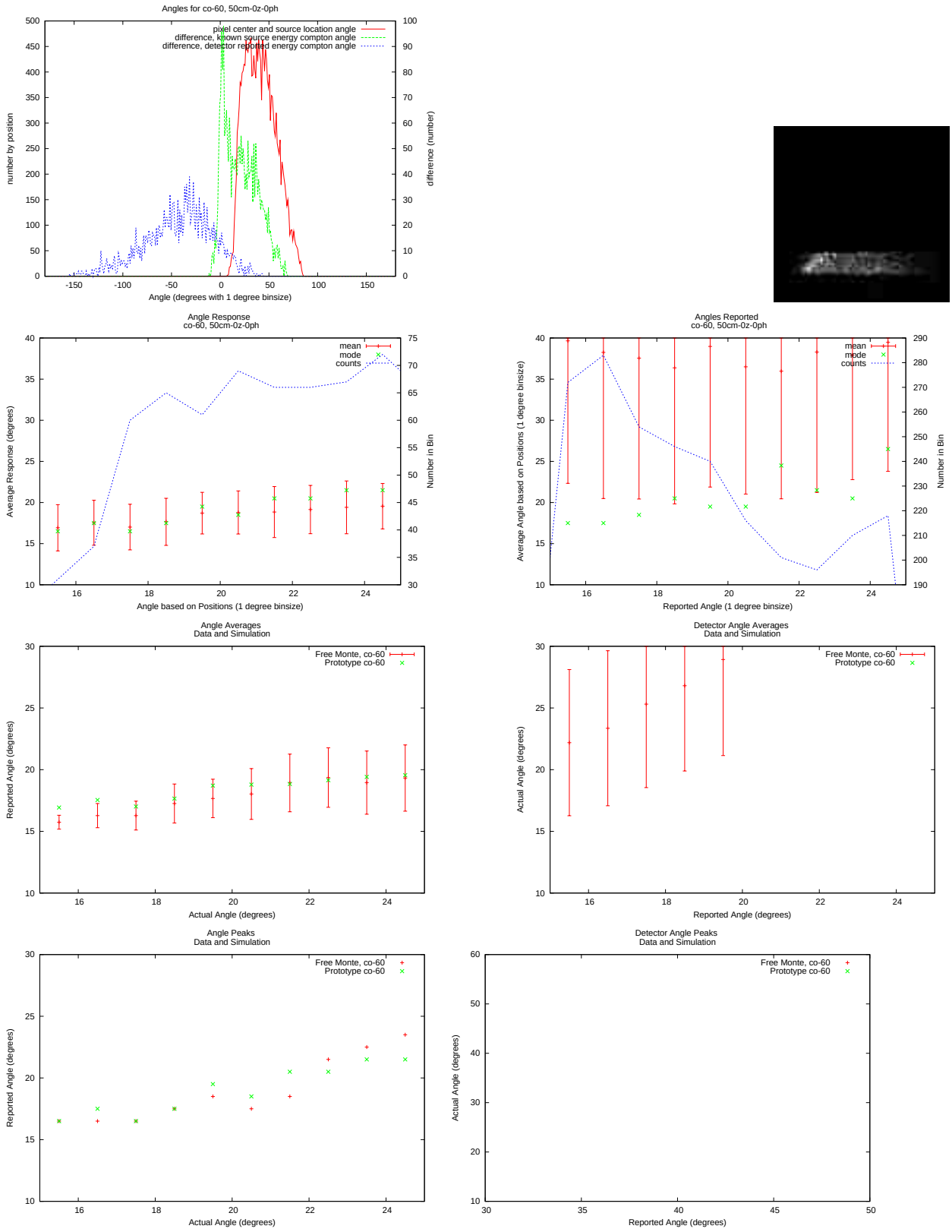

Figure A.8. Co-60 50cm, 0ϕ, $0z$.

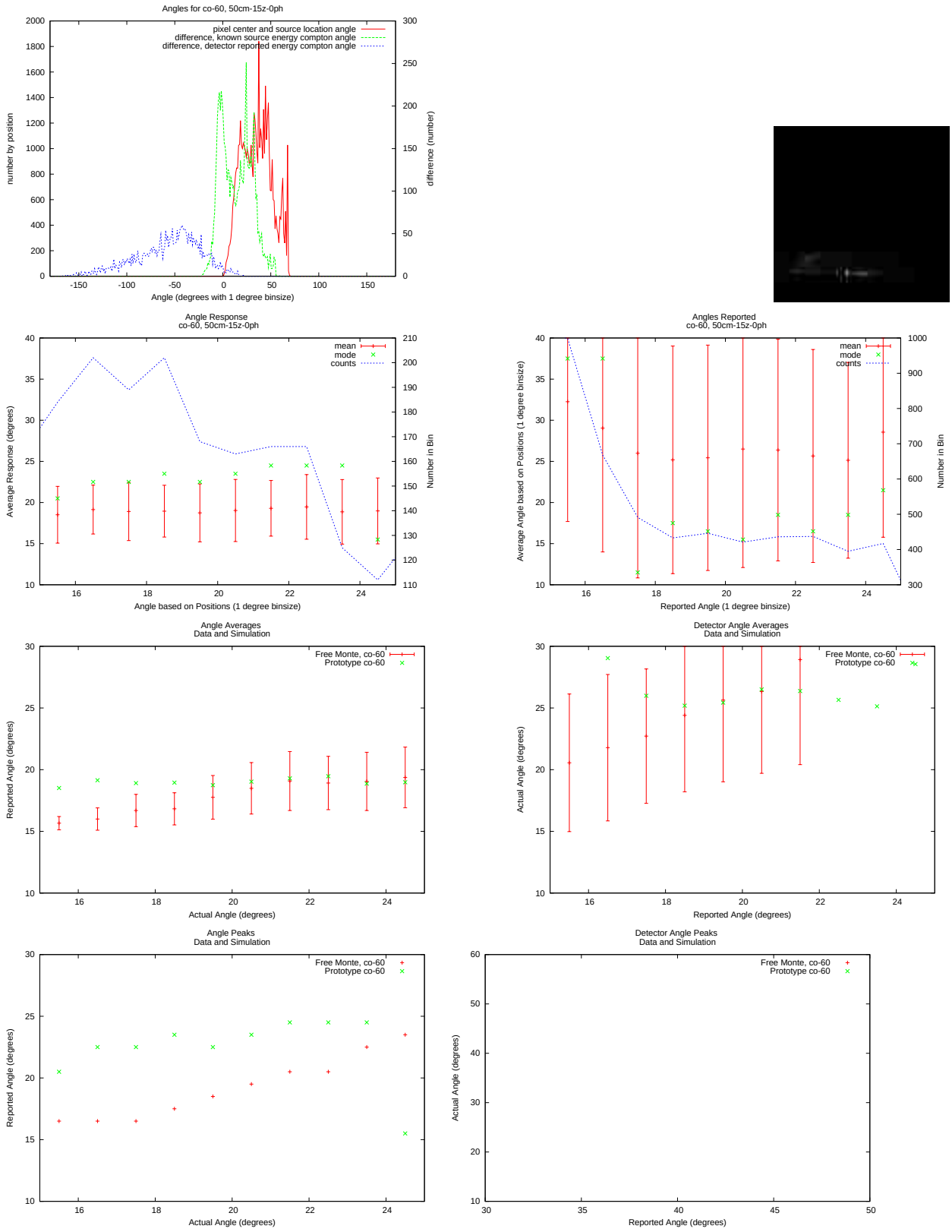

Figure A.9. Co-60 50cm, 0ϕ, $15z$.

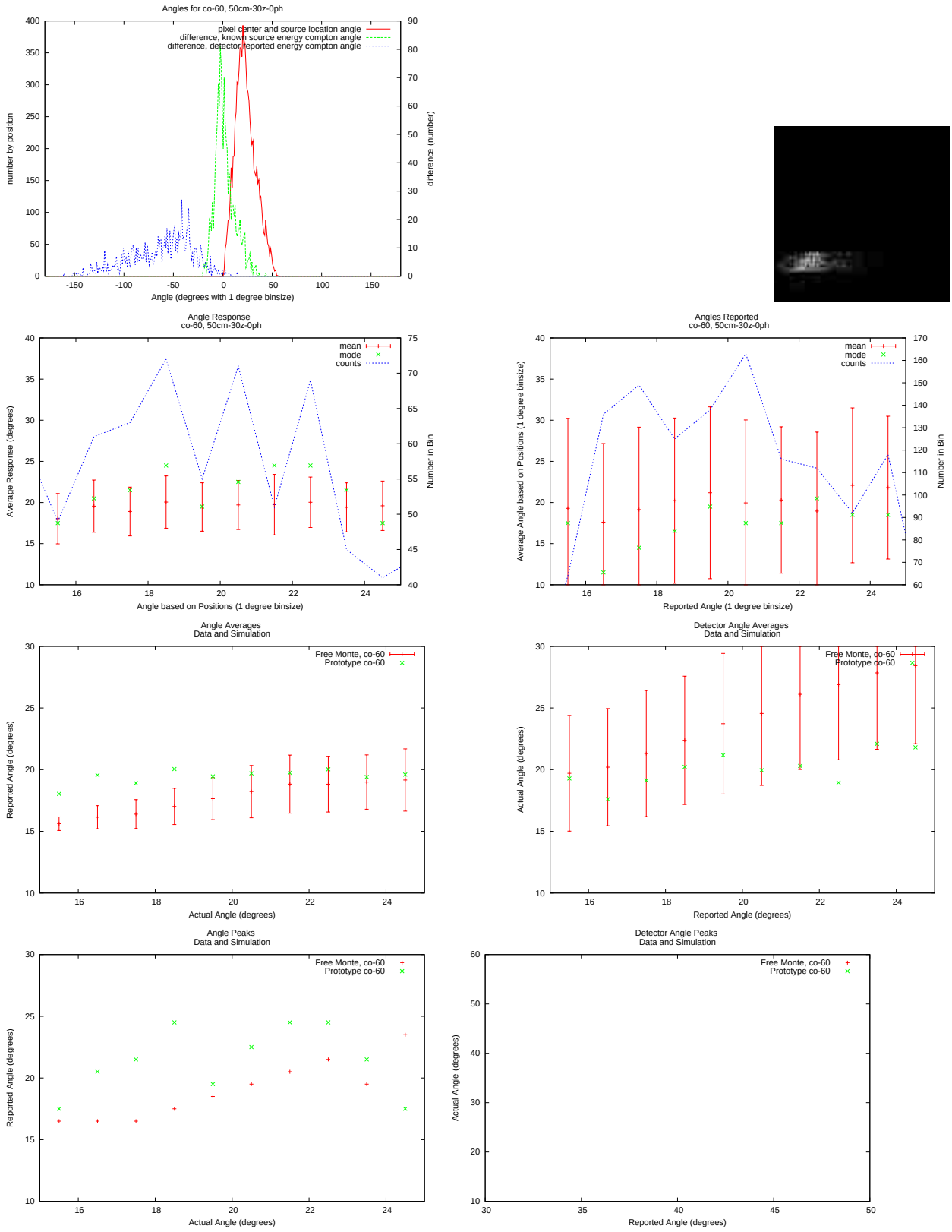

Figure A.10. Co-60 50cm, 0ϕ, $30z$.

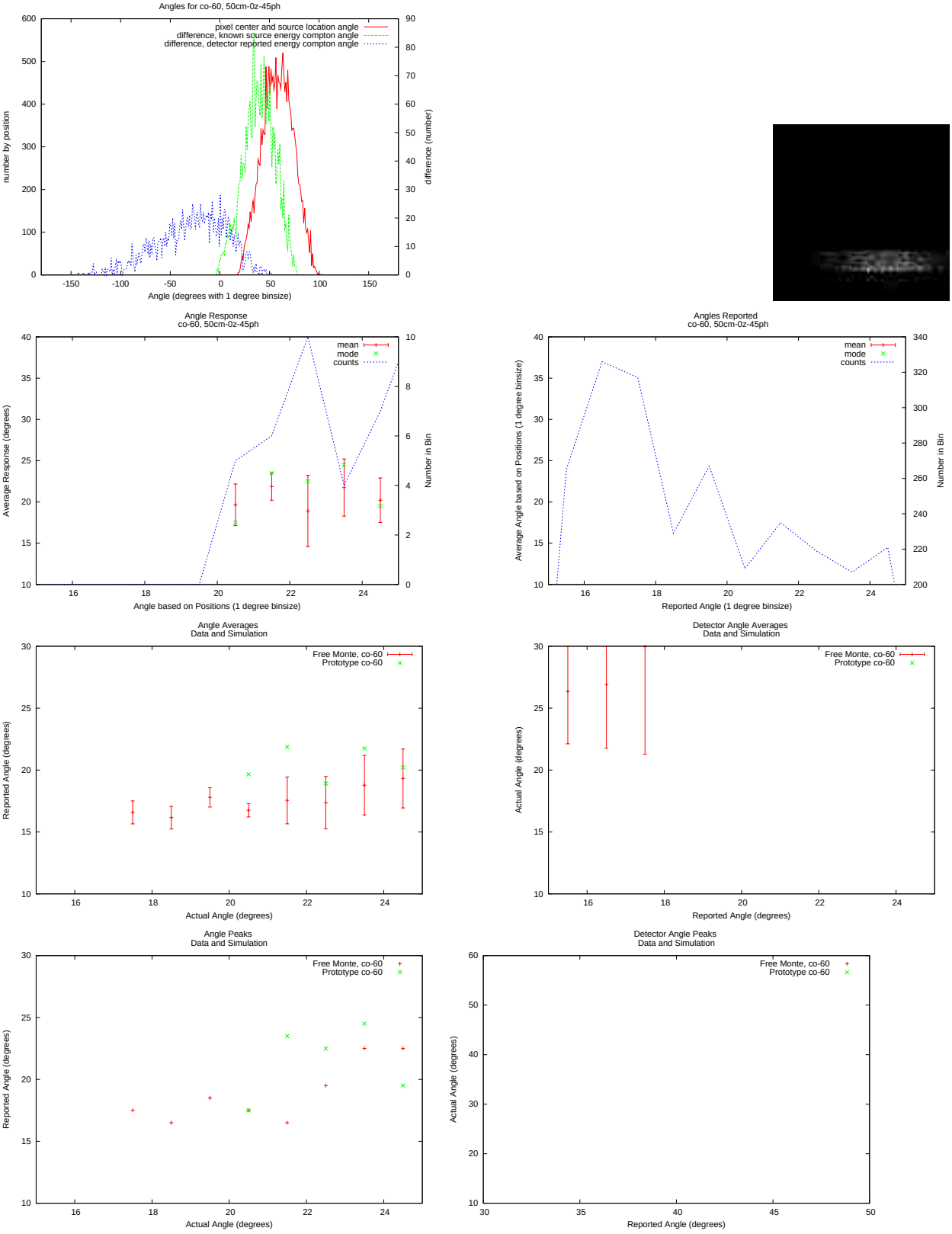

Figure A.11. Co-60 50cm, 45ϕ, 0z.

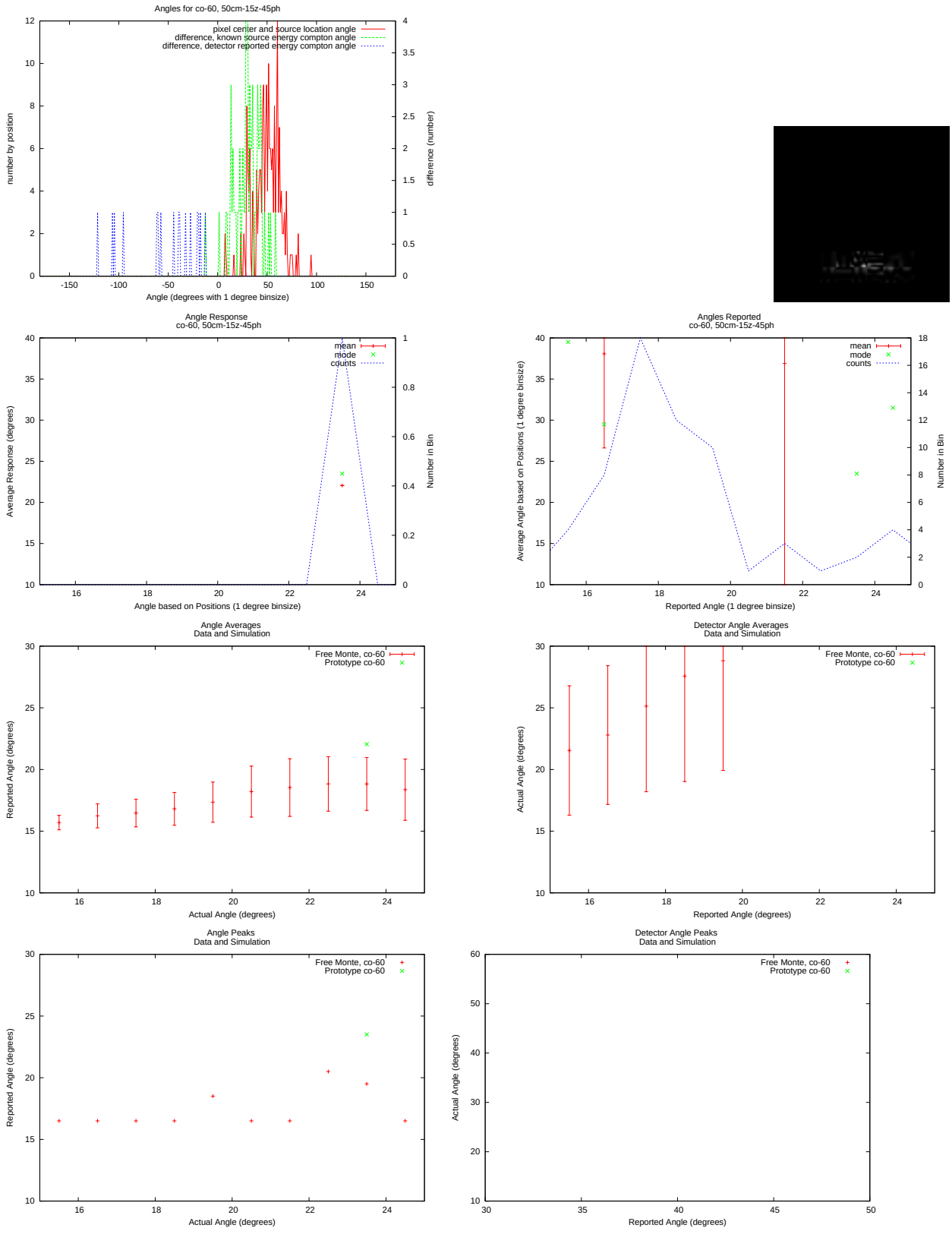

Figure A.12. Co-60 50cm, 45ϕ, 15z.

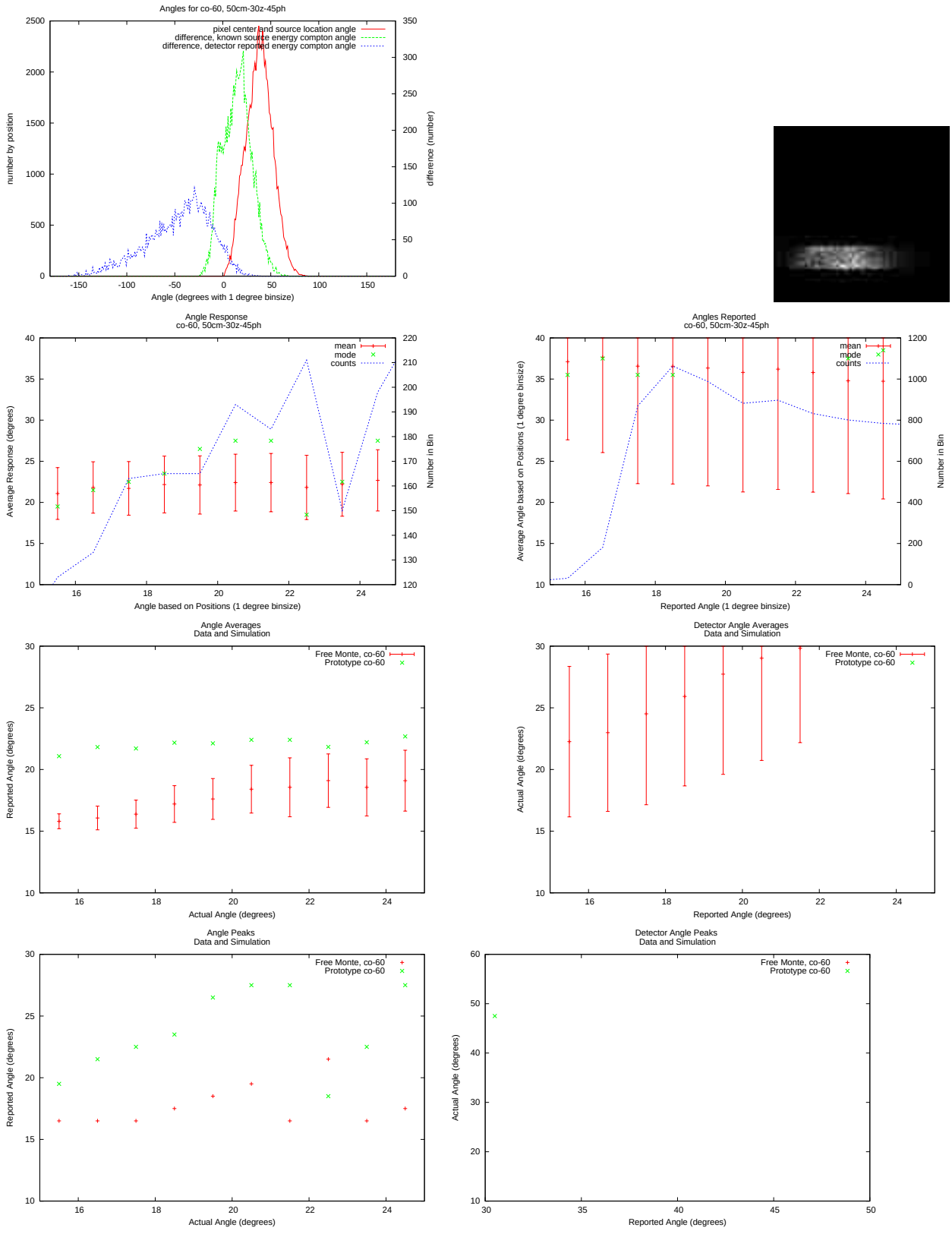

Figure A.13. Co-60 50cm, 45ϕ, 30z.

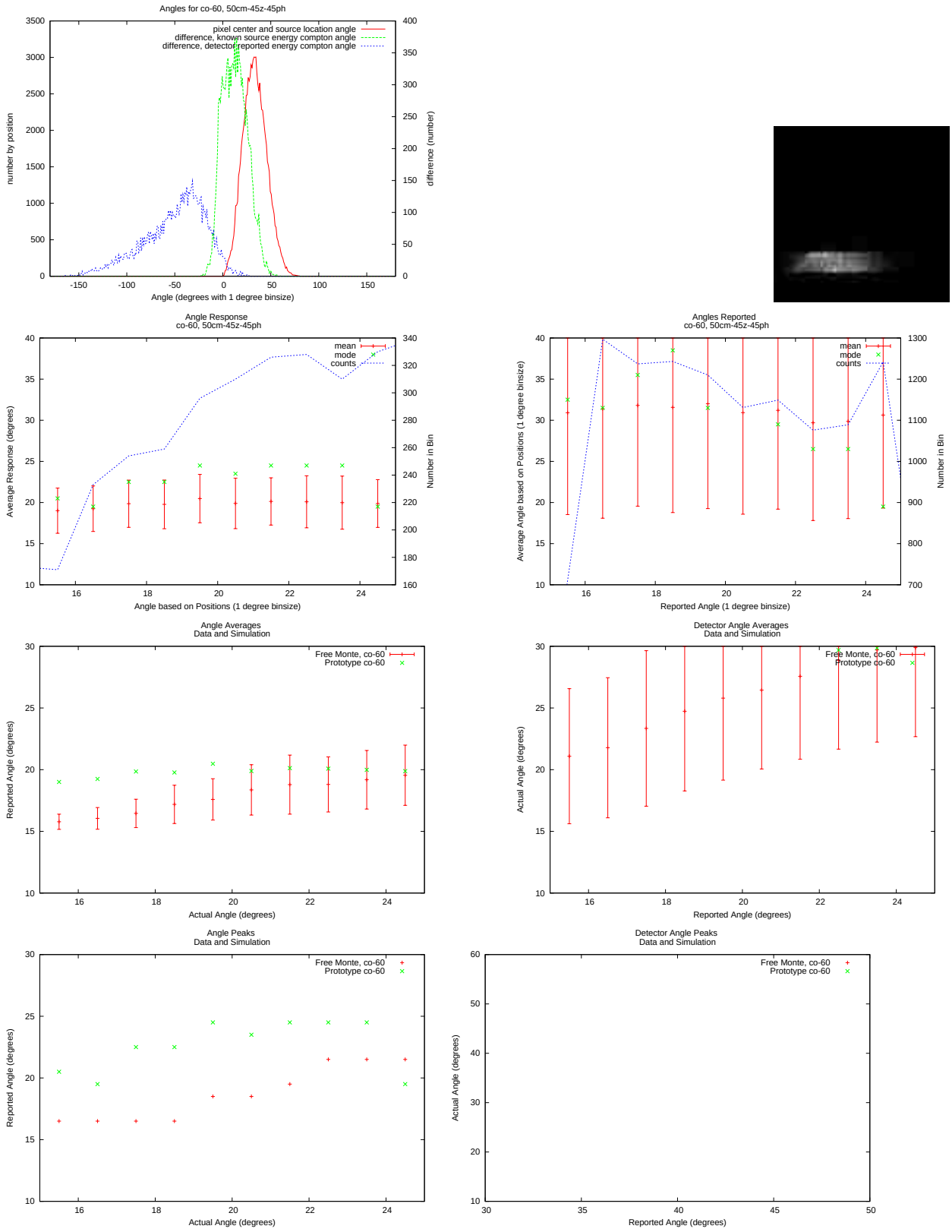

Figure A.14. Co-60 50cm, 45ϕ, 45z.

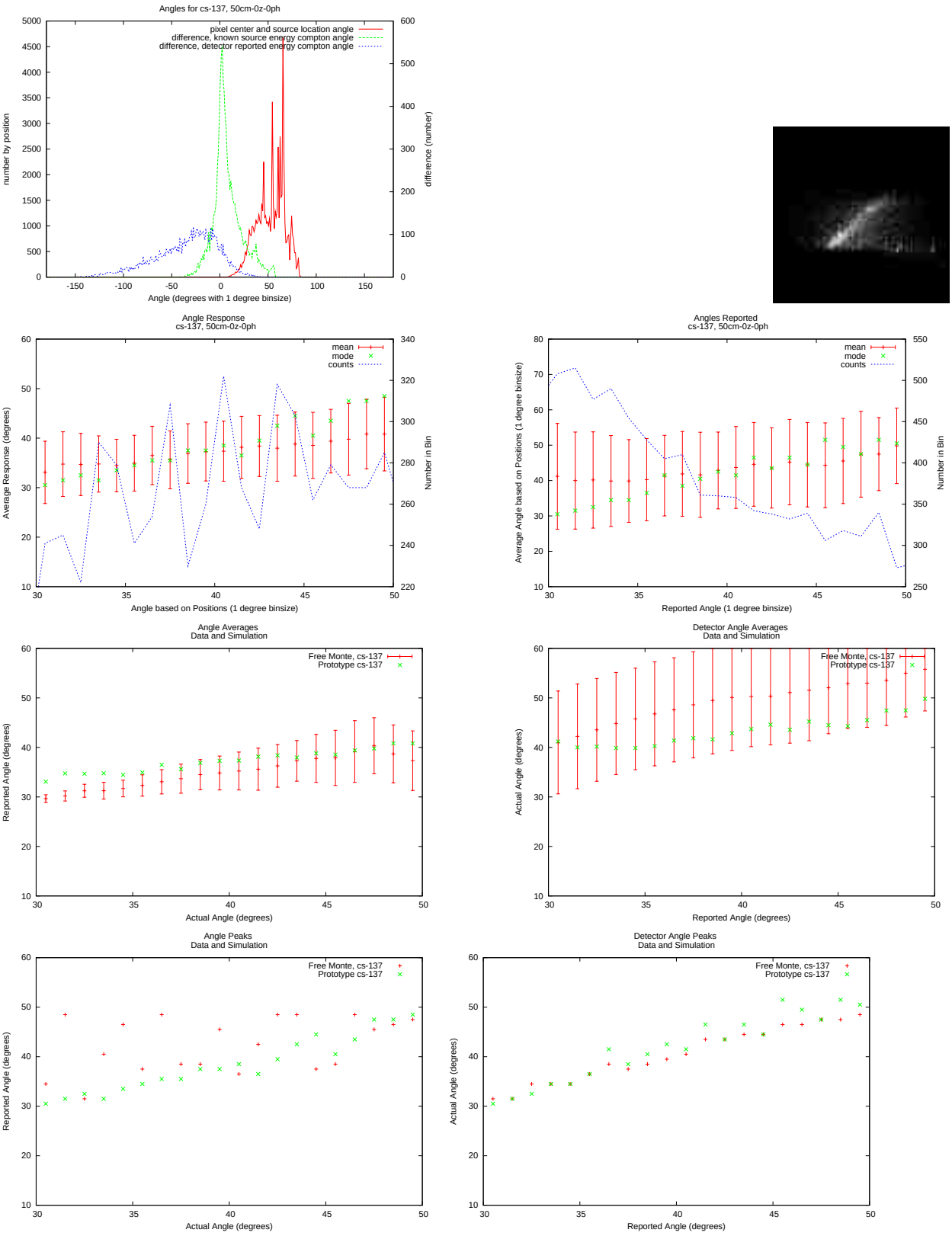

Figure A.15. Cs-137 50cm, 0ϕ, $0z$.

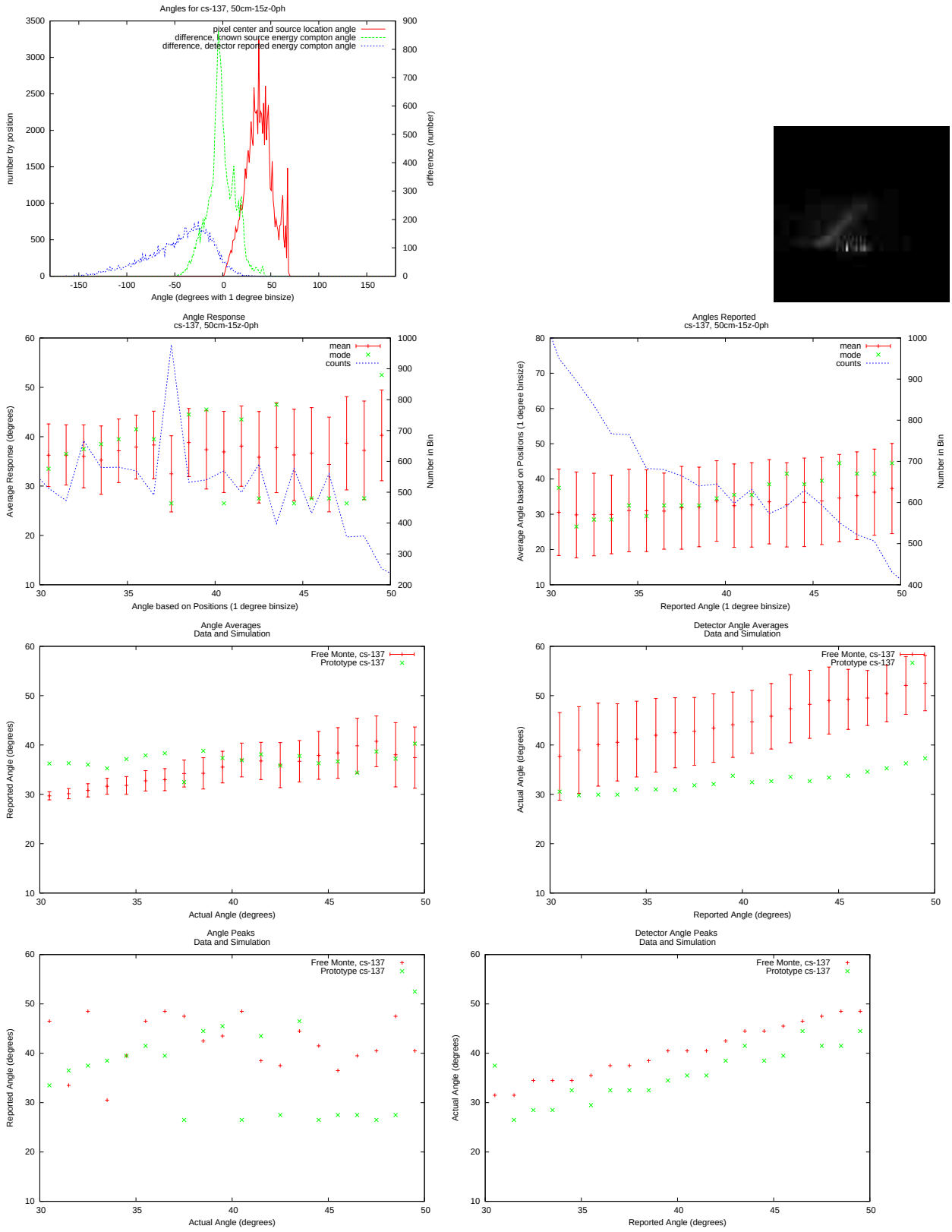

Figure A.16. Cs-137 50cm, 0ϕ, $15z$.

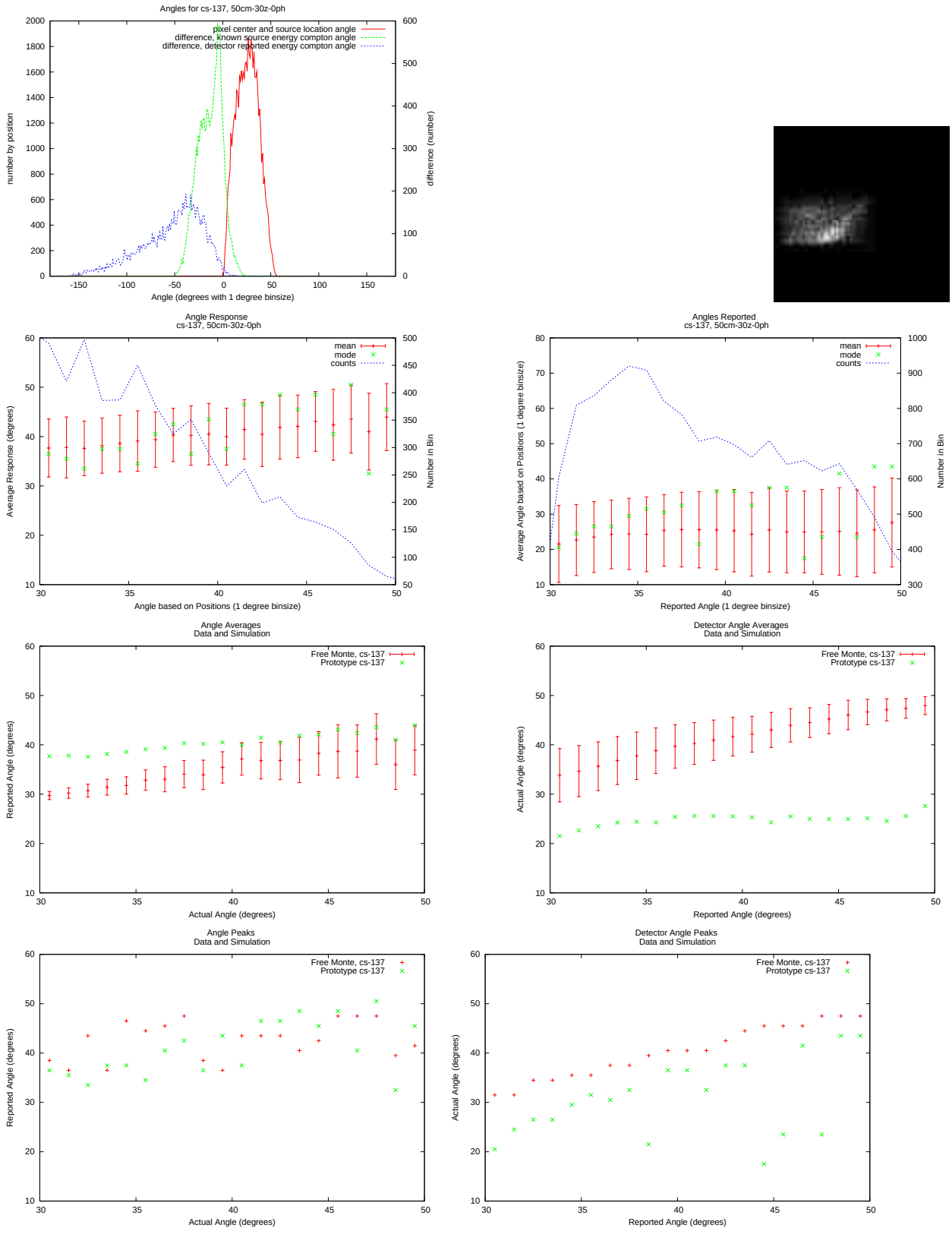

Figure A.17. Cs-137 50cm, 0ϕ, $30z$.

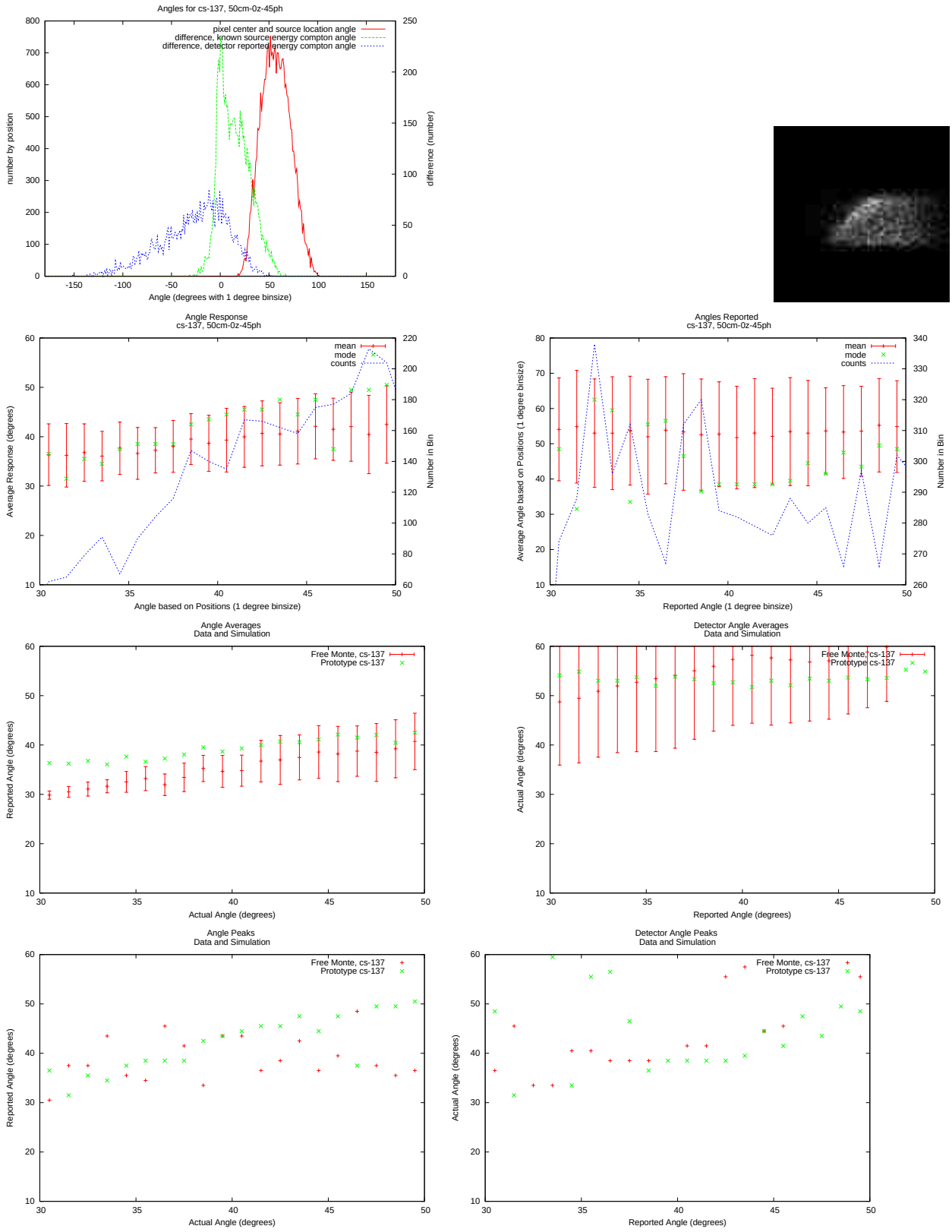

Figure A.18. Cs-137 50cm, 45ϕ, 0z.

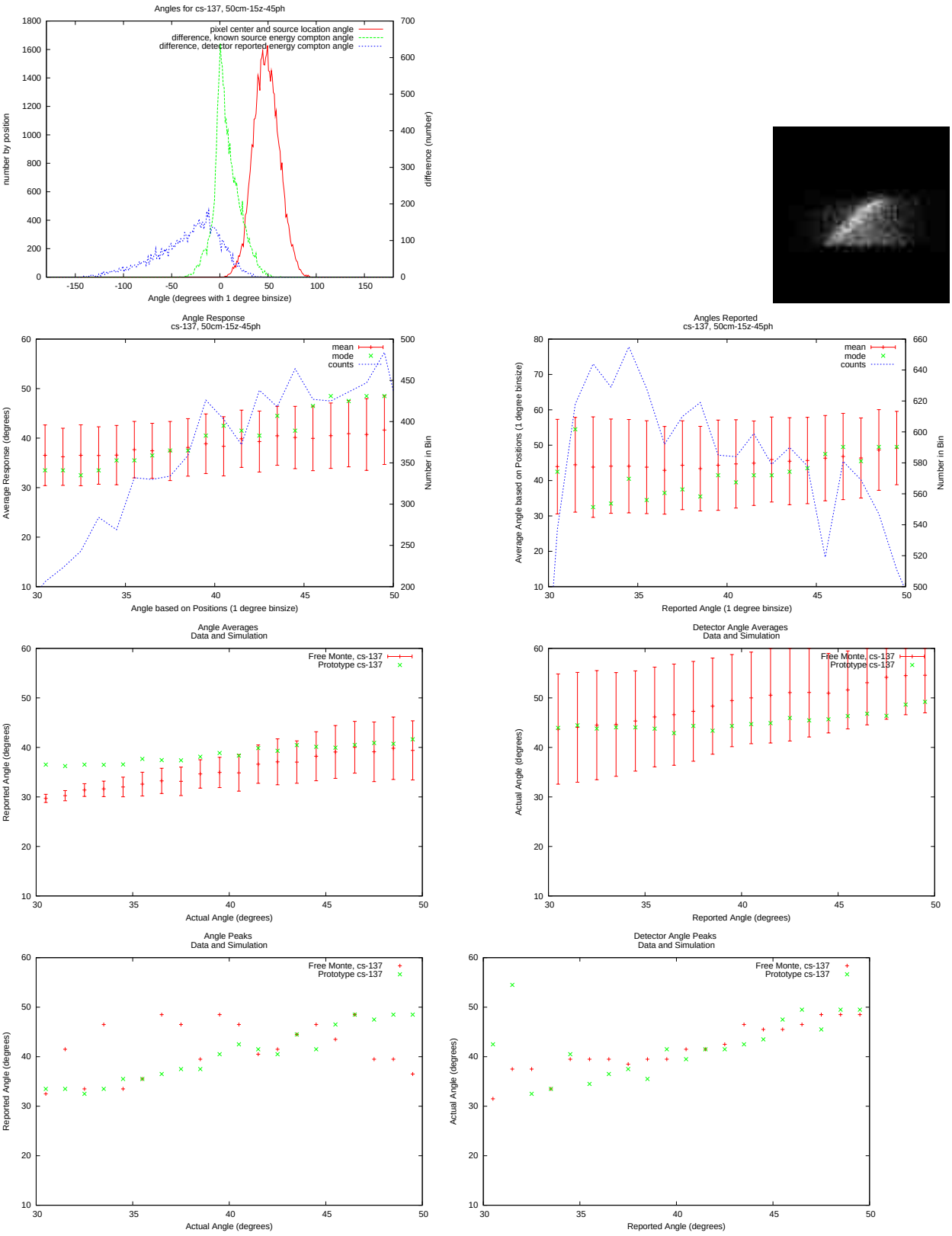

Figure A.19. Cs-137 50cm, 45ϕ, 15z.

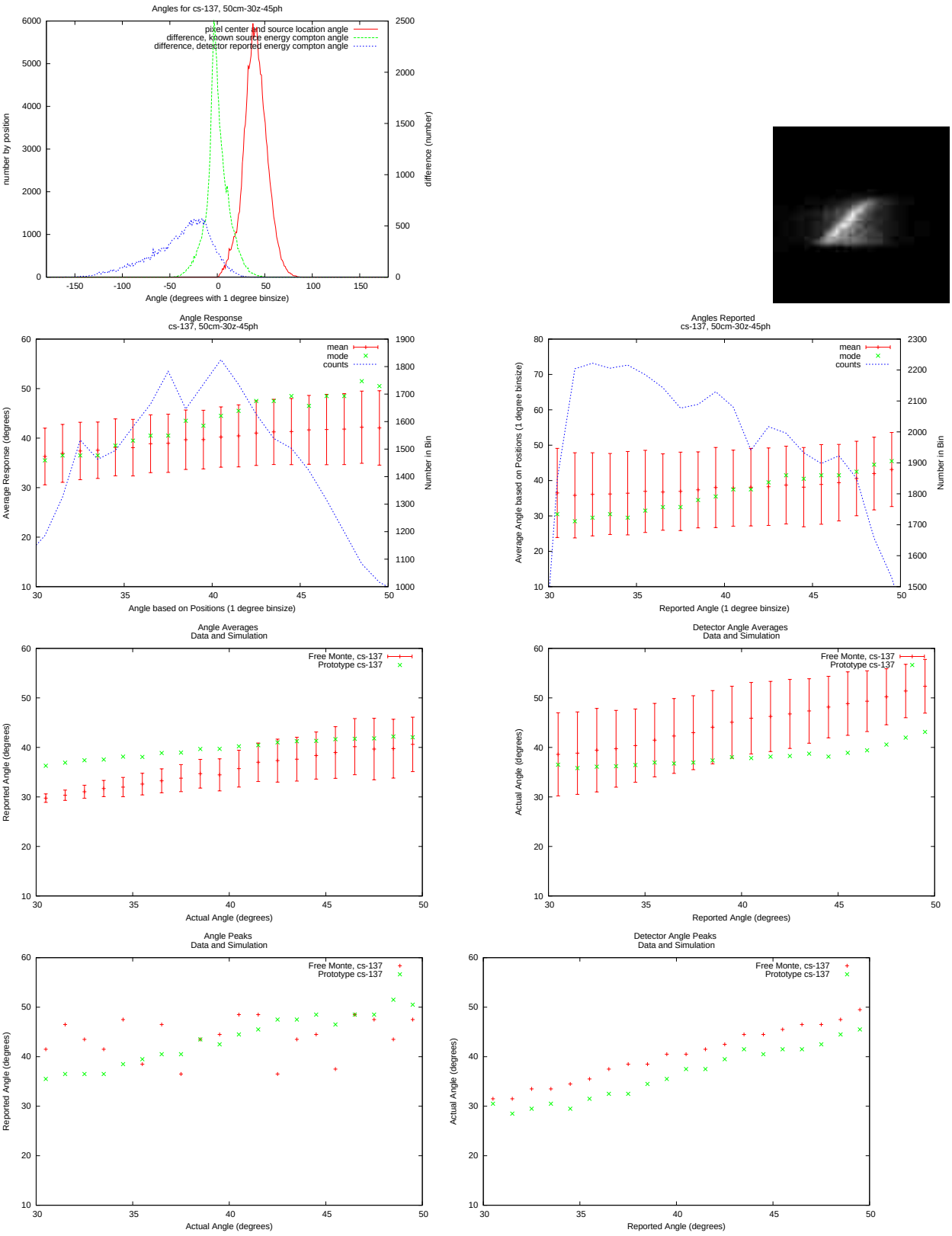

Figure A.20. Cs-137 50cm, 45ϕ, 30z.

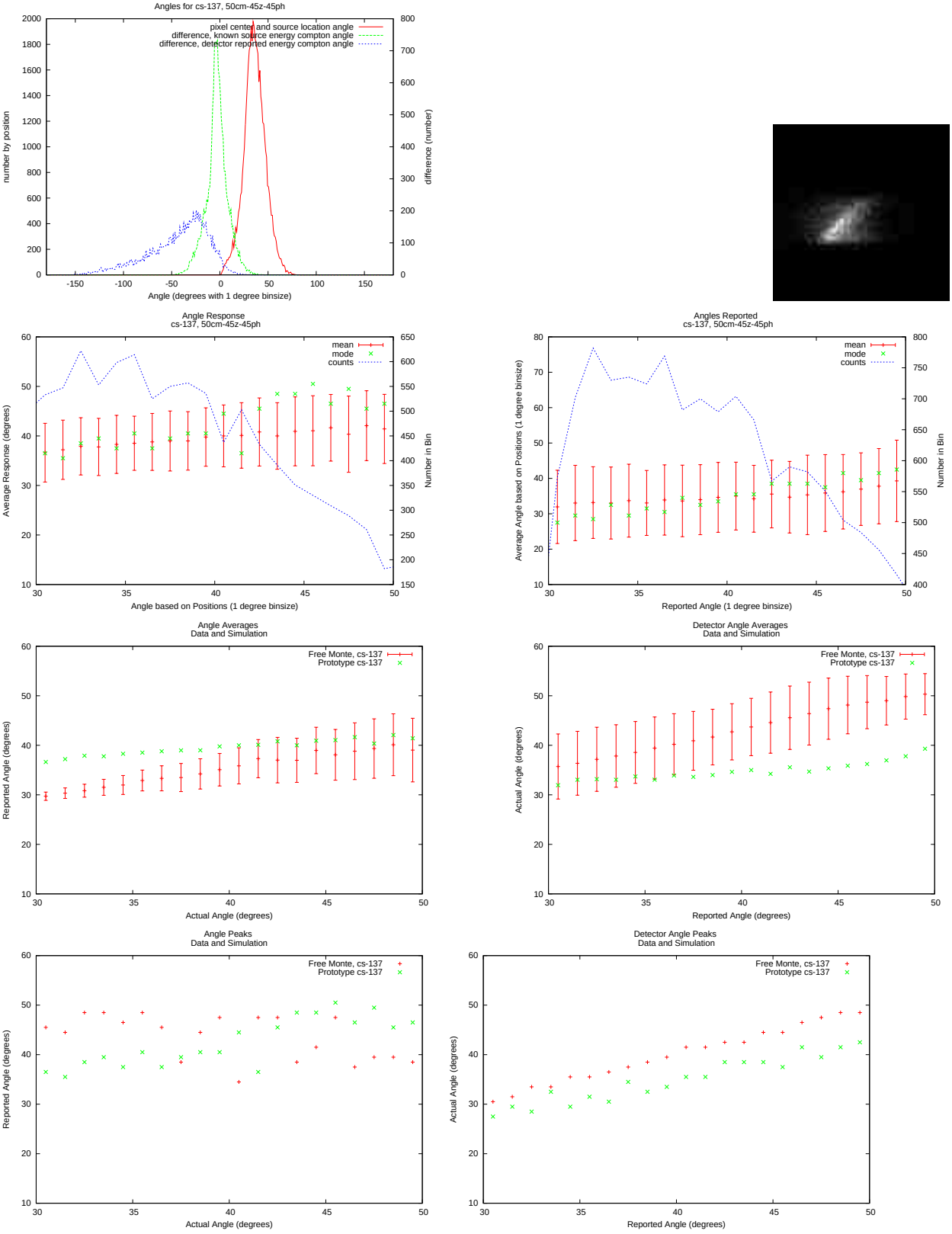

Figure A.21. Cs-137 50cm, 45ϕ, 45z.

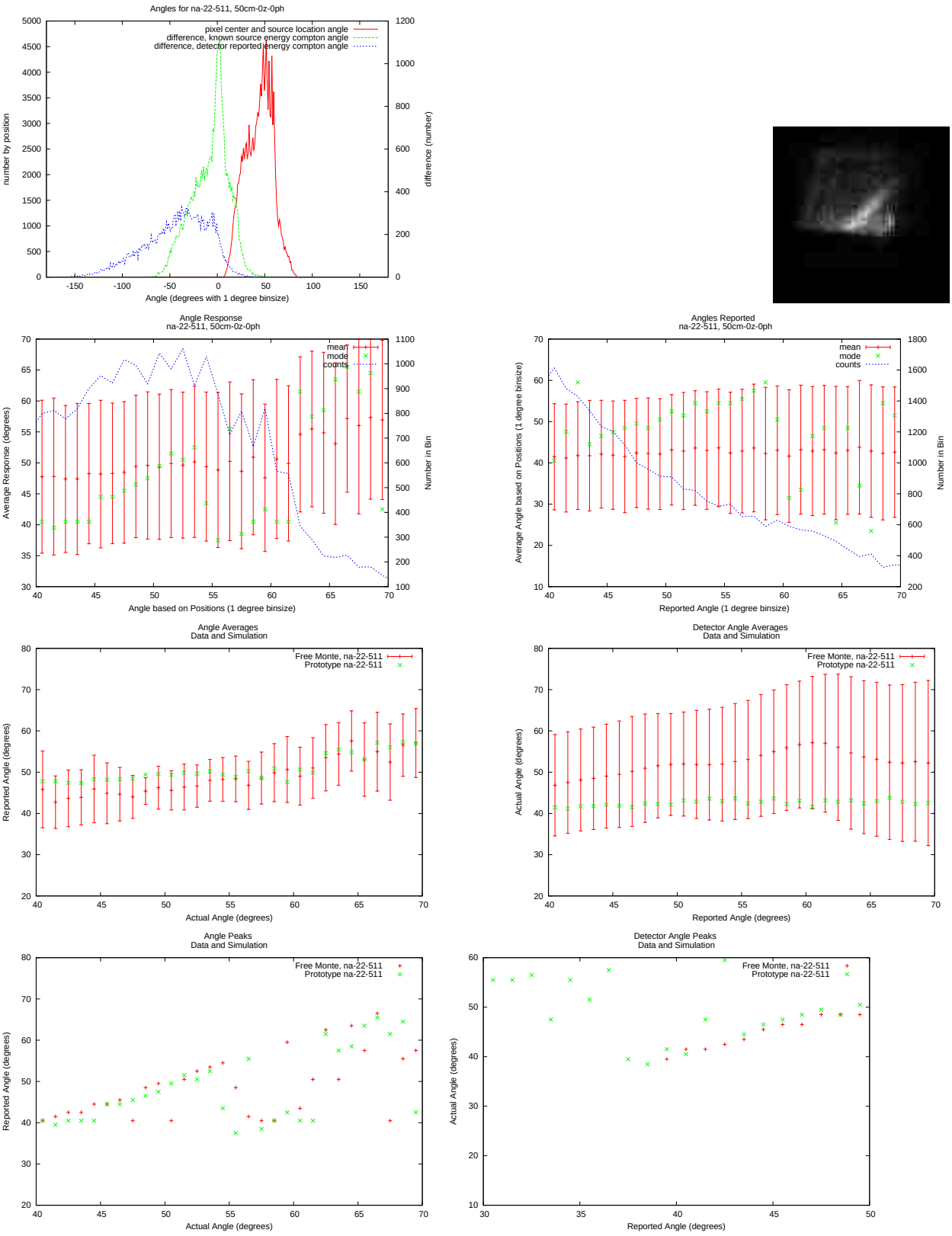

Figure A.22. Na-22, 511 keV 50cm, 0ϕ, $0z$.

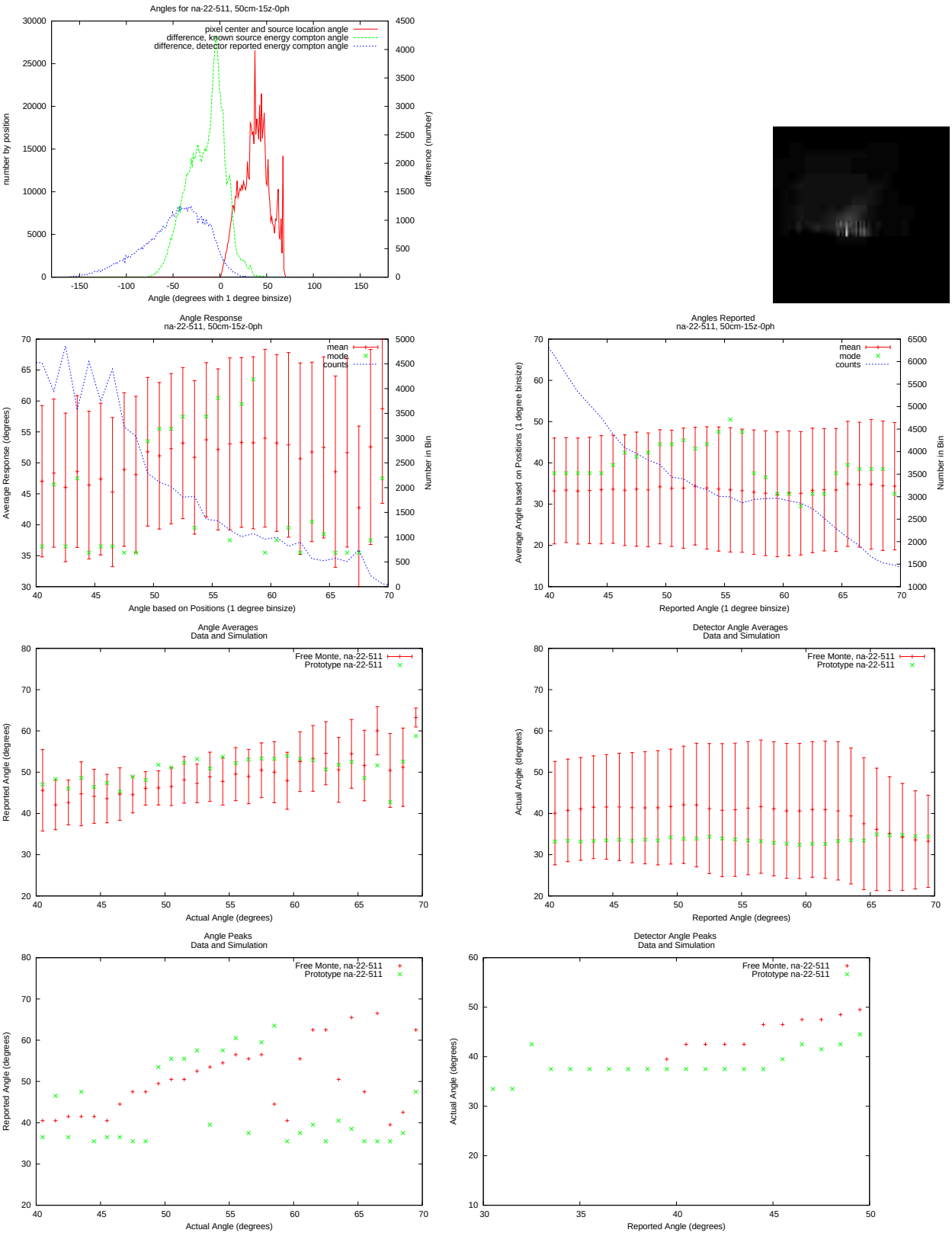

Figure A.23. Na-22, 511 keV 50cm, 0ϕ, $15z$.

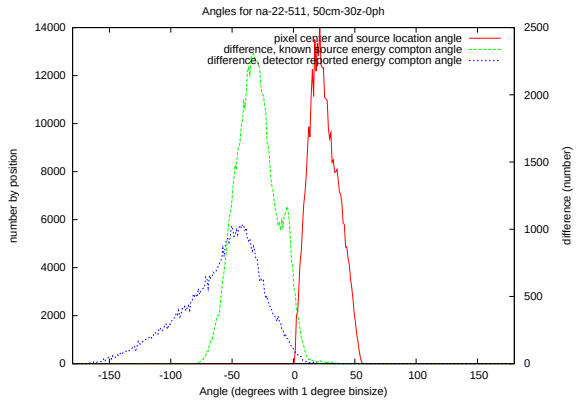

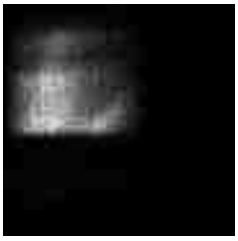

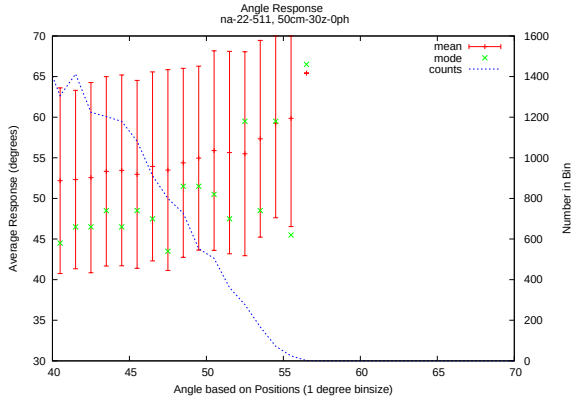

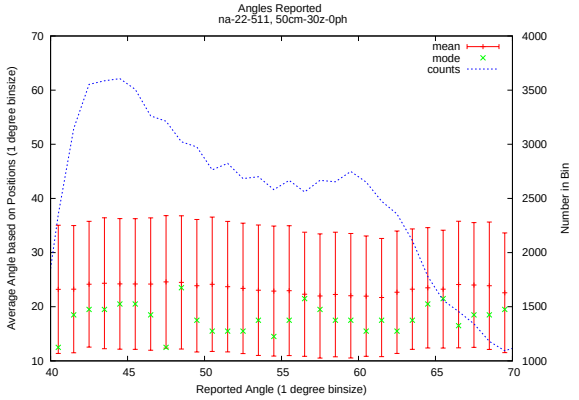

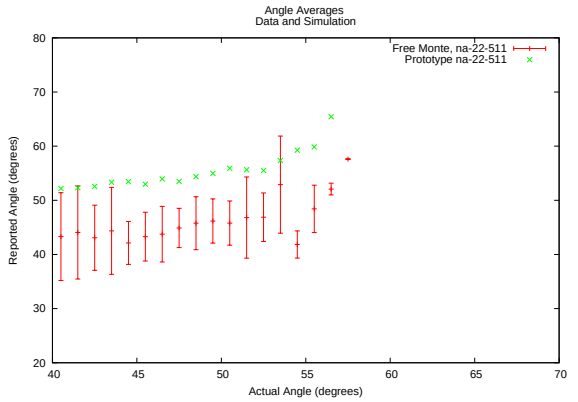

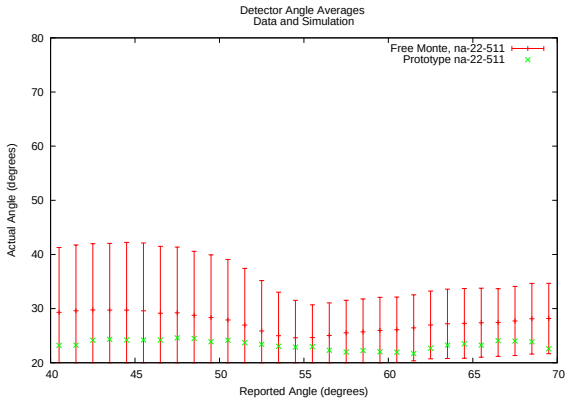

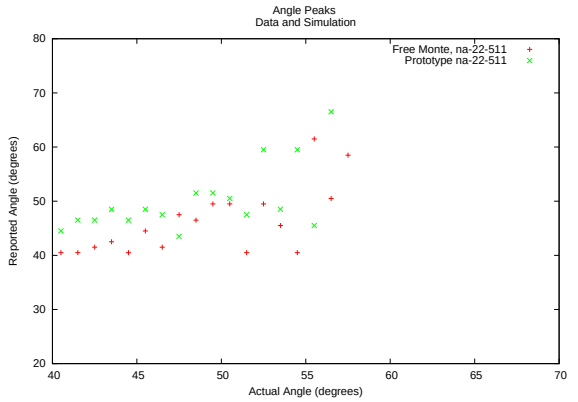

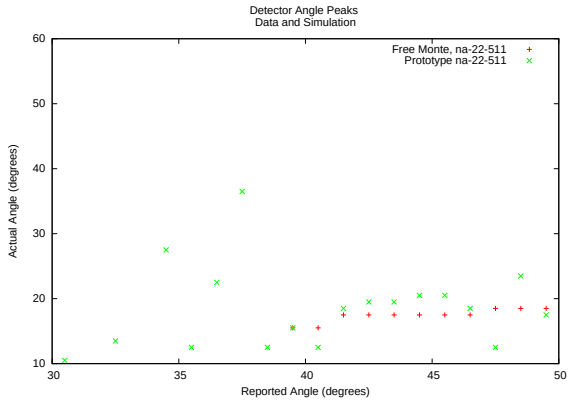

Figure A.24. Na-22, 511 keV 50cm, 0ϕ, $30z$.

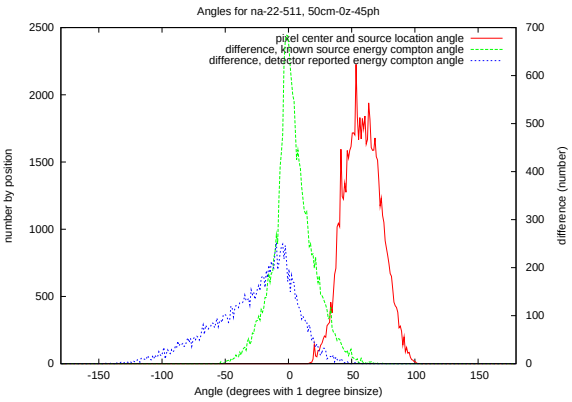

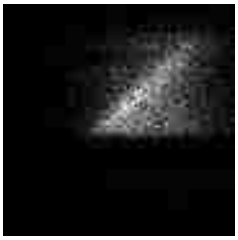

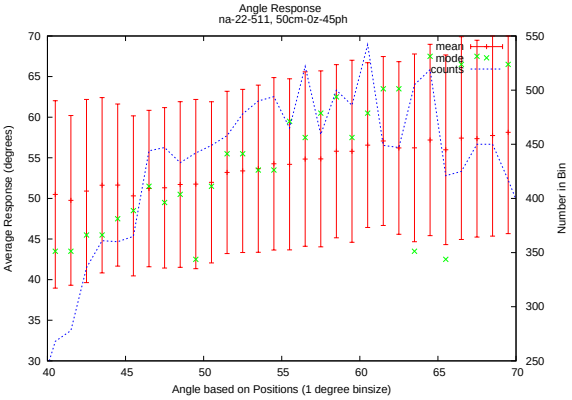

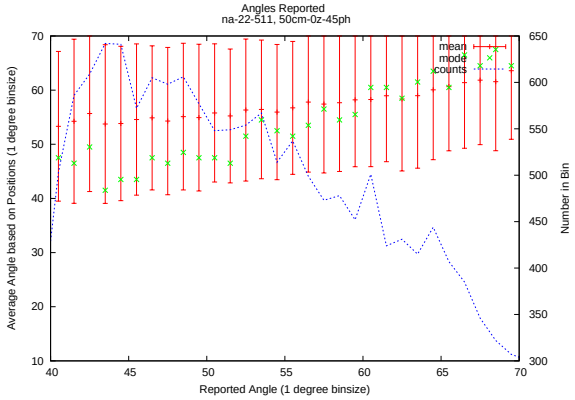

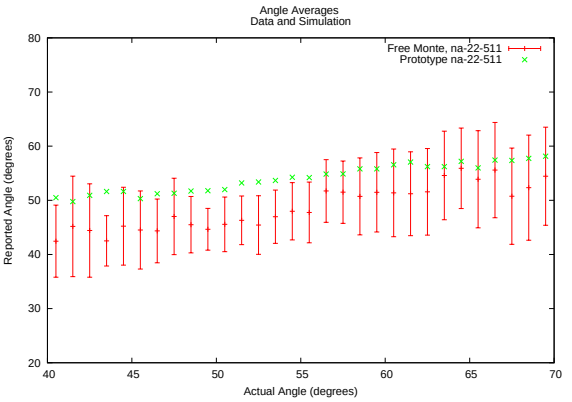

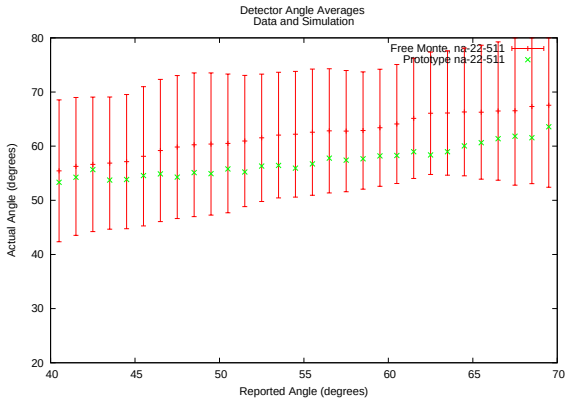

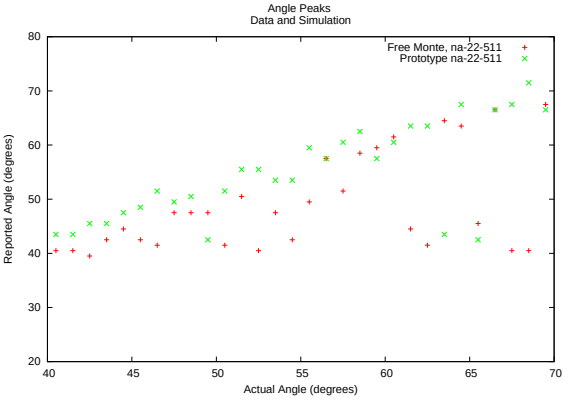

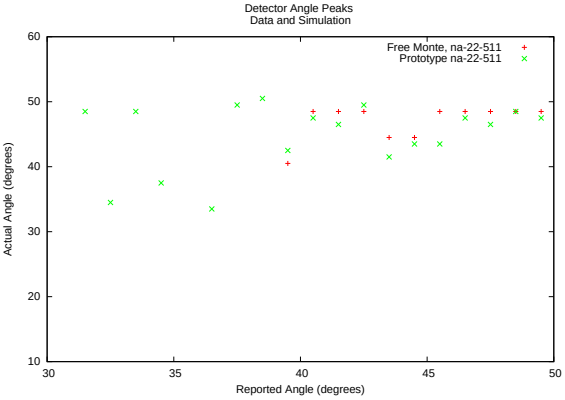

Figure A.25. Na-22, 511 keV 50cm, 45ϕ, 0z.

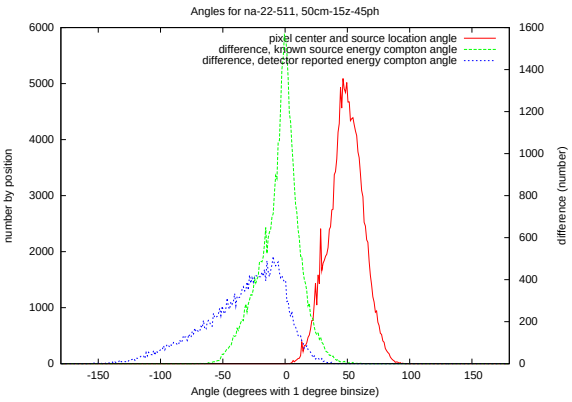

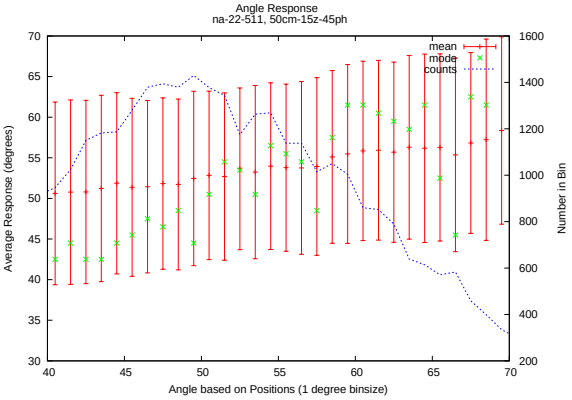

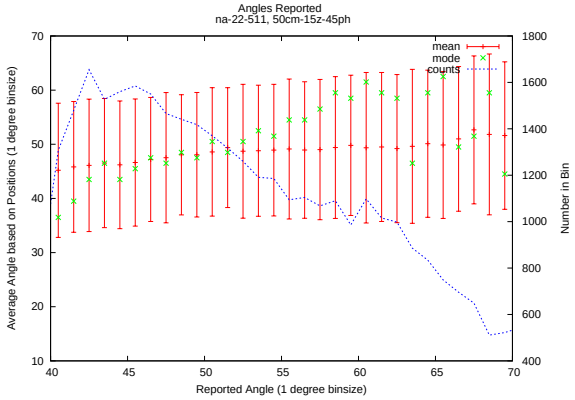

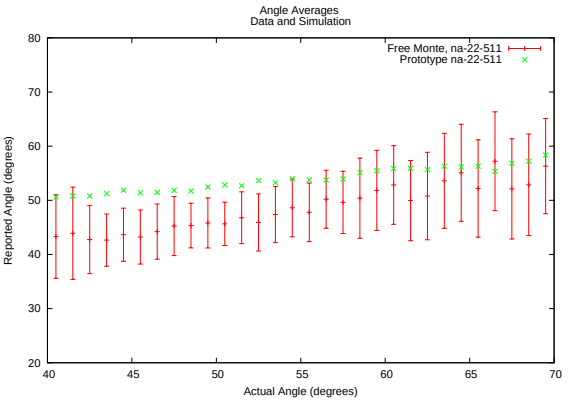

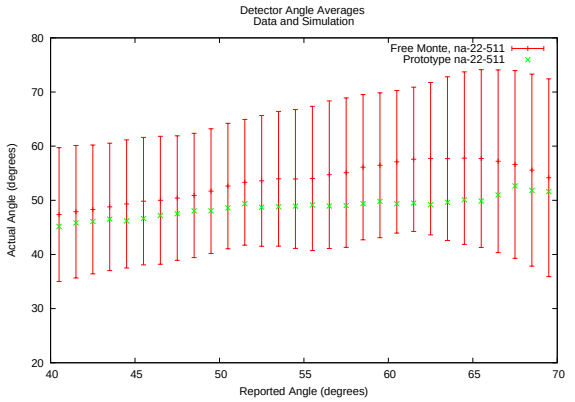

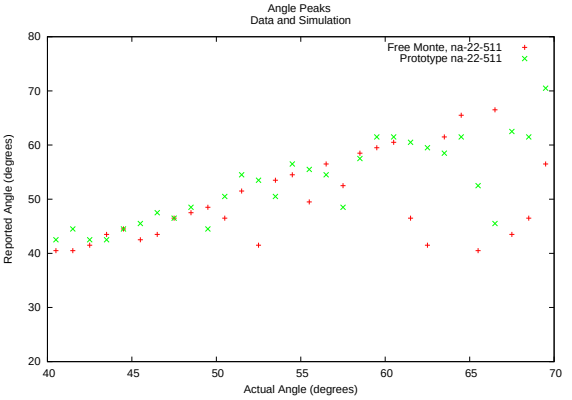

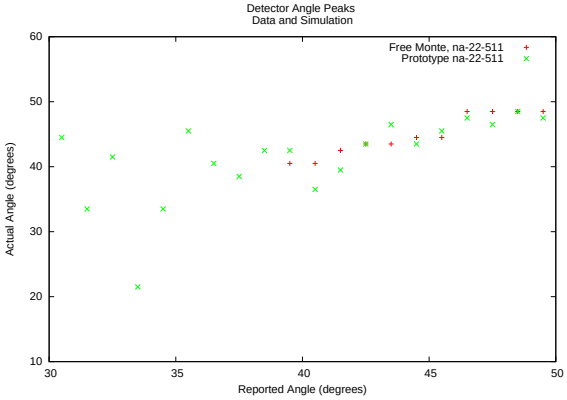

Figure A.26. Na-22, 511 keV 50cm, 45ϕ, 15z.

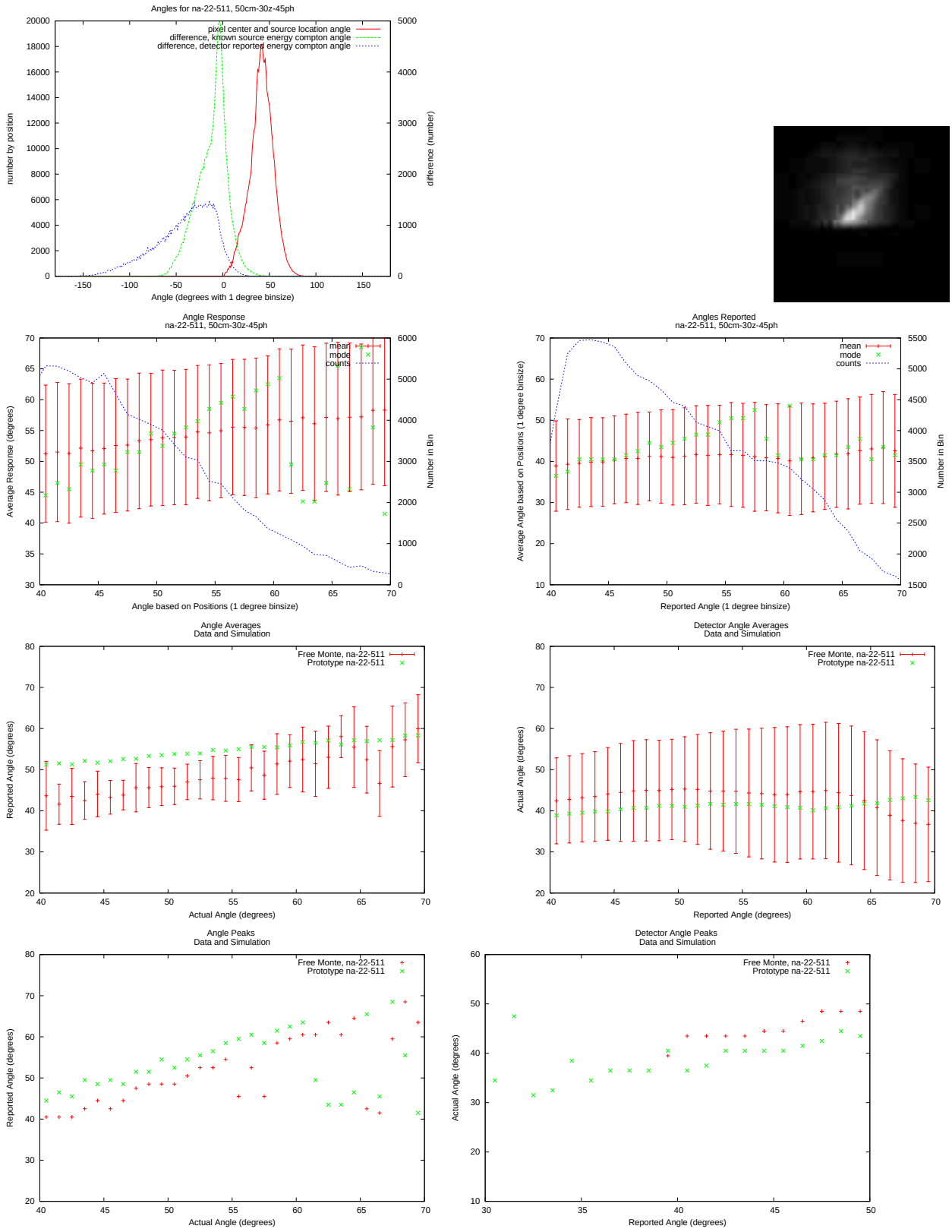

Figure A.27. Na-22, 511 keV 50cm, 45ϕ, 30z.

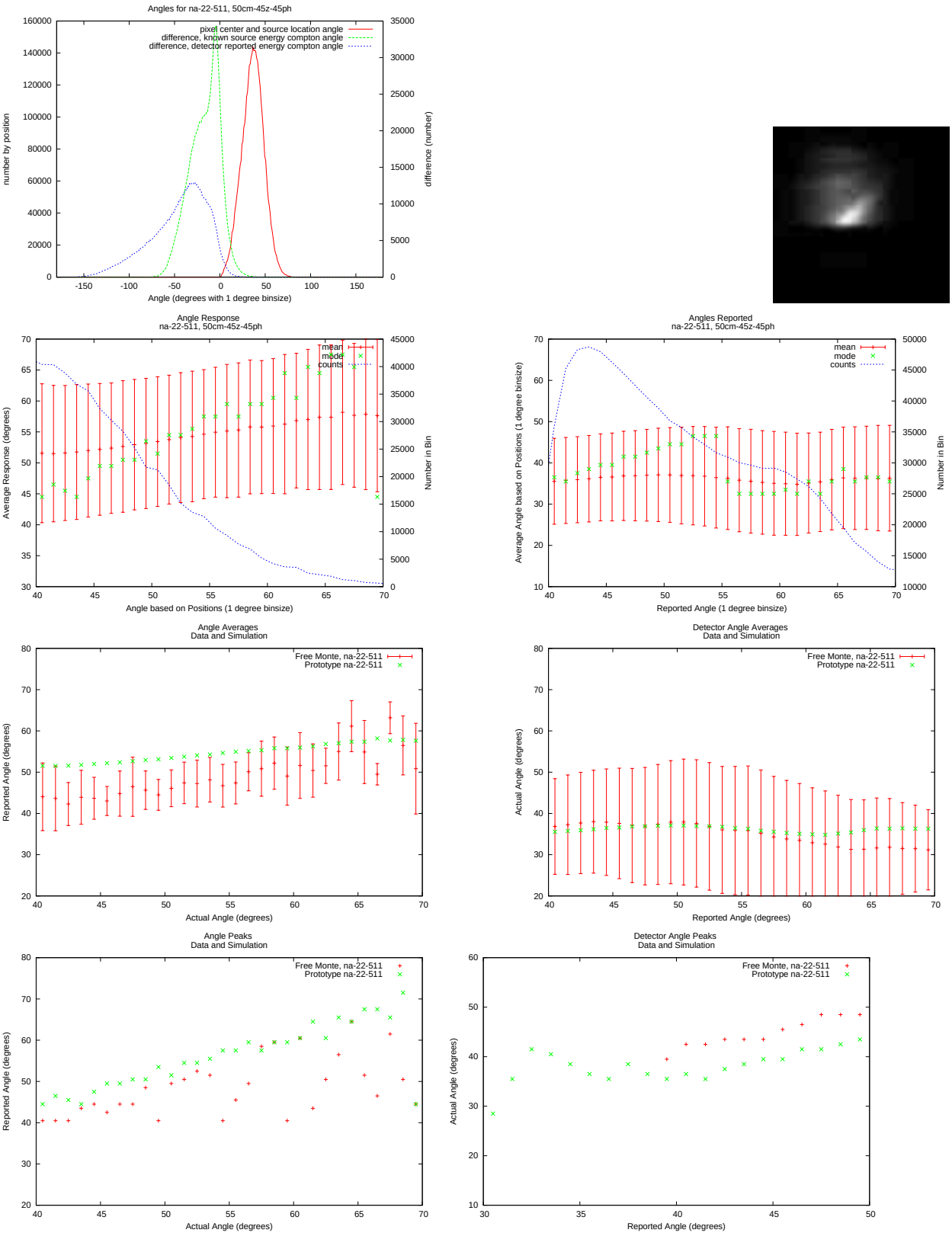

Figure A.28. Na-22, 511 keV 50cm, 45ϕ, 45z.

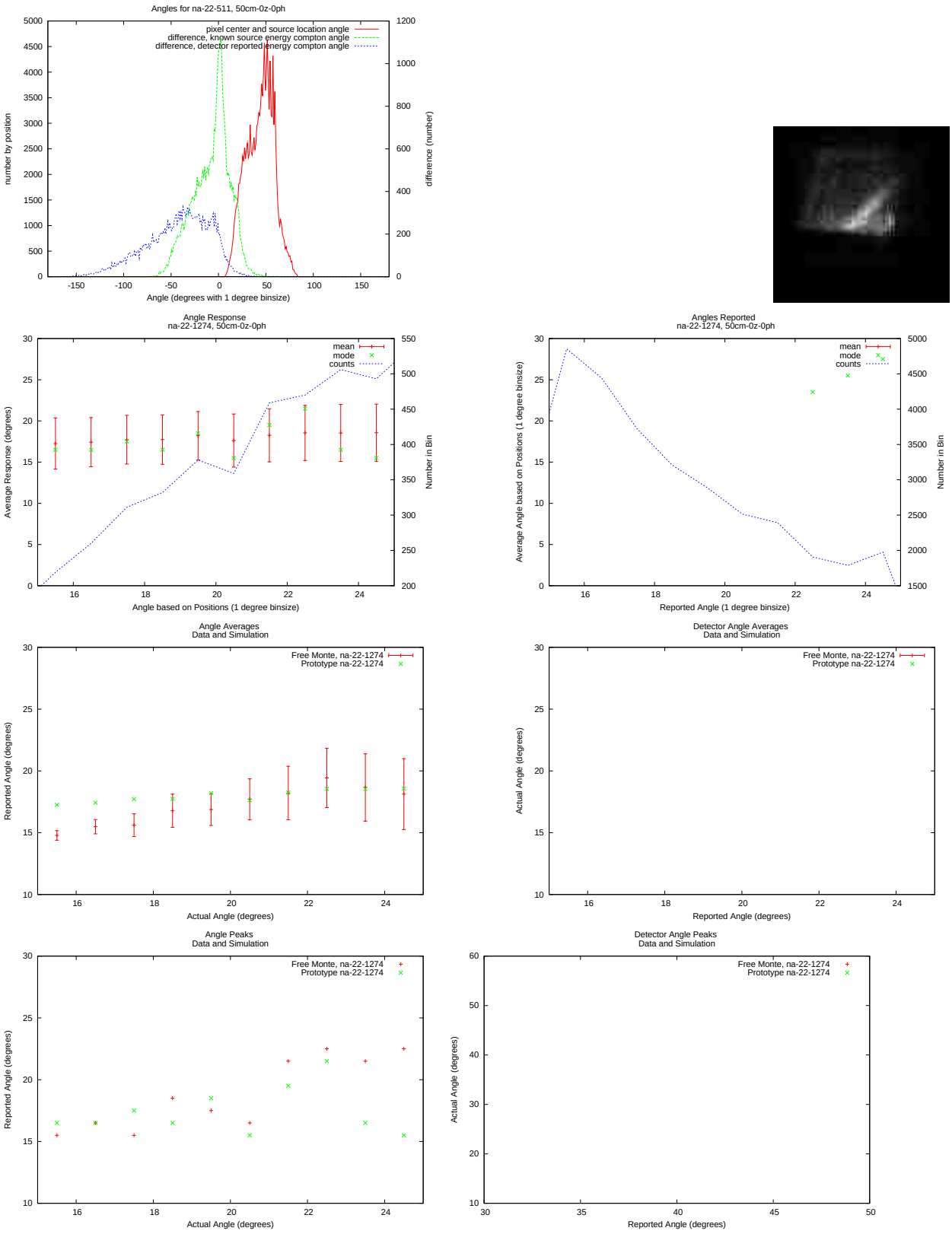

Figure A.29. Na-22, 1274 keV 50cm, 0ϕ, $0z$.

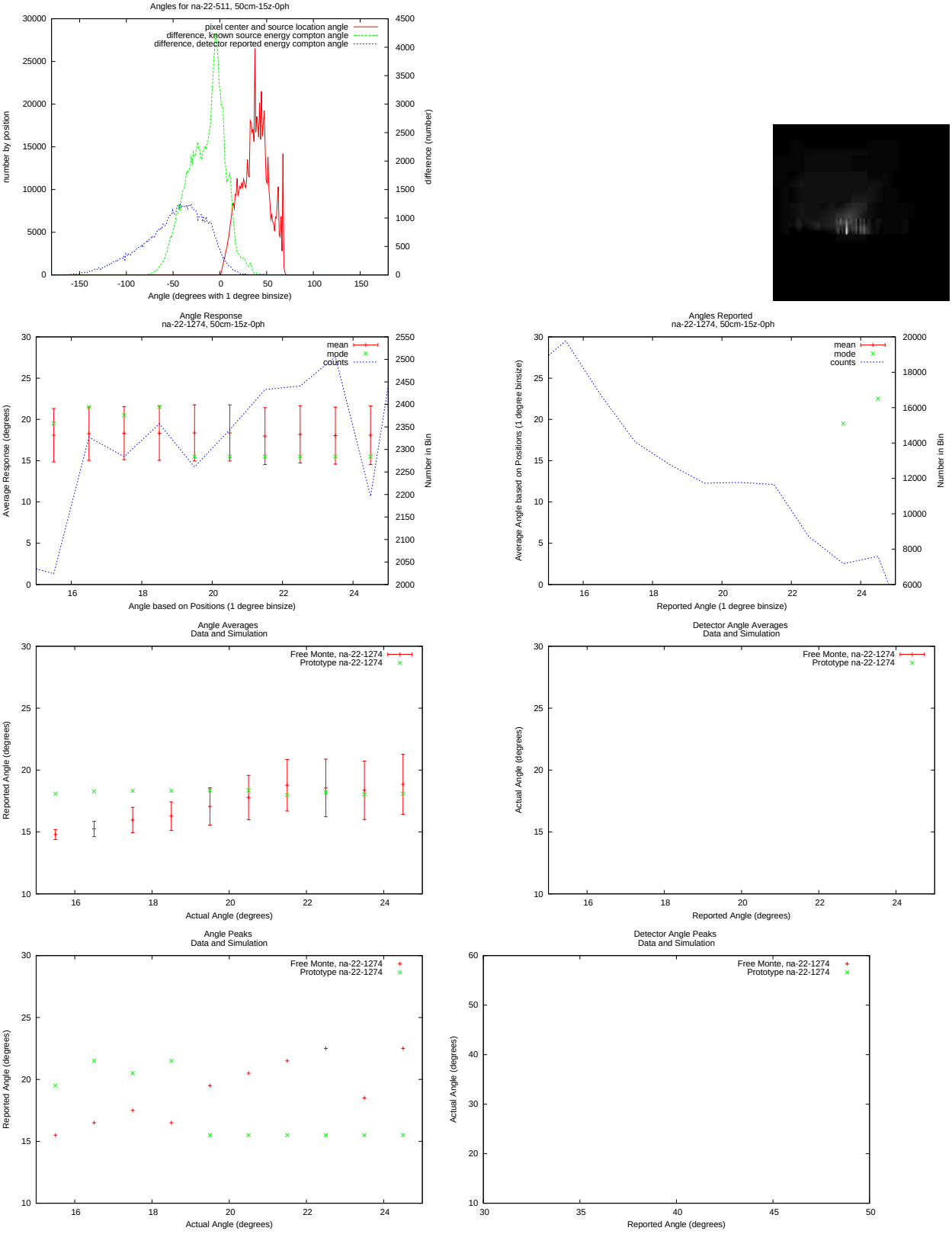

Figure A.30. Na-22, 1274 keV 50cm, 0ϕ, $15z$.

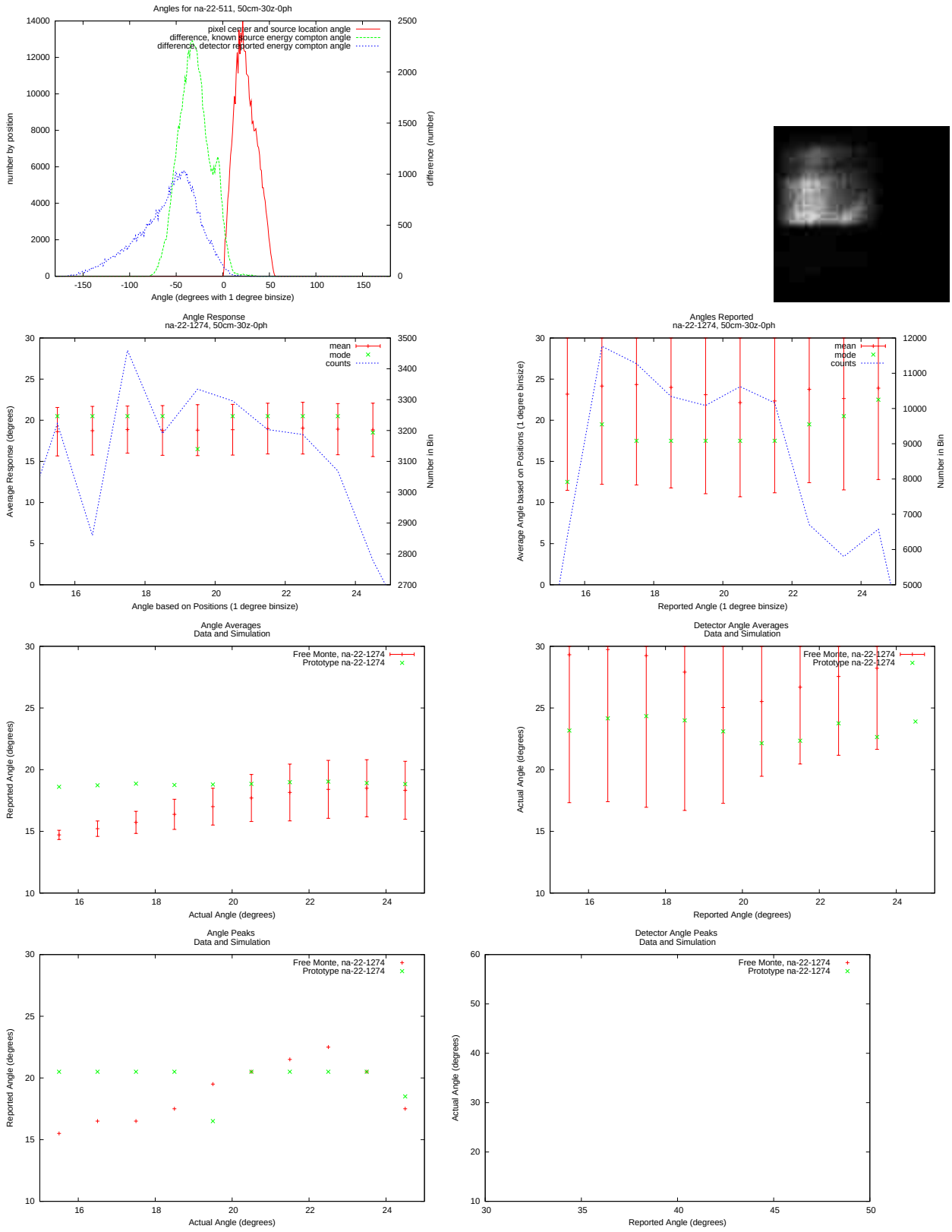

Figure A.31. Na-22, 1274 keV 50cm, 0ϕ, $30z$.

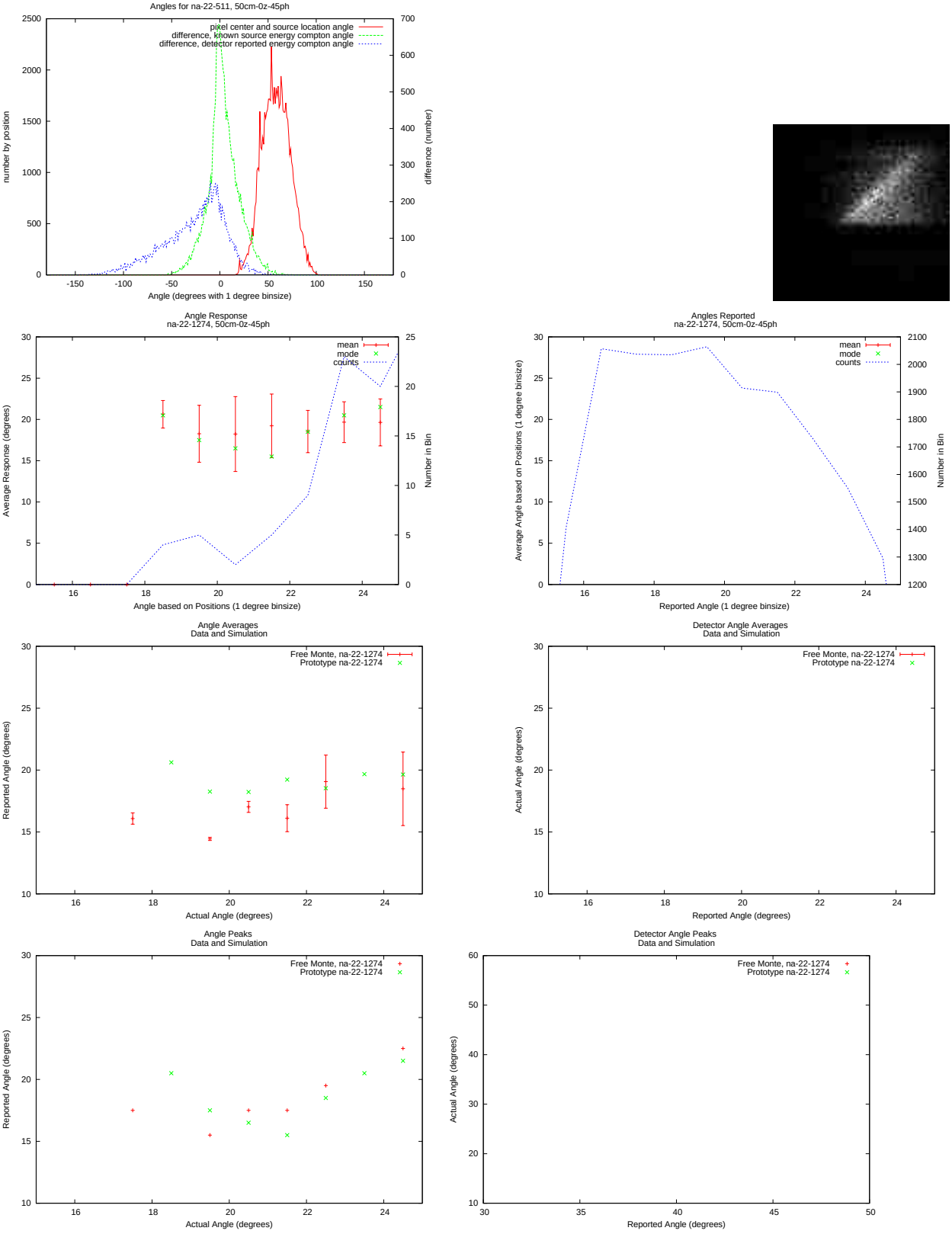

Figure A.32. Na-22, 1274 keV 50cm, 45ϕ, 0z.

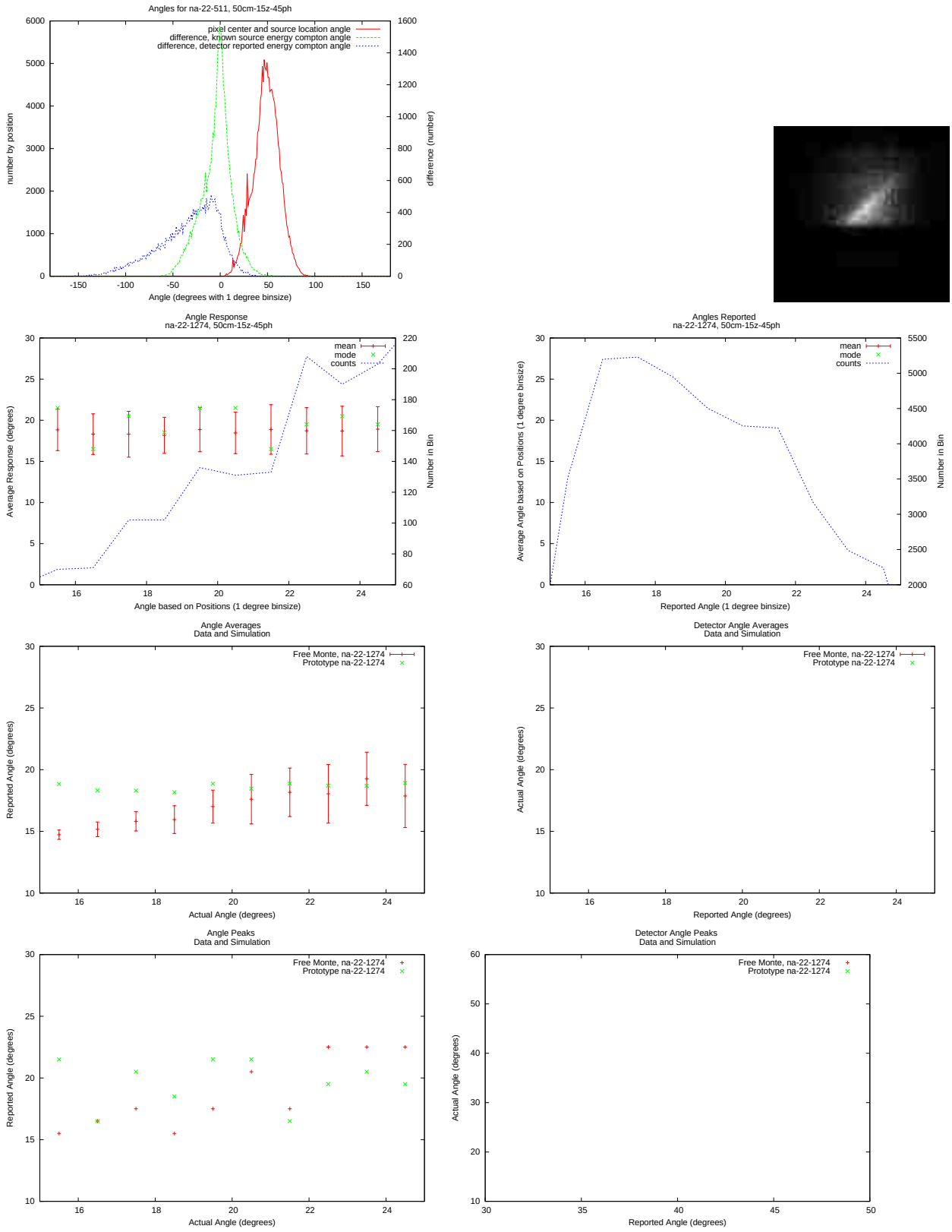

Figure A.33. Na-22, 1274 keV 50cm, 45ϕ, 15z.

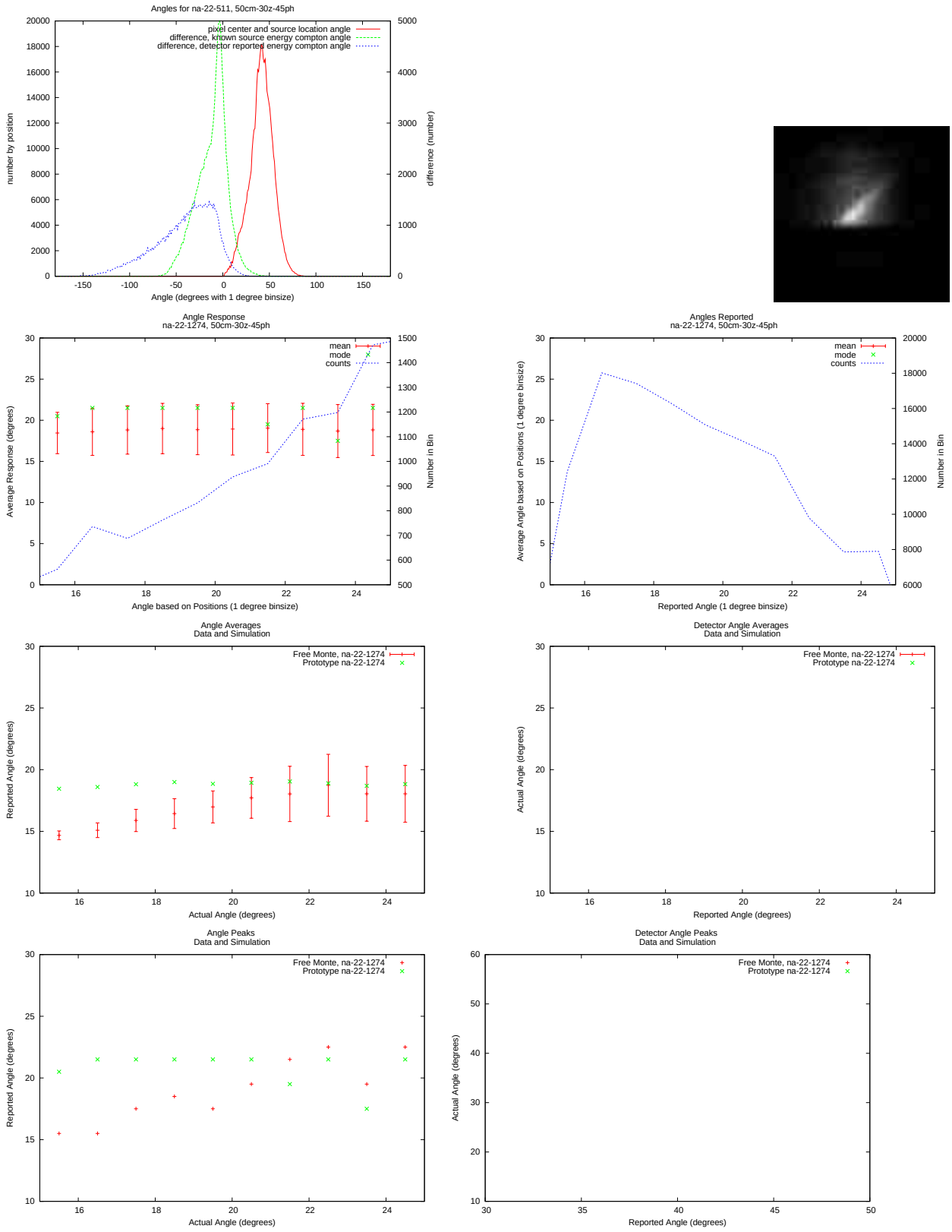

Figure A.34. Na-22, 1274 keV 50cm, 45ϕ, 30z.

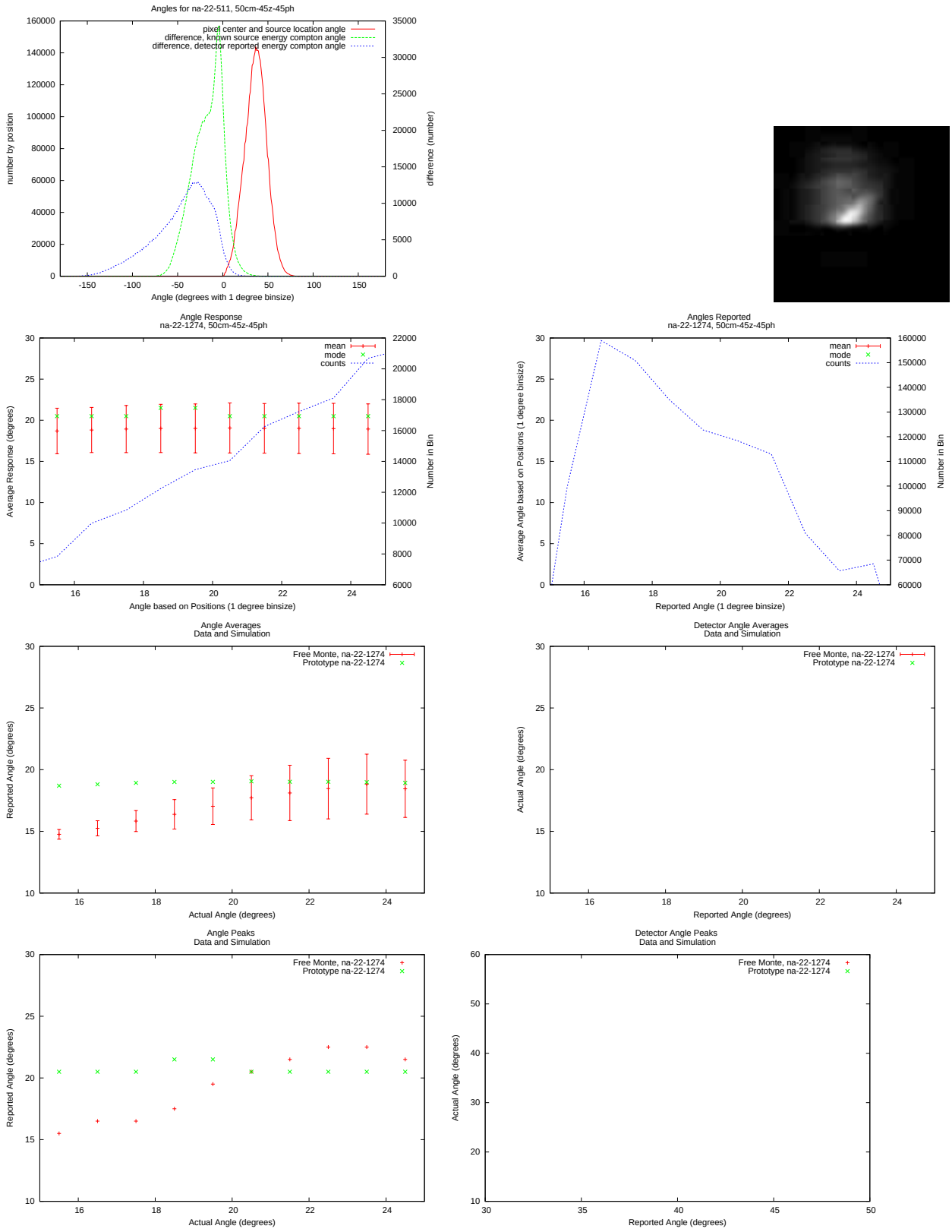

Figure A.35. Na-22, 1274 keV 50cm, 45ϕ, 45z.

APPENDIX B

BACKPROJECTIONS

This appendix contains backprojections of all prototype and simulation results. The first row is data, the second is its simulation and the third row is a full box simulation.

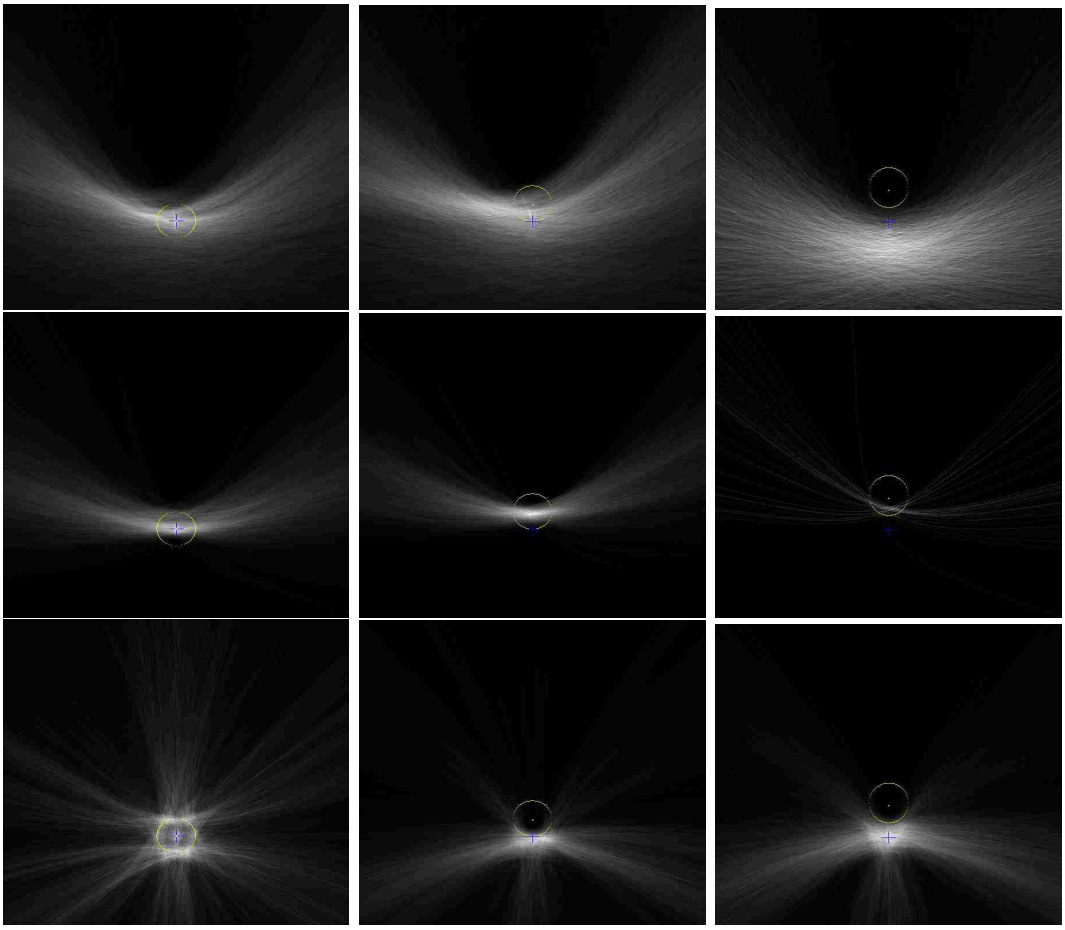

Figure B.1. Backprojection of Ba-133 in plane of symmetry. Source at 50cm, local azimuth 0, local elevation 0, 15 and 30 degrees.

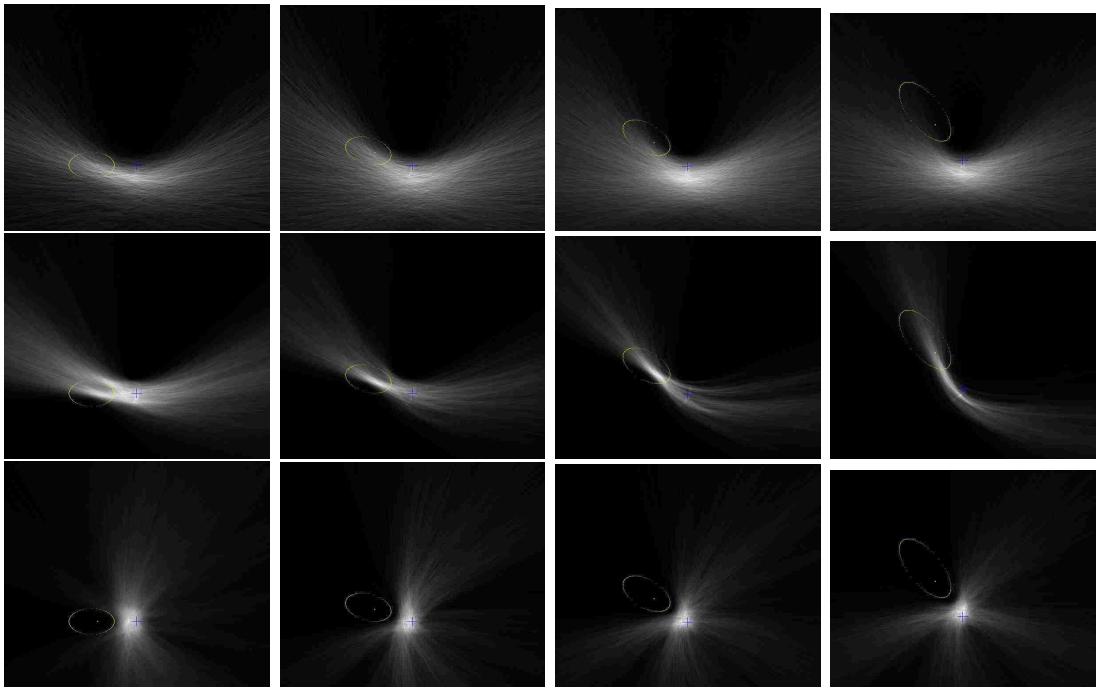

Figure B.2. Backprojection of Ba-133 out of plane of symmetry. Source at 50cm, local azimuth 45, local elevation 0, 15 and 30 degrees.

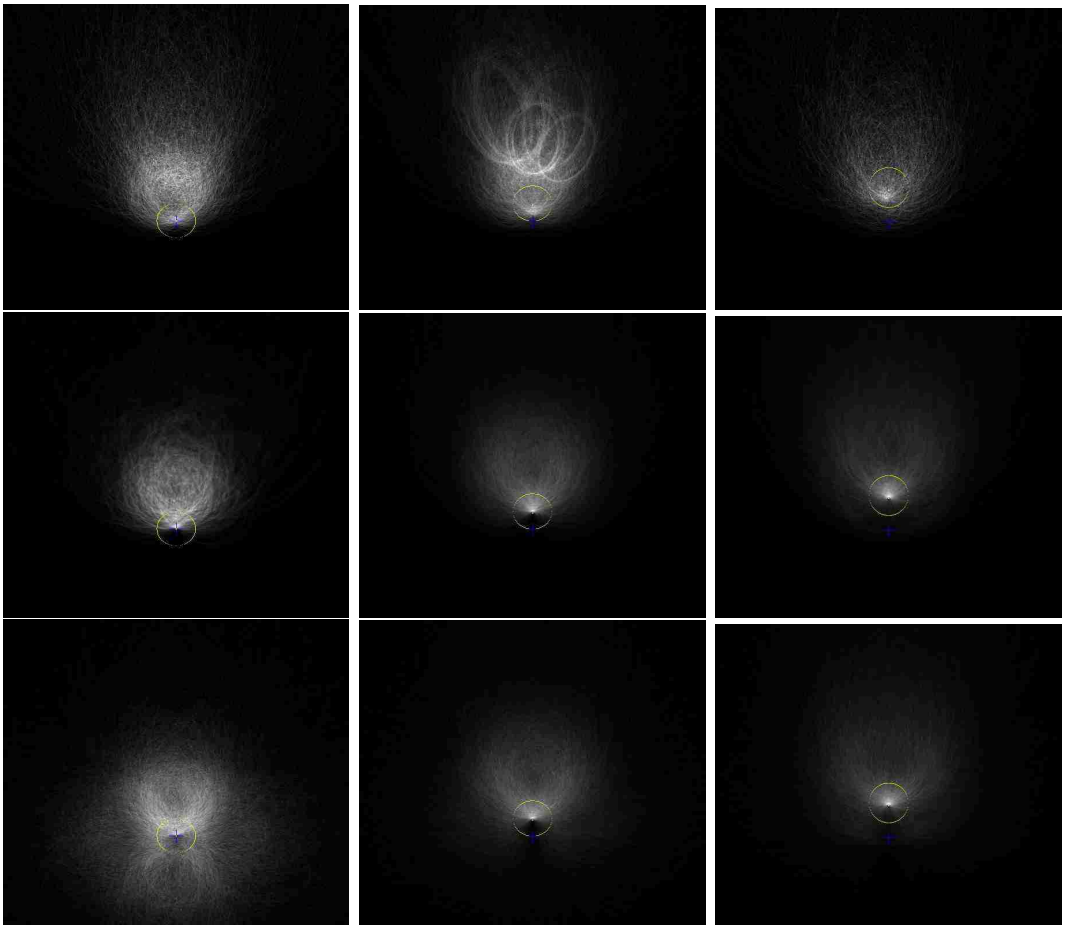

Figure B.3. Backprojection of Co-60 in plane of symmetry. Source at 50cm, local azimuth 0, local elevation 0, 15 and 30 degrees.

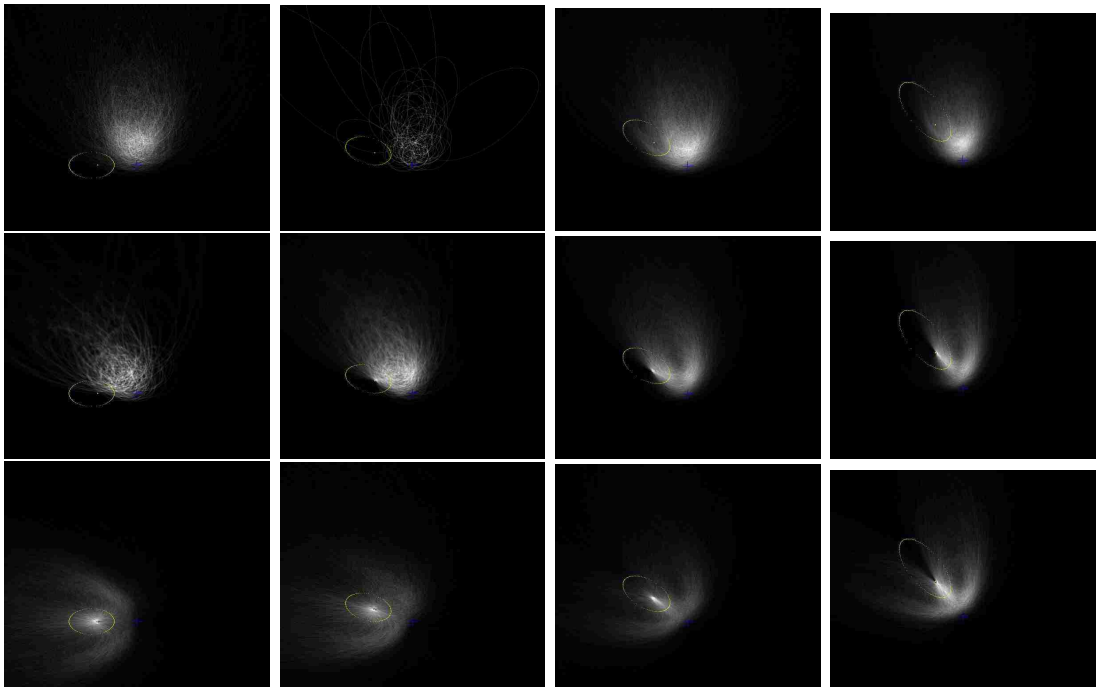

Figure B.4. Backprojection of Co-60 out of plane of symmetry. Source at 50cm, local azimuth 45, local elevation 0, 15 and 30 degrees.

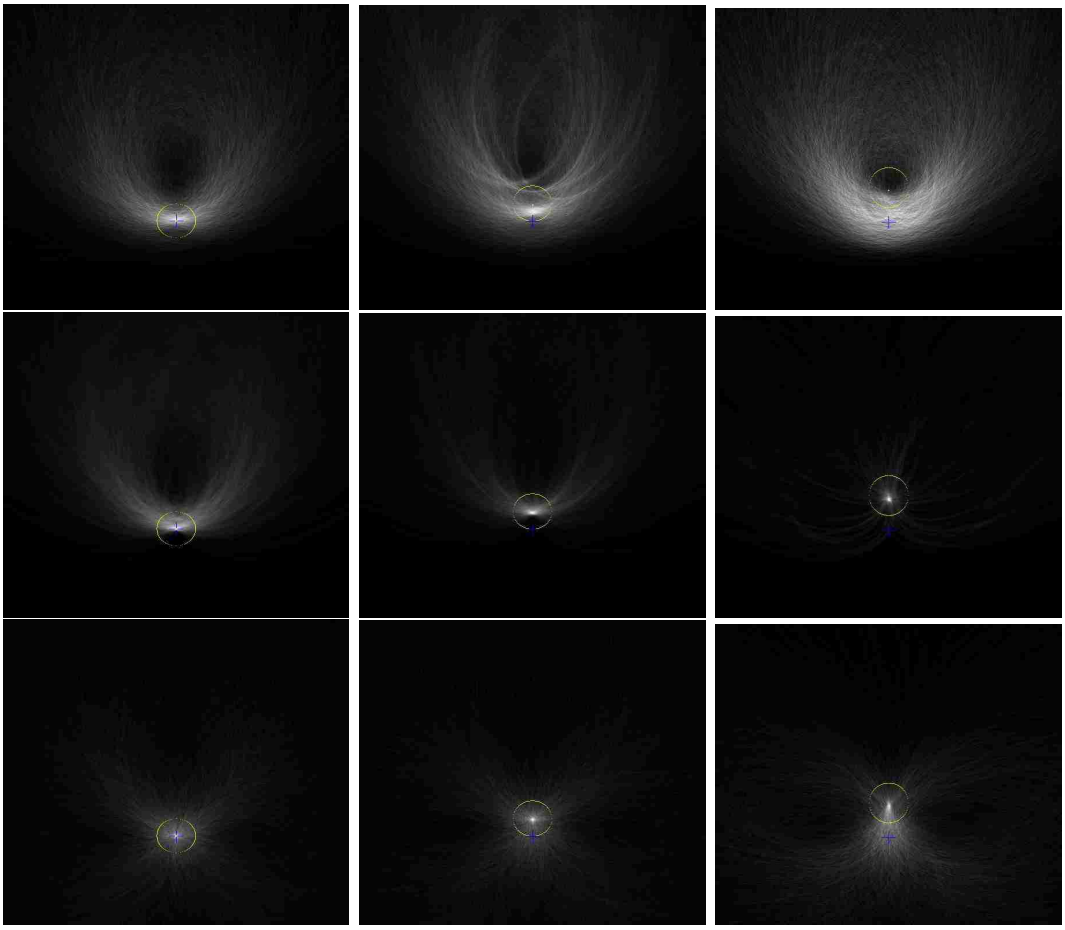

Figure B.5. Backprojection of Cs-137 in plane of symmetry. Source at 50cm, local azimuth 0, local elevation 0, 15 and 30 degrees.

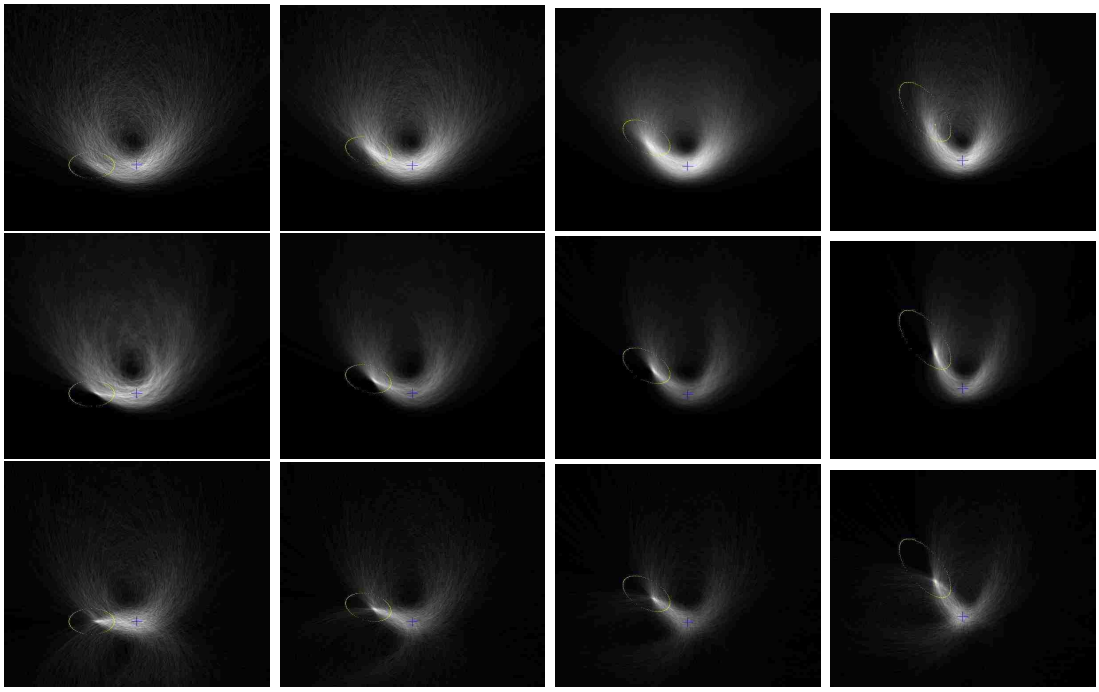

Figure B.6. Backprojection of Cs-137 out of plane of symmetry. Source at 50cm, local azimuth 45, local elevation 0, 15 and 30 degrees.

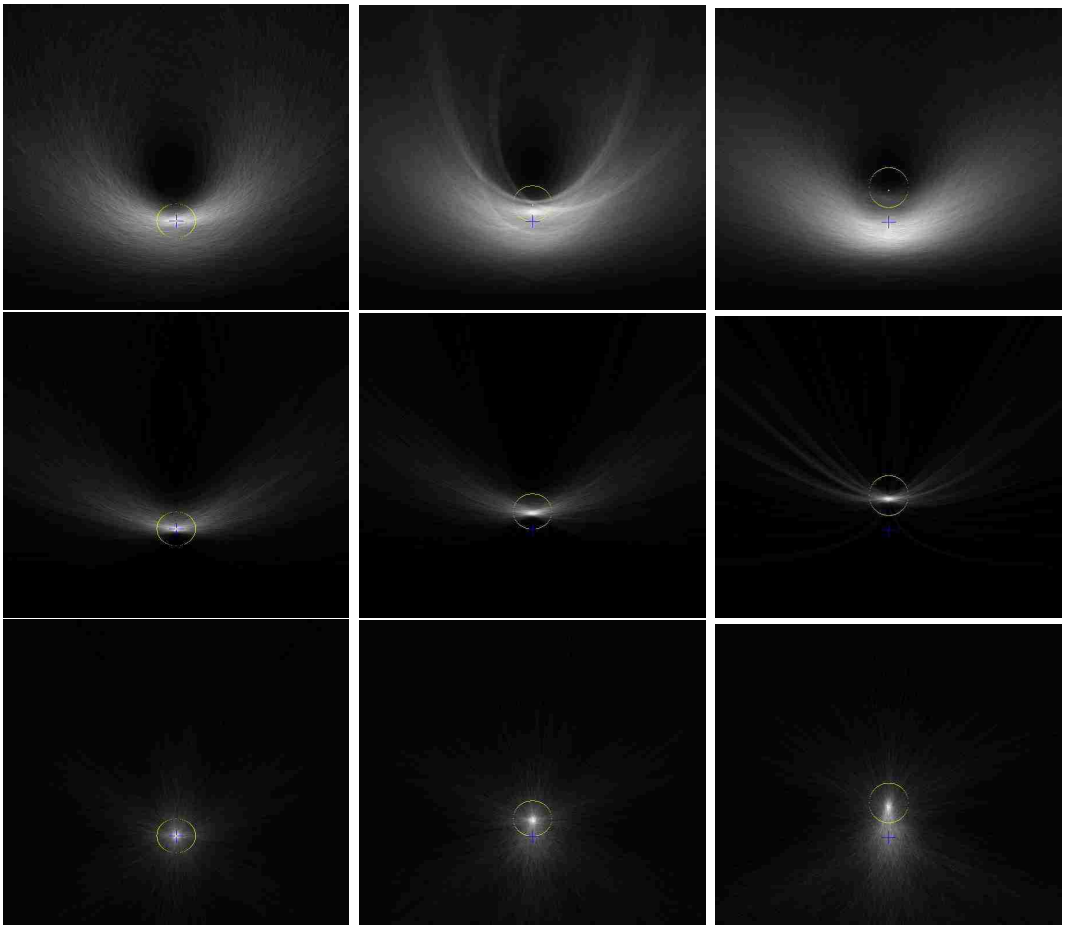

Figure B.7. Backprojection of Na-22 (511 keV) in plane of symmetry. Source at 50cm, local azimuth 0, local elevation 0, 15 and 30 degrees.

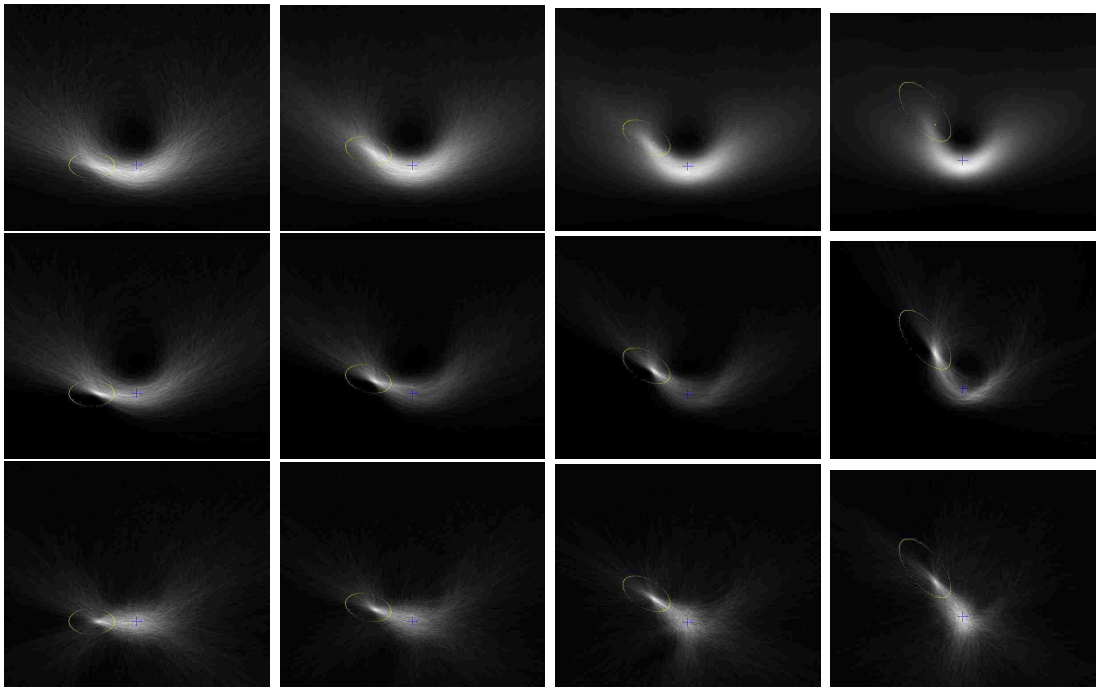

Figure B.8. Backprojection of Na-22 (511 keV) out of plane of symmetry. Source at 50cm, local azimuth 45, local elevation 0, 15 and 30 degrees.

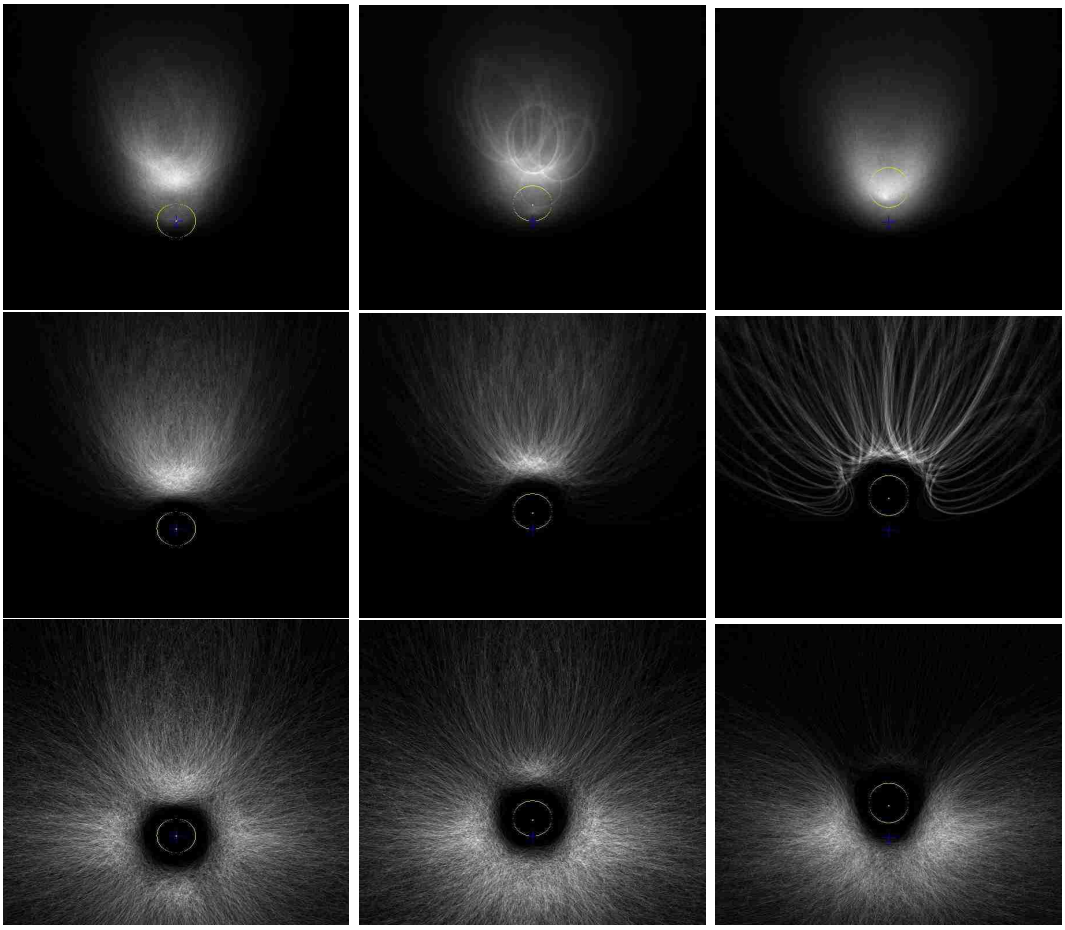

Figure B.9. Backprojection of Na-22 (1274 keV) in plane of symmetry. Source at 50cm, local azimuth 0, local elevation 0, 15 and 30 degrees.

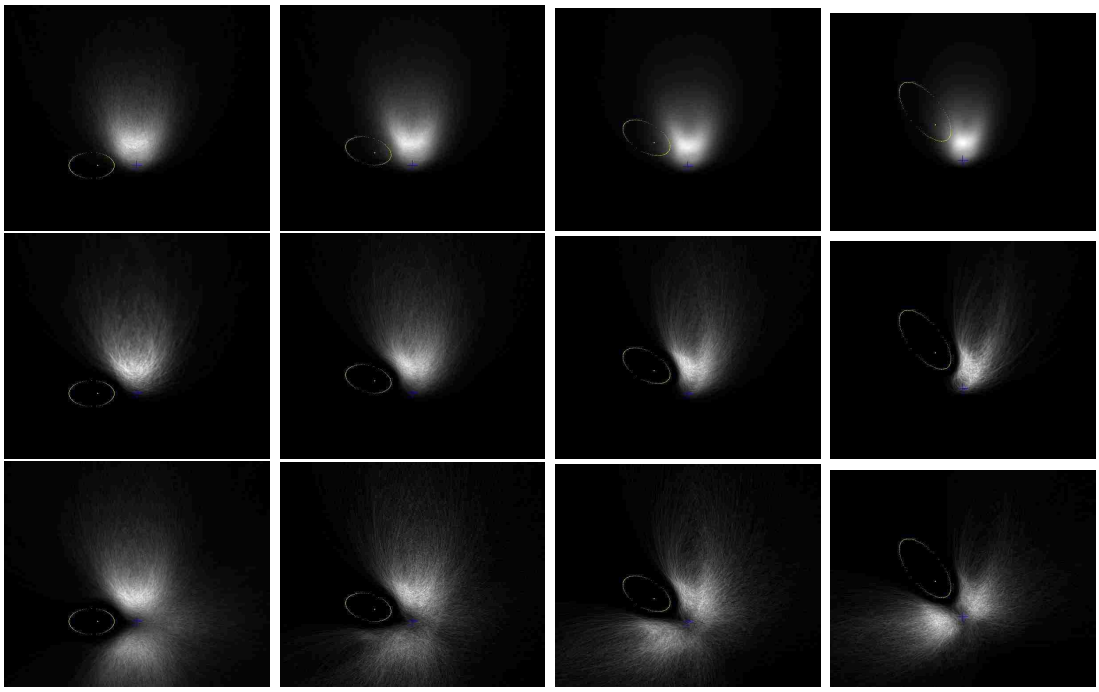

Figure B.10. Backprojection of Na-22 (1274 keV) out of plane of symmetry. Source at 50cm, local azimuth 45, local elevation 0, 15 and 30 degrees.

VITA

Will Hill was born in Nashville, Tennessee, in 1966 and raised in New Orleans, Louisiana. The medical practice of family patriarchs, Drs. Merrill Hines, William Davis and sons blossomed at this time. Their influence complemented the city's already great civic spirit. He earned a Bachelor of Arts in classics from Tulane University in 1989 and a Bachelor of Science in mechanical engineering from Lousiana State University in 1995. After working for an aircraft windshield maker in Florida, Will returned to Louisiana State University and held several research positions while studying Nuclear Science. He then spent two years as a systems engineer at the River Bend Nuclear Generating Station before turning his attention to medical physics.